The Pennsylvania State University

The Graduate School

College of Engineering

OPTICS OF SLANTED CHIRAL SCULPTURED THIN FILMS

A Thesis in

Engineering Science and Mechanics

by

Fei Wang

Submitted in Partial Fulfillment

of the Requirements

for the Degree of

Doctor of Philosophy

May 2005

The thesis of Fei Wang was reviewed and approved* by the following:

Akhlesh Lakhtakia
Distinguished Professor of Engineering Science and Mechanics
Thesis Advisor
Chair of Committee

Russell F. Messier
Professor of Engineering Science and Mechanics

Mark W. Horn
Associate Professor of Engineering Science and Mechanics

Bernhard R. Tittmann
Schell Professor of Engineering Science and Mechanics

Venkatraman Gopalan
Associate Professor of Materials Science and Engineering

Judith A. Todd
P. B. Breneman Department Head Chair
Head of the Department of Engineering Science and Mechanics

*Signatures are on file in the Graduate School.

Abstract

Sculptured thin films (STFs) are unidirectionally nonhomogeneous, anisotropic nanomaterials comprising parallel nanowires of tailored morphology. The nanowire morphology of STFs is exploited to evoke remarkable optical phenomenons of technological interest. To couple the characteristic optical responses of volume gratings and diffraction gratings in the STF architecture, slanted chiral STFs are proposed and optically characterized in this thesis.

The objective of this thesis is to theoretically establish an optical framework for slanted chiral STFs. This objective is achieved by investigating the optical responses of slanted chiral STFs to several types of excitation sources, such as plane waves, optical beams, and dipoles. These studies would also help integrate slanted chiral STFs with semiconductor chips used in the electronics industry.

First, the response of slanted chiral STFs to plane waves is investigated by developing a robust numerical procedure involving the rigorous coupled–wave analysis. The prominent feature of the planewave response is the partial exhibition of the circular Bragg phenomenon in a nonspecular reflection mode and in its diminishment and even elimination by a Rayleigh–Wood anomaly.

Next, the optical response of a slanted chiral STF with a central twist defect is explored, numerically as well as analytically. Due to the twist defect, wave resonance occurs in a localized fashion in the Bragg regime. A remarkable crossover phenomenon is found in slanted chiral STFs for the localization of wave resonance: When the slanted chiral STF is relatively thin, a co–handed reflectance hole occurs in the Bragg regime; as the thickness increases, the co–handed reflectance hole diminishes to vanish eventually, and is replaced by a cross–handed transmittance hole. A coupled–wave theory is employed to derive an approximate but closed–form solution for axial wave propagation in chiral STFs. The crossover phenomenon can be harnessed for the design of ultra–narrowband optical filters.

Finally, the optical responses of slanted chiral STFs to both optical beams and dipolar radiations are examined, which are a step closer to practical applications. An optical beam is represented as an angular spectrum of plane waves, while dipolar radiation is formulated in terms of spectral dyadic Green functions. Lateral shifts of optical beams on reflection by slanted chiral STFs are computed and characterized, with emphasis on the Goos–Hänchen shift. Being comparable with the dimensions of nanomaterials, these lateral shifts are too important to be neglected in nanotechnology. The radiation patterns of Beltrami dipolar sources in the presence of slanted chiral STFs are presented, to elucidate the spatial signature of the circular Bragg phenomenon.

Potential applications of slanted chiral STFs are suggested in this thesis as optical beam-splitters and couplers, nanoband and sub–nanoband spectral–hole filters, and biosensors.

Nontechnical Abstract

Sculptured thin films (STFs) are a class of nanomaterials that emerged during the 1990s from the widely used columnar thin films. The microstructure of an STF is an assembly of virtually identical, curved, and parallel nanowires with diameter 10–100 nm. A wide variety of two–dimensional and three–dimensional nanowire morphologies can nowadays be realized on large–area substrates. Being porous, STFs contain voids of characteristic shapes and sizes. As these voids can be filled with different materials, STFs can function in many different ways and for many different applications in optics and biotechnology. For example, STFs have been designed, fabricated, and tested to filter out selected frequencies of light, change the handedness of light, and optically sense infiltration by moisture. Research on using STFs as biochemical sensors, frequency–tunable lasers, optical pulse–shapers, and transmission–inhibition materials is also occurring.

When the nanowires of a STF are shaped as helixes, the film possesses the property of structural handedness, also known as chirality. Light can also be handed. The attraction of chiral STFs is attributed to the circular Bragg phenomenon displayed by them. Briefly, normally incident light is mostly reflected within a certain wavelength–regime when it has the same handedness as that of the chiral STF; while reflection is little when the handednesses of light and the chiral STF are opposite to each other.

The helical nanowires of a chiral STF stand upright on a substrate. Therefore, the optical periodicity of a chiral STF is unidirectional — along the normal to the substrate plane. It appears possible to fabricate a chiral STF with its helical nanowires slanted at an angle to the normal to the substrate plane. In this way, a slanted chiral STF is formed with optical periodicity both perpendicular and parallel to the substrate plane. The optical importance of slanted chiral STFs lies in the coupling of the dual periodicities — whereas the periodicity perpendicular to the substrate plane gives rise to the circular Bragg phenomenon, the periodicity parallel to the substrate plane leads to the optical

response being spatially multiplexed and discrete.

The objective of this thesis is to theoretically establish an optical framework for slanted chiral STFs. This objective is achieved by investigating the optical responses of slanted chiral STFs to several types of excitation sources, such as plane waves, optical beams, and dipoles. These studies would help integrate slanted chiral STFs with semiconductor chips used in the electronics industry.

First, the response of slanted chiral STFs to plane waves is investigated by developing a robust numerical procedure for reflection and transmission calculations. The prominent feature of the planewave response is exhibited by the circular Bragg phenomenon in a non-specular mode — that is, a normally incident co–handed plane wave is obliquely reflected for the most part, when the circular Bragg phenomenon occurs.

Next, the optical response of a slanted chiral STF with a central twist defect is explored. The central twist defect is introduced into the slanted chiral STF by purposely rotating its upper half by an angle about the helical axis of nanowires in relation to its lower half. Due to the twist defect, wave resonance occurs in a very narrow regime, i.e., it is localized within the wavelength–regime wherein the circular Bragg phenomenon occurs. Additionally, there is a crossover phenomenon associated with the localization of wave resonance by chiral STFs: The localization is seen as a hole in the reflection spectrum when the slanted chiral STF is relatively thin, but as a hole in the transmission spectrum when the thickness is large. This remarkable crossover phenomenon is mathematically elucidated, and can be harnessed for the design of ultra–narrowband optical filters.

Finally, the optical responses of slanted chiral STFs to both optical beams and dipolar radiations are examined, which are a step closer to practical applications. In general, an optical beam is laterally shifted on reflection. Particular interest arises in the so–called Goos–Hänchen shift which is the lateral shift of optical beam when it is totally reflected. Lateral shifts of optical beam on reflection by slanted chiral STFs are computed, with

emphasis on the Goos–Hänchen shift. Being comparable with the dimensions of nanomaterials, these lateral shifts are too important to be neglected in nanotechnology. The radiation pattern of dipolar source in the presence of the slanted chiral STF is presented, which expresses the circular Bragg phenomenon in the coordinate space.

Potential applications of slanted chiral STFs are suggested in this thesis as optical beamsplitters and couplers, spectral–hole filters, and biochemical sensors.

Contents

Glossary of Important Symbols

$a_{\mathrm{L}}^{(n)}$, $a_{\mathrm{R}}^{(n)}$	Complex–valued amplitudes related to LCP and RCP components of order n of incident field
$[\underline{\mathrm{A}}]$, $[\underline{\mathrm{R}}]$, $[\underline{\mathrm{T}}]$	Column vectors defined from $a_{\mathrm{L,R}}^{(n)}$, $r_{\mathrm{L,R}}^{(n)}$ and $t_{\mathrm{L,R}}^{(n)}$
b	Local birefringence
d	Thickness of a chiral STF
d'	$\mathbf{u}_z \cdot \mathbf{r}'$ = location of a point dipolar source
$d_{\mathrm{Br}}^{\parallel}$, $d_{\mathrm{Br}}^{\perp}$	In–plane and out–of–plane lateral shift on Bragg reflection
$d_{\mathrm{L}}^{\mathrm{GH}\parallel}$, $d_{\mathrm{L}}^{\mathrm{GH}\perp}$	In–plane and out–of–plane components of $\mathbf{d}_{\mathrm{L}}^{\mathrm{GH}}$
$d_{\mathrm{L}}^{(n)\parallel}$, $d_{\mathrm{L}}^{(n)\perp}$	In–plane and out–of–plane components of $\mathbf{d}_{\mathrm{L}}^{(n)}$
$d_{\mathrm{R}}^{\mathrm{GH}\parallel}$, $d_{\mathrm{R}}^{\mathrm{GH}\perp}$	In–plane and out–of–plane components of $\mathbf{d}_{\mathrm{R}}^{\mathrm{GH}}$
$d_{\mathrm{R}}^{(n)\parallel}$, $d_{\mathrm{R}}^{(n)\perp}$	In–plane and out–of–plane components of $\mathbf{d}_{\mathrm{R}}^{(n)}$
$\mathbf{d}_{\mathrm{L}}^{\mathrm{GH}}$	Goos–Hänchen shift vector of LCP beam
$\mathbf{d}_{\mathrm{L}}^{(n)}$	Lateral shift vector of order n of LCP beam
$\mathbf{d}_{\mathrm{R}}^{\mathrm{GH}}$	Goos–Hänchen shift vector of RCP beam
$\mathbf{d}_{\mathrm{R}}^{(n)}$	Lateral shift vector of order n of RCP beam
$\mathrm{Diag}[.]_{[m,m']}$	Diagonal matrix
$\mathbf{D}$, $\mathbf{B}$	Electric and magnetic displacement phasors
$\left[\underline{\underline{\tilde{\mathrm{D}}}}\right]$	Diagonal matrix containing eigenvalues of $\left[\underline{\underline{\tilde{\mathbf{P}}}}\right]$
$\left[\underline{\underline{\tilde{\mathrm{D}}}}\right]_{\sigma}$	Diagonal matrix containing eigenvalues of $\left[\underline{\underline{\tilde{\mathbf{P}}}}\right]_{\sigma}$
$\left[\underline{\underline{\tilde{\mathrm{D}}}}_{u}\right]$, $\left[\underline{\underline{\tilde{\mathrm{D}}}}_{l}\right]$	Upper and lower diagonal submatrixes of $\left[\underline{\underline{\tilde{\mathrm{D}}}}\right]$
$\left[\underline{\underline{\tilde{\mathrm{D}}}}_{u}\right]_{\sigma}$, $\left[\underline{\underline{\tilde{\mathrm{D}}}}_{l}\right]_{\sigma}$	Upper and lower diagonal submatrixes of $\left[\underline{\underline{\tilde{\mathrm{D}}}}\right]_{\sigma}$
$\mathbf{e}$	Auxiliary electric field phasor
$\mathbf{e}_i$, $\mathbf{h}_i$	Incident electromagnetic field vectors
$\mathbf{e}_r^{(n)}$, $\mathbf{h}_r^{(n)}$	Reflected electromagnetic field vectors of order n

continued on next page

continued

$\mathbf{e}_t^{(n)}$, $\mathbf{h}_t^{(n)}$	Transmitted electromagnetic field vectors of order n
$\mathbf{E}$, $\mathbf{H}$	Electric and magnetic field phasors
$\mathbf{E}_i$, $\mathbf{H}_i$	Incident electromagnetic field phasors
$\mathbf{E}_r$, $\mathbf{H}_r$	Reflected electromagnetic field phasors
$\mathbf{E}_r^{(n)}$, $\mathbf{H}_r^{(n)}$	Reflected electromagnetic field phasor of order n
$\mathbf{E}_t$, $\mathbf{H}_t$	Transmitted electromagnetic field phasors
$\mathbf{E}_t^{(n)}$, $\mathbf{H}_t^{(n)}$	Transmitted electromagnetic field phasor of order n
$\mathrm{E}_{x,y,z}$	Components of $\mathbf{E}$ for axial wave propagation
$\mathrm{E}_{x,y,z}^{(n)}$, $\mathrm{H}_{x,y,z}^{(n)}$	Floquet harmonic components of $\mathbf{E}$, $\mathbf{H}$
$\tilde{\mathrm{E}}_{x,y,z}^{(n)}$, $\tilde{\mathrm{H}}_{x,y,z}^{(n)}$	Functions defined from $\mathrm{E}_{x,y,z}^{(n)}$, $\mathrm{H}_{x,y,z}^{(n)}$
$[\underline{\mathrm{E}}_\sigma(z)]$, $[\underline{\mathrm{E}}_\sigma(z)]$	Column vectors defined from $\mathrm{E}_{x,y,z}^{(n)}$, $\mathrm{H}_{x,y,z}^{(n)}$
$[\underline{\mathrm{E}}_\perp(z)]$	2–column vector containing E_x and E_y
$\left[\underline{\tilde{\mathrm{E}}}_\sigma(z)\right]$, $\left[\underline{\tilde{\mathrm{E}}}_\sigma(z)\right]$	Column vectors containing $\tilde{\mathrm{E}}_{x,y,z}^{(n)}$, $\tilde{\mathrm{H}}_{x,y,z}^{(n)}$
$\left[\underline{\tilde{\mathrm{E}}}_\perp(z)\right]$	2–column vector related to $[\underline{\mathrm{E}}_\perp(z)]$
$[\underline{\mathbf{f}}\,(z)]$	Column vector containing $[\underline{\mathrm{E}}_\sigma(z)]$ and $[\underline{\mathrm{H}}_\sigma(z)]$
$\left[\underline{\tilde{\mathbf{f}}}(z)\right]$	Column vector containing $\left[\underline{\tilde{\mathrm{E}}}_\sigma(z)\right]$ and $\left[\underline{\tilde{\mathrm{H}}}_\sigma(z)\right]$
$\left[\underline{\underline{\mathrm{G}}}(z)\right]$	Square matrix function related to $\left[\underline{\underline{\tilde{\mathrm{G}}}}\right]$
$\left[\underline{\underline{\mathrm{G}}}(z)\right]_\sigma$	Square matrix function related to $\left[\underline{\underline{\tilde{\mathrm{G}}}}\right]_\sigma$
$\left[\underline{\underline{\tilde{\mathrm{G}}}}\right]$	Square matrix containing eigenvectors of $\left[\underline{\underline{\tilde{\mathbf{P}}}}\right]$
$\left[\underline{\underline{\tilde{\mathrm{G}}}}\right]_\sigma$	Square matrix containing eigenvectors of $\left[\underline{\underline{\tilde{\mathbf{P}}}}\right]_\sigma$
$\underline{\underline{\mathbf{G}}}_0$	Free–space dyadic Green function (DGF)
$\underline{\underline{\mathbf{G}}}_{\mathrm{L}0}$, $\underline{\underline{\mathbf{G}}}_{\mathrm{R}0}$	DGFs defined from $\underline{\underline{\mathbf{G}}}_0(\mathbf{r},\mathbf{r}')$
$\underline{\underline{\mathbf{G}}}_{\mathrm{L}}$, $\underline{\underline{\mathbf{G}}}_{\mathrm{R}}$	DGFs in the presence of a slanted chiral STF
$\underline{\underline{\mathbf{G}}}_{\mathrm{L}r}$, $\underline{\underline{\mathbf{G}}}_{\mathrm{R}r}$	Reflection DGFs
$\underline{\underline{\mathbf{G}}}_{\mathrm{L}t}$, $\underline{\underline{\mathbf{G}}}_{\mathrm{R}t}$	Transmission DGFs

continued on next page

continued

$h = \pm 1$	Structural handedness parameter
$\mathrm{H}_{x,y,z}$	Components of $\mathbf{H}$ for axial wave propagation
$[\underline{\mathrm{H}}'_{\perp}(z)]$	2–column vector containing $\eta_0 \mathrm{H}_x$ and $\eta_0 \mathrm{H}_y$
i	$\sqrt{-1}$
$\left[\underline{\underline{\mathrm{I}}}\right]_m$	$m \times m$ identity matrix
$\underline{\underline{\mathrm{I}}}$	3×3 identity dyadic
$\mathbf{J}(\mathbf{r}')$, $\mathbf{K}(\mathbf{r}')$	Source electric and magnetic density phasors
k	$k_0 \bar{n}$
k_0	Free–space wavenumber
k_δ	$k_0 \delta_n$
$k_x^{(n)}$, $k_y^{(0)}$, $k_z^{(n)}$	Coordinate components of $\mathbf{k}_{\pm}^{(n)}$
$\mathbf{k}_{+}^{(0)}$	Wavevector of incident plane wave
$\mathbf{k}_{\pm}^{(n)}$	Wavevector of the nth–order Floquet harmonic
$\left[\underline{\underline{\mathrm{K}}}_x\right]$	Diagonal matrix containing $\mathbf{k}_x^{(n)}$
$\mathbf{L}_{\pm}^{(n)}$, $\mathbf{R}_{\pm}^{(n)}$	Circular polarization vectors of order n
n	Floquet harmonic order
$\bar{n}$	$\sqrt{\bar{\epsilon}}$
n_{hs}	Refractive index of ambient dielectric medium
$\mathrm{N}_{a,b,c}$	Absorption linewidths
N_d	d/Ω
N_d^{co}	Crossover value of N_d
N_t	Maximum harmonic order for computation; $\lvert n \rvert \leq \mathrm{N}_t$
$p_{a,b,c}$	Oscillator strengths
$\left[\underline{\underline{\tilde{\mathbf{P}}}}\right]$	Kernel matrix
$\left[\underline{\underline{\tilde{\mathbf{P}}}}\right]_\sigma$	Different values of kernel matrix

continued on next page

continued

$r_{\mathrm{L}}^{(n)}$, $r_{\mathrm{R}}^{(n)}$	Complex–valued amplitudes related to LCP and RCP components of order n of reflected field
r_{LL}, etc.	Reflection coefficients for axial wave propagation
$r_{\mathrm{LL}}^{(n)}$, etc.	Reflection coefficients of order n
$\mathbf{r}$, $\mathbf{r}'$	Position vectors
$\tilde{\mathbf{r}}$,	$\mathbf{r} - d\mathbf{u}_z$
$\mathbf{R}$	$\mathbf{r} - \mathbf{r}'$
$\mathbf{R}$ R_{LL}, etc.	Reflectances for axial wave propagation
$\mathrm{R}_{\mathrm{LL}}^{(n)}$, etc.	Reflectances of order n
$\mathbf{s}^{(n)}$, $\mathbf{p}_{\pm}^{(n)}$	Linear polarization vectors of order n
$\underline{\underline{s}}_y$, $\underline{\underline{s}}_z$	Rotation dyadics for slanted chiral STFs
$\underline{\underline{\mathrm{S}}} \in \left\{ \underline{\underline{\mathrm{S}}}_x, \underline{\underline{\mathrm{S}}}_y, \underline{\underline{\mathrm{S}}}_z \right\}$	Rotation dyadic
t	Time
$t_{\mathrm{L}}^{(n)}$, $t_{\mathrm{R}}^{(n)}$	Complex–valued amplitudes related to LCP and RCP components of order n of transmitted field
t_{LL}, etc.	Transmission coefficients for axial wave propagation
$t_{\mathrm{LL}}^{(n)}$, etc.	Transmission coefficients of order n
T_{LL}, etc.	Transmittances for axial wave propagation
$\mathrm{T}_{\mathrm{LL}}^{(n)}$, etc.	Transmittances of order n
$\mathbf{u}_s$	Orientation vector of a dipole
$\mathbf{u}_x, \mathbf{u}_y, \mathbf{u}_z$	Unit Cartesian vectors
$\mathbf{u}_{\bar{x}}, \mathbf{u}_{\bar{y}}, \mathbf{u}_{\bar{z}}$	Unit Cartesian vectors for beam incidence
$\mathbf{u}_\tau, \mathbf{u}_n, \mathbf{u}_b$	Unit Cartesian vectors to describe nanowire morphology
$\mathbf{u}_\ell$	Unit vector parallel to the axis of nonhomogeneity
$\mathbf{W}_{\mathrm{L}}$, $\mathbf{W}_{\mathrm{R}}$	Beltrami source configurations

continued on next page

continued

$\left[\underline{\underline{\mathrm{W}}}^{\pm}(z)\right]$	4×4 transfer matrix for axial wave propagation
(x, y, z)	Cartesian coordinate system
$(\bar{x}, \bar{y}, \bar{z})$	Cartesian coordinate system for optical beam
$\left[\underline{\underline{\mathrm{Y}}}_{e}^{\pm}\right]$, $\left[\underline{\underline{\mathrm{Y}}}_{h}^{\pm}\right]$	Square matrixes derived from $\mathbf{L}_{\pm}^{(n)}$, $\mathbf{R}_{\pm}^{(n)}$, $\mathbf{s}^{(n)}$ and $\mathbf{p}_{\pm}^{(n)}$
α	Slant angle of a (slanted) chiral STF
α_n, $\tilde{\alpha}_n$	Saddle points along the SDPs of $k_x^{(0)}$
α_∞	Matrix weight
$\underline{\underline{\alpha}}$, $\underline{\underline{\beta}}$	Relative magnetoelectricity dyadics
$\underline{\underline{\alpha}}_{ref}$, $\underline{\underline{\beta}}_{ref}$	Reference relative magnetoelectricity dyadics
β	$(k - \pi/\Omega)/k_\delta$
β_0, $\tilde{\beta}_0$	Saddle points along the SDPs of $k_y^{(0)}$
γ_n	$+\sqrt{k_0^2 - \alpha_n^2 - \beta_0^2}$
$\tilde{\gamma}_n$	$+\sqrt{k_0^2 - \tilde{\alpha}_n^2 - \tilde{\beta}_0^2}$
$\delta(.)$	Dirac delta function
δ_n	$\delta_\epsilon / 2\bar{n}$
$\delta_{n,n'}$	Kronecker delta
δ_ϵ	$(\epsilon_d - \epsilon_c)/2$
ϵ_0	Free–space permittivity
$\epsilon_{a,b,c}$	Reference relative permittivity scalars
ϵ_d	Parameter derived from ϵ_a, ϵ_b and χ_s
$\bar{\epsilon}$	$(\epsilon_d + \epsilon_c)/2$
$\epsilon_{\sigma\sigma'}^{(n)}$	Components of $\underline{\underline{\epsilon}}^{(n)}$
$\underline{\underline{\epsilon}}$	Relative permittivity dyadic
$\underline{\underline{\epsilon}}_{ref}$	Reference relative permittivity dyadic
$\underline{\underline{\epsilon}}^{(n)}$	Constant–valued dyadic derived from $\underline{\underline{\epsilon}}$

continued on next page

continued

$\left[\underline{\underline{\epsilon}}_{perp}(z)\right]$	2×2 matrix defined from $\underline{\underline{\epsilon}}$ for axial wave propagation
$\left[\underline{\underline{\epsilon}}_{\sigma\sigma'}\right]$	Toeplitz matrix defined from $\underline{\underline{\epsilon}}^{(n)}$
ζ_x, ζ_y, ζ_z	Rotational angles to describe morphology
ζ_ρ	Polar angle of observation
η_0	Intrinsic impedance of free space
θ_i^b, ψ_i^b	Mean polar and azimuthal angles of beam incidence
θ_i^p, ψ_i^p	Polar and azimuthal angles of planewave incidence
θ_{ic}^b	Critical value of θ_i^b upon total reflection
θ_{ic}^p	Critical value of θ_i^p upon total reflection
$\vartheta_x, \vartheta_y, \vartheta_z$	Variables related to wavevector
κ_x, κ_z	$\kappa_x = \frac{2\pi}{\Lambda_x}$, $\kappa_z = \frac{2\pi}{\Lambda_z}$
$\left[\underline{\underline{\kappa}}_z\right]$	Diagonal matrix defined from κ_z
λ_0	Free–space wavelength
λ_0^{Br}	Center–wavelength of Bragg regime
$\lambda_{0_{\mathrm{CWT}}}^{\mathrm{Br}}$	Center–wavelength of Bragg regime predicted by CWT
λ_0^p	Peak wavelength
$\lambda_{0_{\mathrm{CWT}}}^p$	Peak wavelength predicted by CWT
$\lambda_{0_n}^{\mathrm{RW}}$	Free–space wavelength of Rayleigh–Wood anomaly of order n
$\lambda_{a,b,c}$	Resonance wavelengths
λ_{hs}	Wavelength in the medium with refractive index n_{hs}
μ_0	Free–space permeability
$\underline{\underline{\mu}}$	Relative permeability dyadic
$\underline{\underline{\mu}}_{ref}$	Reference relative permeability dyadic
ν_0	Distance between origins of two coordinate systems
σ, σ'	Dummy indexes

continued on next page

continued

$\left[\underline{\underline{\tau}}\right]$, $\left[\underline{\underline{\hat{\tau}}}\right]$	4×4 transmission matrixes for axial wave propagation
ϕ	Twist angle
φ	Phase of planewave reflection coefficient
χ_s	Tilt angle
ω	Angular frequency
$\omega_{a,b,c}$	Resonant frequencies
$\Delta\lambda_0^{\mathrm{Br}}$	FWHM bandwidth of Bragg regime
$\mathbf{\Delta}_i$	First moment of energy density of $\mathbf{E}_i$
$\mathbf{\Delta}_r^{(n)}$	First moment of energy density of $\mathbf{E}_r^{(n)}$
$\left[\underline{\underline{\Theta}}(b)\right]$	Perturbing term of $\left[\underline{\underline{\hat{\tau}}}\right]$
Λ_x, Λ_z	Equivalent periods along x and z axes
Ψ	Angular–spectrum function
Ω	Structural half–period
$[\underline{\mathcal{A}}]$	2–column vector containing amplitudes of the LCP and RCP components of incident field for axial wave propagation
$[\underline{\mathcal{R}}]$	2–column vector containing amplitudes of the LCP and RCP components of reflected field for axial wave propagation
$[\underline{\mathcal{T}}]$	2–column vector containing amplitudes of the LCP and RCP components of transmitted field for axial wave propagation
$\underline{\underline{\mathfrak{R}}}_{\mathrm{L}}^{(n)}$, $\underline{\underline{\mathfrak{R}}}_{\mathrm{R}}^{(n)}$	Reflection dyadics
$\underline{\underline{\mathfrak{T}}}_{\mathrm{L}}^{(n)}$, $\underline{\underline{\mathfrak{T}}}_{\mathrm{R}}^{(n)}$	Transmission dyadics
$\mathbb{R}^3$	3D real space
$\mathbb{Z}$	Set of all integers
$[\underline{0}]_m$	m–column null vector
$\left[\underline{\underline{0}}\right]_m$	$m \times m$ null matrix

continued on next page

continued

$\|\|\,.\,\|\|$	L_∞–norm of a matrix

List of Figures

Acknowledgements

I gratefully acknowledge the guidance provided by my advisor, Professor Akhlesh Lakhtakia. I hope this thesis is sufficient evidence of the fact that working with him has indeed been an intellectual experience. Beyond being an advisor, he has also been a counselor and friend of mine and I offer my heartfelt and sincerest thanks to him for the influence he has had on me.

I would also like to thank Professor Russell F. Messier for serving as a co–advisor, particularly during my initial graduate studies. My thanks are also due to Professor Mark W. Horn for invaluable discussions on microlithography in summer research.

I offer my thanks to Professors Bernhard R. Tittmann and Venkatraman Gopalan for serving on my committee and their valuable suggestions to improve this thesis.

Special thanks are due to Mrs. Josephine and Mr. William L. Weiss and Professors Judith A. Todd and Richard P. McNitt of Department of Engineering Science and Mechanics for generously providing me financial support during the course of this work. Computing assistance from Mr. Abdul H. Aziz of the Penn State Institute for High Performance Computing Applications is also deeply appreciated.

Finally, I would like to acknowledge my sincere appreciation to my parents who have always encouraged me to turn my dreams into reality. I am greatly indebted to my wife Xiaoli and my daughter Christine for their patience and love during my graduate studies.

Chapter 1

Introduction

1.1 Sculptured Thin Films

1.1.1 A General Picture

The concept of sculptured thin films (STFs) and an associated technology for optics emerged during the 1990s from the widely used columnar thin films (CTFs) [1]–[3]. The ideal morphology of CTFs consists of almost identical, straight, and parallel nanowires of elliptical cross–section. The nanowires in a STF are not straight, but are made to grow as curves that veer away from the substrate [4]–[6], as shown in Figure 1.1. The nanowire diameters range from about 10 to 100 nm, and a wide variety of such morphologies are realizable through instantaneous variation in the growth direction of nanowires during physical vapor deposition (PVD) [7, 8].

Two canonical classes of STF morphologies — nematic and helicoidal — are obtainable by choosing the proper axis of rotation of the substrate during PVD. Nematic morphologies are two–dimensional (2D), ranging from the simple chevrons to the more complex C and S shapes. Helicoidal morphologies are three–dimensional (3D), including helical and

superhelical [9]. More complex morphologies and multisection STFs, in which the chemical composition or/and the nanowire shape varies from section to section along the thickness direction, can also be realized on large–area substrates [10, 11]. The two–section STF, illustrated in Figure 1.2 as an example, comprises helical nanowires in the lower section and chevronic nanowires in the upper section.

A wide variety of materials can be used for PVD of STFs, ranging from insulators (e.g., oxides and fluorides) to semiconductors (e.g., crystalline silicon) to metals (e.g., aluminum and chromium). This diversity reflects the low degree of sensitivity of morphology obtained by PVD to chemical composition. In fact, as predicted by the structure zone model of Thornton [12], the morphology obtained through PVD is largely a consequence of obeying simple geometric rules of atomic aggregation, when little or no surface diffusion is involved — which explains why essentially similar morphologies can be generated from a broad range of material sources.

Being porous, STFs contain voids of characteristic shapes and sizes. As these voids can be filled with different materials, STFs can function in many different ways. For examples, the fabrication of low–permittivity nanocomposites for the microelectronics industry has been suggested using STF technology [13], and proof–of–concept optical fluid sensors have been designed and fabricated to exploit the textured porosity of STFs [14, 15].

In order to fully harness STF technology, an electromagnetic model of STFs needs to be established with the capability to account for structure–property relationships. In the macroscopic sense, a STF is a unidirectionally nonhomogeneous, bianisotropic continuum in the optical regime. In the microscopic sense, a STF is viewed as a composite material with at least two different material phases molded into the sculptured morphology. The relationship between the nanostructure and the macroscopic constitutive properties needs to be quantitatively delineated and understood. For that purpose, a nominal model has been developed to determine the constitutive dyadics of STFs from local homogenization

of electrically small ellipsoidal particles of different material phases [16]–[19]. Intelligent design and fabrication of STF devices are made possible by coupling this nominal model with experimentation [18].

1.1.2 Growth of STFs

In general, STFs are fabricated by directional PVD methods, such as evaporation in high–vacuum conditions or by sputtering at intermediate–vacuum conditions. The schematic of a basic system for PVD of STFs on planar substrates is presented in Figure 1.3. There are two fundamental axes of rotation of the substrate: one (z axis) is perpendicular to the substrate plane (xy plane), and the other (y axis) is parallel to the substrate plane. The incident vapor flux makes an oblique angle χ_v to the substrate plane.

The growth of a STF starts with the process of nucleation and involves continuous renucleation thereafter. These processes are controlled through the proper choice of PVD parameters — such as energy of bombarding particles, substrate temperature, and χ_v. Once the growth reaches a steady state, the nanowire shapes can be tailored by controlling the rotation of substrate. For example, nematic STFs are attained by rotating the substrate about the y axis [20], while helicoidal STFs are formed with the substrate rotation about the z axis [21, 22]. The mass density of helicoidal STFs is expected not to vary in the thickness direction since χ_v is fixed during growth, so long as the nanowires attain a steady–state diameter in the early nucleation and growth stages. By changing the rotational speed and the orientation of the substrate sequentially without halting deposition, multisection STFs have been fabricated with cascaded morphologies in the thickness direction [10, 11].

1.1.3 Canonical Delineation of STFs

The macroscopic conception of STFs in the optical regime is as unidirectionally nonhomogeneous, bianisotropic continuums, with the linear constitutive relations

$$\left.\begin{aligned} \mathbf{D}(\mathbf{r},\omega) &= \epsilon_0[\underline{\underline{\epsilon}}(z,\omega)\cdot\mathbf{E}(\mathbf{r},\omega) + \underline{\underline{\alpha}}(z,\omega)\cdot\mathbf{H}(\mathbf{r},\omega)] \\ \mathbf{B}(\mathbf{r},\omega) &= \mu_0[\underline{\underline{\beta}}(z,\omega)\cdot\mathbf{E}(\mathbf{r},\omega) + \underline{\underline{\mu}}(z,\omega)\cdot\mathbf{H}(\mathbf{r},\omega)] \end{aligned}\right\} \tag{1.1}$$

indicating that the axis of nonhomogeneity is parallel to the z axis. In (1.1) and hereafter, $\mathbf{E}(\mathbf{r},\omega)$ and $\mathbf{H}(\mathbf{r},\omega)$ are the electric and magnetic field phasors, respectively; $\mathbf{D}(\mathbf{r},\omega)$ and $\mathbf{B}(\mathbf{r},\omega)$ are the electric and magnetic displacement phasors, respectively; an $\exp(-i\omega t)$ time–dependence is implicit, with $i=\sqrt{-1}$, ω as the angular frequency of light, and t as time; $\mathbf{r} = x\mathbf{u}_x + y\mathbf{u}_y + z\mathbf{u}_z$ is the position vector, with $\mathbf{u}_x$, $\mathbf{u}_y$ and $\mathbf{u}_z$ as unit cartesian vectors; and $\epsilon_0 = 8.854\times10^{-12}$ F m^{-1} and $\mu_0 = 4\pi\times10^{-7}$ H m^{-1} are the permittivity and permeability of free space, respectively. The electric and magnetic properties of STFs are expressed through the relative permittivity dyadic $\underline{\underline{\epsilon}}(z,\omega)$ and the relative permeability dyadic $\underline{\underline{\mu}}(z,\omega)$, respectively; while the magnetoelectric properties are expressed through the relative magnetoelectricity dyadics $\underline{\underline{\alpha}}(z,\omega)$ and $\underline{\underline{\beta}}(z,\omega)$. These four constitutive dyadics in (1.1) have to be modeled with guidance from morphology.

In the macroscopic sense, the STF morphology is delineated by a unaxially rotational dyadic $\underline{\underline{\mathrm{S}}}(z)$, which is a composition of the following three elementary rotational dyadics:

$$\underline{\underline{\mathrm{S}}}_x(z) = \mathbf{u}_x\mathbf{u}_x + (\mathbf{u}_y\mathbf{u}_y + \mathbf{u}_z\mathbf{u}_z)\cos\zeta_x(z) + (\mathbf{u}_z\mathbf{u}_y - \mathbf{u}_y\mathbf{u}_z)\sin\zeta_x(z)\,, \tag{1.2}$$

$$\underline{\underline{\mathrm{S}}}_y(z) = \mathbf{u}_y\mathbf{u}_y + (\mathbf{u}_x\mathbf{u}_x + \mathbf{u}_z\mathbf{u}_z)\cos\zeta_y(z) + (\mathbf{u}_z\mathbf{u}_x - \mathbf{u}_x\mathbf{u}_z)\sin\zeta_y(z)\,, \tag{1.3}$$

$$\underline{\underline{\mathrm{S}}}_z(z) = \mathbf{u}_z\mathbf{u}_z + (\mathbf{u}_x\mathbf{u}_x + \mathbf{u}_y\mathbf{u}_y)\cos\zeta_z(z) + (\mathbf{u}_y\mathbf{u}_x - \mathbf{u}_x\mathbf{u}_y)\sin\zeta_z(z)\,. \tag{1.4}$$

Here, $\zeta_x(z)$, $\zeta_y(z)$ and $\zeta_z(z)$ are angular functions indicating rotations about the x, y and z axes, respectively. Accordingly, the linear constitutive relations of a single–section STF

are set up as follows:

$$\left.\begin{aligned}
\mathbf{D}(\mathbf{r},\omega) &= \epsilon_0 \underline{\underline{S}}(z) \cdot [\underline{\underline{\epsilon}}_{ref}(\omega) \cdot \underline{\underline{S}}^{T}(z) \cdot \mathbf{E}(\mathbf{r},\omega) + \underline{\underline{\alpha}}_{ref}(\omega) \cdot \underline{\underline{S}}^{T}(z) \cdot \mathbf{H}(\mathbf{r},\omega)] \\
\mathbf{B}(\mathbf{r},\omega) &= \mu_0 \underline{\underline{S}}(z) \cdot [\underline{\underline{\beta}}_{ref}(\omega) \cdot \underline{\underline{S}}^{T}(z) \cdot \mathbf{E}(\mathbf{r},\omega) + \underline{\underline{\mu}}_{ref}(\omega) \cdot \underline{\underline{S}}^{T}(z) \cdot \mathbf{H}(\mathbf{r},\omega)]
\end{aligned}\right\} . \qquad (1.5)$$

The dyadics $\underline{\underline{\epsilon}}_{ref}(\omega)$, etc., are termed *reference* relative constitutive dyadics that are spatially invariant, and the superscript ^{T} denotes the transpose. The constitutive equations (1.5) reflect the fact that the morphologies of a single–section STF in any two planes $z = z_1$ and $z = z_2$ are exactly interchangeable by a suitable rotation.

Canonical forms of STFs have been delineated. For example, by choosing $\underline{\underline{S}}(z) = \underline{\underline{S}}_y(z)$, (1.5) describes the canonical class of STFs with nematic morphology. The choice of $\underline{\underline{S}}(z) = \underline{\underline{S}}_z(z)$ gives rise to the canonical class of STFs with helicoidal morphology. Helicoidal STFs are exemplified by chiral STFs for which $\zeta_z(z) = \pm\pi z/\Omega$ in (1.4), where 2Ω is the structural period, and the $+/-$ signs indicate the structural right/left–handedness of the film. More complicated specifications of $\underline{\underline{S}}(z)$ are possible, as for the STFs with superhelical morphology [9].

On account of the inclination of the nanowires with respect to z axis, it is appropriate to delineate $\underline{\underline{\epsilon}}_{ref}(\omega)$, etc., in terms of the reference unit vectors

$$\left.\begin{aligned}
\mathbf{u}_\tau &= \mathbf{u}_x \cos\chi_s + \mathbf{u}_z \sin\chi_s \\
\mathbf{u}_n &= -\mathbf{u}_x \sin\chi_s + \mathbf{u}_z \cos\chi_s \\
\mathbf{u}_b &= -\mathbf{u}_y
\end{aligned}\right\} , \qquad (1.6)$$

where χ_s is called the tilt angle. The specification

$$\underline{\underline{\sigma}}_{ref}(\omega) = \sigma_a(\omega)\mathbf{u}_n\mathbf{u}_n + \sigma_b(\omega)\mathbf{u}_\tau\mathbf{u}_\tau + \sigma_c(\omega)\mathbf{u}_b\mathbf{u}_b\,, \quad \sigma \in (\epsilon, \alpha, \beta, \mu) \qquad (1.7)$$

is in accord with the local orthorhombicity of STFs, as illustrated in Figure 1.4. In fact, if the nanowire cross–section is circular, $\sigma_a(\omega) = \sigma_c(\omega)$ and the unit vectors $\mathbf{u}_n$ and $\mathbf{u}_b$ can be chosen arbitrarily in the cross–section plane of the nanowire (Figure 1.4(a)). When the nanowire cross–section is elliptical, $\sigma_a(\omega) \neq \sigma_c(\omega)$ and the unit vectors $\mathbf{u}_n$ and $\mathbf{u}_b$ should

be along the two principal axes of the cross–section ellipse (Figure 1.4(b)). More generally, the nanowire cross–section can be of any convex shape defined by

$$\mathbf{r}_s = \underline{\underline{\mathrm{U}}}(\theta) \cdot \mathbf{u}_r(\theta)\,. \tag{1.8}$$

Here, $\mathbf{u}_r(\theta)$ is the radial unit vector in a two–dimensional polar coordinate system and $\underline{\underline{\mathrm{U}}}(\theta)$ is the 2×2 shape dyadic which is assumed to real symmetric because of the convexity of the cross–section. Clearly, the determination of the in–plane dyadic $\underline{\underline{\sigma}}^{||}_{ref}(\omega)$ — which is the projection of $\underline{\underline{\sigma}}_{ref}(\omega)$ in the nanowire cross–section plane — through (1.8) can be achieved by a local homogenization procedure (e.g., Bruggeman formalism) detailed elsewhere [16]–[19]. However, because $\underline{\underline{\mathrm{U}}}(\theta)$ is real symmetric, it can be shown that $\underline{\underline{\sigma}}^{||}_{ref}(\omega)$ should be a symmetric 2×2 dyadic which can be diagonalized as

$$\underline{\underline{\sigma}}^{||}_{ref}(\omega) = \underline{\underline{\mathrm{V}}}(\omega) \cdot \underline{\underline{\sigma}}^{||}_{diag}(\omega) \cdot \underline{\underline{\mathrm{V}}}^{\mathrm{T}}(\omega)\,, \quad \sigma \in (\epsilon, \alpha, \beta, \mu)\,. \tag{1.9}$$

Here, $\underline{\underline{\sigma}}^{||}_{diag}(\omega)$ is the 2×2 diagonal dyadic whose two nonzero entries determine the values of $\sigma_a(\omega)$ and $\sigma_c(\omega)$; and $\underline{\underline{\mathrm{V}}}(\omega)$ is the 2×2 orthogonal dyadic comprising the normalized eigenvectors of $\underline{\underline{\sigma}}^{||}_{ref}(\omega)$. By choosing the in–plane unit vectors $\mathbf{u}_n$ and $\mathbf{u}_b$ as the two normalized eigenvectors contained in $\underline{\underline{\mathrm{V}}}(\omega)$, $\underline{\underline{\sigma}}_{ref}(\omega)$ can still be expressed as per (1.7), which is tantamount to the local orthorhombicity of STFs in general (Figure 1.4(c)). By choosing $\sigma_a(\omega) \neq \sigma_b(\omega) \neq \sigma_c(\omega)$ in general for $\underline{\underline{\sigma}}_{ref}(\omega)$, the density anisotropy occurring during PVD is thus also taken into account [1].

For magneto–optics, gyrotropic terms such as $i\sigma_g(\omega)\mathbf{u}_\tau \times \underline{\underline{\mathrm{I}}}$ can be included in (1.7), where $\underline{\underline{\mathrm{I}}}$ is the identity dyadic [23].

The Post constraint

$$\mathrm{Trace}\left\{\underline{\underline{\mu}}^{-1}_{\mathrm{ref}}(\omega)\left[\underline{\underline{\beta}}_{ref}(\omega) + \frac{\epsilon_0}{\mu_0}\underline{\underline{\alpha}}_{ref}(\omega)\right]\right\} \equiv 0 \tag{1.10}$$

is mandated by the Lorentz–Heaviside visualization of electromagnetic theory [24]. If $\underline{\underline{\epsilon}}_{ref}(\omega) = \underline{\underline{\epsilon}}^{\mathrm{T}}_{\mathrm{ref}}(\omega)$, $\underline{\underline{\mu}}_{ref}(\omega) = \underline{\underline{\mu}}^{\mathrm{T}}_{\mathrm{ref}}(\omega)$, and $\underline{\underline{\alpha}}_{ref}(\omega) = -\underline{\underline{\beta}}^{\mathrm{T}}_{\mathrm{ref}}(\omega)$, the STF is Lorentz–

reciprocal [25]. The simplest form of STFs is the purely dielectric one, so that $\underline{\underline{\mu}}_{ref}(\omega) = \underline{\underline{I}}$, whereas both $\underline{\underline{\alpha}}_{ref}(\omega)$ and $\underline{\underline{\beta}}_{ref}(\omega)$ are null dyadics.

1.1.4 From Nanostructure to Continuum

The constitutive relations (1.5) are set by viewing any STF as a continuous medium. The nanoscale information regarding morphology and composition needs to be reflected in this macroscopic model. As any STF is a composite material with at least two different material phases, the constitutive dyadics $\underline{\underline{\epsilon}}(z,\omega)$, etc., can be modeled through the commonly used procedure of homogenization, so long as the particulate dimensions of all material phases are much smaller than the wavelength of incident light [26]. However, as a STF is effectively nonhomogeneous in the z direction, the homogenization procedure must be implemented in the localized fashion, i.e., for any thin slice of the STF perpendicular to the z axis. But any two slices of a single–section STF are in fact identical, except for a rotational transformation captured by $\underline{\underline{S}}(z)$. Therefore, the local homogenization procedure for the STF can be performed for $\underline{\underline{\epsilon}}_{ref}(\omega)$, etc., but leading to the construction of $\underline{\underline{\epsilon}}(z,\omega)$, etc.

In a nominal model that has been developed during the last five years [16]–[19], the nanowires as well as interparticle voids/fillings in a STF are represented as parallel strings of electrically small ellipsoidal particles. Both ellipsoidal shape factors and the volumetric proportions of the material phases must be chosen for the implementation of local homogenization procedure. Once an algorithm for the macroscopic properties of the STF has been set up, calibration of this nominal model is possible by comparison of the predicted optical responses against measured data [18].

1.2 Chiral STFs

Chiral STFs are a subclass of helicoidal STFs that are periodically nonhomogeneous along the z axis. It is easy to fabricate them with periods specified between 50 nm and 2 μm. A of chiral STF is described by specifying $\underline{\underline{S}}(z) = \underline{\underline{S}}_z(z)$ in (1.5), along with $\zeta_z(z) = \pm\pi z/\Omega$. Modeled as purely dielectric substances, these have been the most popular STFs for optics till date.

1.2.1 Circular Bragg Phenomenon

The attraction of chiral STFs is attributed to the circular Bragg phenomenon evinced by them [9]. Briefly, a structurally right/left–handed chiral STF only a few periods thick reflects almost completely normally incident right/left circularly polarized (RCP/LCP) plane waves with wavelength lying in the so–called Bragg regime; while the reflection of normally incident LCP/RCP plane waves in the same regime is very little. A schematic of the circular Bragg phenomenon is presented in Figure 1.5.

Certainly, the circular Bragg phenomenon occurs for oblique incidence as well, but it is greatly influenced by the directionality of planewave incidence [27, 28]. For example, the Bragg regime shifts to shorter wavelengths as the polar angle of planewave incidence $\theta_{\rm i}^p$ (with respect to the z axis) increases in absolute value. The width of Bragg regime also decreases with increasing $|\theta_{\rm i}^p|$. The azimuthal angle of planewave incidence $\psi_{\rm i}^p$ (eith respect to the x axis in the xy plane) does not affect the Bragg regime strongly, but it does significantly affect properties of optical rotation and ellipticity in the Bragg regime. There is also a decrease in discrimination between LCP and RCP plane waves when $|\theta_{\rm i}^p|$ is very large [29].

A simple explanation of circular Bragg phenomenon for chiral STFs is provided by the application of coupled–wave theory for normal incidence [30, 31]: When the incident wave-

length is approximately equal to the optical period of the dielectric nonhomogeneity, the morphology of a chiral STF acts as a scalar Bragg grating for co–handed circularly polarized (CP) plane waves, but not for cross–handed circularly polarized plane waves. Rather, the chiral STF acts as a homogenous, isotropic, dielectric medium in the latter case. This discrimination of circularly polarized plane waves by chiral STFs can be harnessed in many different ways, so that optical applications of chiral STFs are abundant.

1.2.2 Optical Applications

Many optical applications of chiral STFs have been proposed and even realized to date. By utilizing the circular Bragg phenomenon, chiral STFs as circular polarization filters have been theoretically examined and then experimentally realized [9, 33]. A handedness–selective light inverter, which comprises a chiral STF and a CTF functioning as a half waveplate, was also designed and then fabricated and tested [34, 35]. By introducing either a layer defect or a twist defect in the middle of a chiral STF, narrowband spectral–hole filters have been designed and implemented [15, 36, 37]. The operational free–space wavelength of these filters is located in the Bragg regime for normal incidence, and is dependent on the nature of the defect.

Piezoelectrically tunable lasers made of dye–doped polymer chiral STFs have been recently proposed as a result of theoretical analysis of piezoelectric manipulation of chiral STFs [38]. Time–domain exhibition of the circular Bragg phenomenon is being studied, which would lead to the use of chiral STFs to shape optical pulses in optical communication systems [39, 40]. Being porous, chiral STFs are also useful for optically sensing humidity and various chemicals [15, 41, 42].

1.3 Slanted Chiral STFs

1.3.1 Genesis

The helical nanowires of a chiral STF stand upright on a substrate. Therefore, the optical periodicity of a chiral STF is unidirectional — along the normal to the substrate plane, i.e., the z axis. A chiral STF can be viewed as a volume grating that consists of infinitesimally thin dielectric sublayers. The constitutive properties are homogenous within each sublayer, but vary periodically from sublayer to sublayer to form a chiral architecture. The periodicity of the chiral architecture implies that a chiral STF is indeed a volume grating, albeit different from the ones usually studied [43].

There exists another type of gratings of great importance in optics, however. These are diffraction gratings [44]. The distinguishing feature of a diffraction grating is the periodic variation of constitutive properties in a plane, often achieved by periodically corrugating a planar sheet. In consequence of illumination by a plane wave, the reflected, the refracted, and the transmitted fields of a diffraction grating are discrete angular spectrums of propagating as well as evanescent plane waves — called the Floquet harmonics, on account of their emergence from the Floquet–Bloch theorem [45]. As either the frequency or the direction of incidence is altered, an evanescent Floquet harmonic of the reflected/refracted/transmitted field may turn into a propagating one or vice versa, this phenomenon being manifested as the so–called Rayleigh–Wood anomaly [44] in the remittance (i.e., reflectance and transmittance) spectrums.

Clearly, the coupling of these two types of gratings (i.e., volume and diffraction gratings) is likely to be rich in optical phenomenons and applications, the more so when the volume grating is sensitive to circular polarization. A direct outcome of the coupling is that the circular Bragg phenomenon would be affected by the nonspecular angular spectrums of diffraction as well as by the associated Rayleigh–Wood anomalies. In order to

physically achieve this coupling, slanted chiral STFs were conceptualized for this thesis as an extension of chiral STFs [46].

Morphologically, a slanted chiral STF comprises helical nanowires slanted at an angle $\alpha \neq 0$ to the normal to the substrate plane, as schematically illustrated in Figure 1.6. A possible way to attain this morphology is by rotating the substrate with a variable angular velocity during deposition [47, 48]. A slanted chiral STF will thus be unidirectionally and periodically nonhomogeneous along an axis inclined, but not perpendicular to the substrate plane.

Therefore, a slanted chiral STF is periodic along the z and the x axes as well. In order to represent the slanted morphology, $\underline{\underline{S}}(z)$ in (1.5) is replaced by

$$\underline{\underline{S}}(\mathbf{r}) = \underline{\underline{s}}_y(-\alpha) \cdot \underline{\underline{s}}_z(\mathbf{r}) \,, \tag{1.11}$$

where

$$\underline{\underline{s}}_y(\alpha) = \mathbf{u}_y \mathbf{u}_y + (\mathbf{u}_x \mathbf{u}_x + \mathbf{u}_z \mathbf{u}_z) \cos\alpha + (\mathbf{u}_z \mathbf{u}_x - \mathbf{u}_x \mathbf{u}_z) \sin\alpha \tag{1.12}$$

is similar to $\underline{\underline{S}}_y(z)$, while

$$\underline{\underline{s}}_z(\mathbf{r}) = \mathbf{u}_z \mathbf{u}_z + (\mathbf{u}_x \mathbf{u}_x + \mathbf{u}_y \mathbf{u}_y) \cos\left[\frac{\pi}{\Omega}(\mathbf{r} \cdot \mathbf{u}_\ell)\right] + h(\mathbf{u}_y \mathbf{u}_x - \mathbf{u}_x \mathbf{u}_y) \sin\left[\frac{\pi}{\Omega}(\mathbf{r} \cdot \mathbf{u}_\ell)\right] \tag{1.13}$$

is similar to $\underline{\underline{S}}_z(z)$ except that the axis of nonhomogeneity is parallel to the unit vector

$$\mathbf{u}_\ell = \sin\alpha \, \mathbf{u}_x + \cos\alpha \, \mathbf{u}_z \,. \tag{1.14}$$

Therefore, $\underline{\underline{s}}_z(\mathbf{r})$ in (1.13) is a function of both x and z, and the structural handedness is specified through the parameter $h = \pm 1$.

The constitutive relations of a single–section slanted chiral STF are thereby written as

$$\left.\begin{aligned}
\mathbf{D}(\mathbf{r},\omega) = \epsilon_0 \underline{\underline{s}}_y(-\alpha) \cdot \underline{\underline{s}}_z(\mathbf{r}) \cdot \Big[& \underline{\underline{\epsilon}}_{ref}(\omega) \cdot \underline{\underline{s}}_z^{\mathrm{T}}(\mathbf{r}) \cdot \underline{\underline{s}}_y^{\mathrm{T}}(-\alpha) \cdot \mathbf{E}(\mathbf{r},\omega) \\
& + \underline{\underline{\alpha}}_{ref}(\omega) \cdot \underline{\underline{s}}_z^{\mathrm{T}}(\mathbf{r}) \cdot \underline{\underline{s}}_y^{\mathrm{T}}(-\alpha) \cdot \mathbf{H}(\mathbf{r},\omega) \Big] \\
\mathbf{B}(\mathbf{r},\omega) = \mu_0 \underline{\underline{s}}_y^{\mathrm{T}}(-\alpha) \cdot \underline{\underline{s}}_z(\mathbf{r}) \cdot \Big[& \underline{\underline{\beta}}_{ref}(\omega) \cdot \underline{\underline{s}}_z^{\mathrm{T}}(\mathbf{r}) \cdot \underline{\underline{s}}_y^{\mathrm{T}}(-\alpha) \cdot \mathbf{E}(\mathbf{r},\omega) \\
& + \underline{\underline{\mu}}_{ref}(\omega) \cdot \underline{\underline{s}}_z^{\mathrm{T}}(\mathbf{r}) \cdot \underline{\underline{s}}_y^{\mathrm{T}}(-\alpha) \cdot \mathbf{H}(\mathbf{r},\omega) \Big]
\end{aligned}\right\} . \tag{1.15}$$

Clearly from (1.12) to (1.15), a slanted chiral STF couples the two types of gratings in its constitutive properties, and the slant angle $\alpha \neq 0$ totally controls this coupling. In the remainder of the thesis, $\underline{\underline{\mu}}_{ref}(\omega) = \underline{\underline{I}}$ while $\underline{\underline{\alpha}}_{ref}(\omega)$ and $\underline{\underline{\beta}}_{ref}(\omega)$ are null dyadics, for simplicity as well as in accord with the dielectric nature of most optical films.

1.3.2 Optics of Slanted Chiral STFs

The basic feature of slanted chiral STFs is likely to be visualized best in terms of the planewave response. The circular Bragg phenomenon may occur nonspecularly due to the dual–periodicity in morphology. Affected by the slant angle α, the circular Bragg phenomenon could become even tunable in both spectrum and direction; and many different optical applications could arise.

Apart from the commonplace planewave excitation, finite sources of excitation (e.g., evanescent waves, nonparaxial optical beams, and point dipoles) are being widely used in nano–optics research [49, 50]. While evanescent waves are essential to near–field optics, oriented dipolar sources are useful for modeling nanoprobes in near–field scanning microscopy as well as for near–field lithography in optoelectronics [51, 52]. Radiation from these finite sources is likely to be responded by slanted chiral STFs in a distinctive fashion that not only incorporates all the features displayed in analogy by planewave excitation, but also encompasses optical phenomenons that would be new and valuable in nanotechnology.

Furthermore, structural defects parallel to the substrate plane could be easily incorporated into the nanostructure of slanted chiral STFs. These structural defects generally produce a wave resonance localized inside the Bragg regime or at its edges. Both frequency and polarization characteristics of wave resonance have been harnessed for the design of narrowband optical filters in chiral STFs [36, 37], and low–threshold lasers and low–loss waveguides are also possible for being devised therefrom [53]–[55]. There is a

crossover phenomenon associated with the localization of wave resonance in both chiral STFs [56] and cholesteric liquid crystals (CLCs) [57]–[59]: The localization is seen as a co–handed reflectance hole when the chiral structure is relatively thin, but as a cross–handed transmission hole when the thickness is large. No doubt, this phenomenon would also be found in slanted chiral STFs in the presence of some types of defects. Exploitation of the crossover phenomenon for new devices is also possible, as exemplified by the design of a superior filter by combining both layer and twist defects in a chiral STF [56].

1.4 Outline of Thesis

The main objective of this thesis is to couple the characteristic optical responses of volume and diffraction gratings in the architecture of STFs. For that purpose, slanted chiral STFs are proposed. Theoretical analyses of their optical responses to both plane waves and finite sources are presented. A simple method to deal with beam propagation is to represent an optical beam as an angular spectrum of propagating and evanescent plane waves. The planewave response of slanted chiral STFs must then be characterized before analyzing their responses to optical beams, dipolar sources, as well as other finite sources.

The remainder of this thesis is organized according to the following plan. Chapter 2 presents a theoretical treatment of planewave diffraction by slanted chiral STFs. By exploiting the periodicity along the axis of nonhomogeneity, a rigorous coupled–wave analysis (RCWA) is undertaken to devise a numerical solution procedure. RCWA is chosen as the solution tool chiefly because of its simplicity and its consistency with the structure of electromagnetic theory [60, 61]. It is commonly used for computation of planewave diffraction by superlattices and diffraction gratings. However, the RCWA implementation in Chapter 2 has novel features for easier application to slanted chiral STFs.

The planewave response of a slanted chiral STF is presented in Chapters 3 and 4,

respectively, under normal–incidence and oblique–incidence conditions. The distinctive features of the circular Bragg phenomenon as displayed by a slanted chiral STF are contrasted with those of a chiral STF in Chapter 3. The effect of directionality of planewave incidence on the circular Bragg phenomenon is discussed in Chapter 4.

The wave resonance in a slanted chiral STF with a central twist defect is presented in Chapter 5, focusing on the crossover phenomenon as seen in the evolution of two types of spectral holes in the Bragg regime.

Theoretically, the phenomenon of wave resonance in a chiral STF with a central 90°–twist defect is re–constructed in Chapter 6, but with an analytical approach. Based on the coupled–wave theory (CWT), an approximate but closed–form solution for axial wave propagation in a chiral STF is derived in terms of a 4×4 CWT transmission matrix. The crossover phenomenon due to a central 90°–twist defect in a chiral STF is explained by the spectral characteristics of transmission matrix. A similar explanation is expected hold for a slanted chiral STF with a central twist defect.

The response of slanted chiral STFs to optical beams is dealt with in Chapter 7. Diffraction of 3D optical beams by slanted chiral STFs is formulated in terms of the spectral superposition of planewave diffractions. The reflected/refracted/transmitted field is a discrete spectrum of beams (each of which is an angular spectrum of plane waves) that are tagged with different Floquet–harmonic orders. Lateral shifts of the reflected beams would occur on Bragg reflection as well as on total reflection. For the latter case, the lateral shift is named as the Goos–Hänchen shift [62]. Being comparable with the dimensions of nanoengineered features, the Goos–Hänchen shift must not be neglected in nanotechnology [63].

The electromagnetic interaction of dipolar sources with slanted chiral STFs is discussed in Chapter 8. Dyadic Green functions (DGFs) are synthesized for reflection and transmission by a slanted chiral STF irradiated by Beltrami dipolar sources. The technique of

angular–planewave–spectrum representation is employed to facilitate calculation of radiation patterns in the far–zone.

The results of these studies is briefly summarized in Chapter 9, which concludes this thesis with a sketch of future research possibilities.

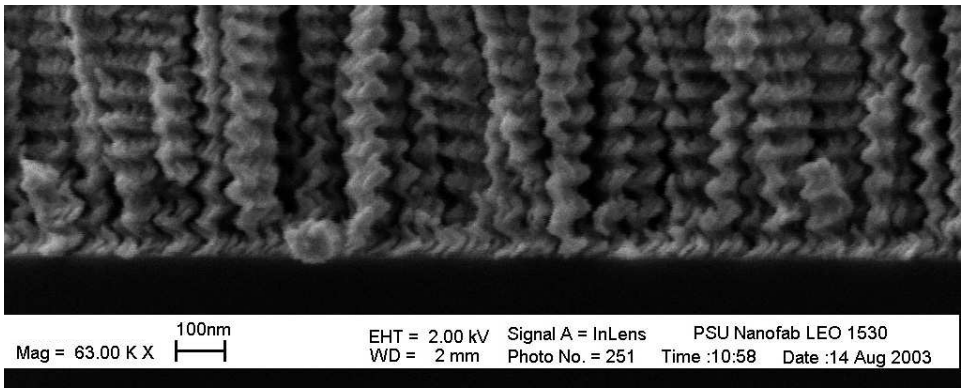

Figure 1.1: Scanning electron micrograph of a chiral STF of silicon oxide. This thin film is an assembly of parallel helical nanowires. (Courtesy: Mark W. Horn, Pennsylvania State University)

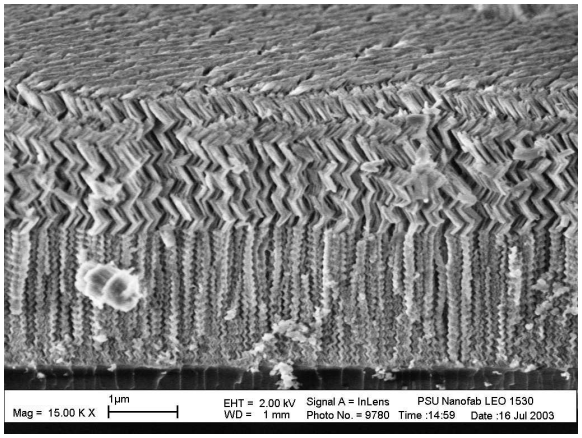

Figure 1.2: Scanning electron micrograph of a two–section STF of silicon oxide. This thin film comprises helical nanowires (3D) in the lower section and chevronic nanowires (2D) in the upper section. (Courtesy: Mark W. Horn, Pennsylvania State University)

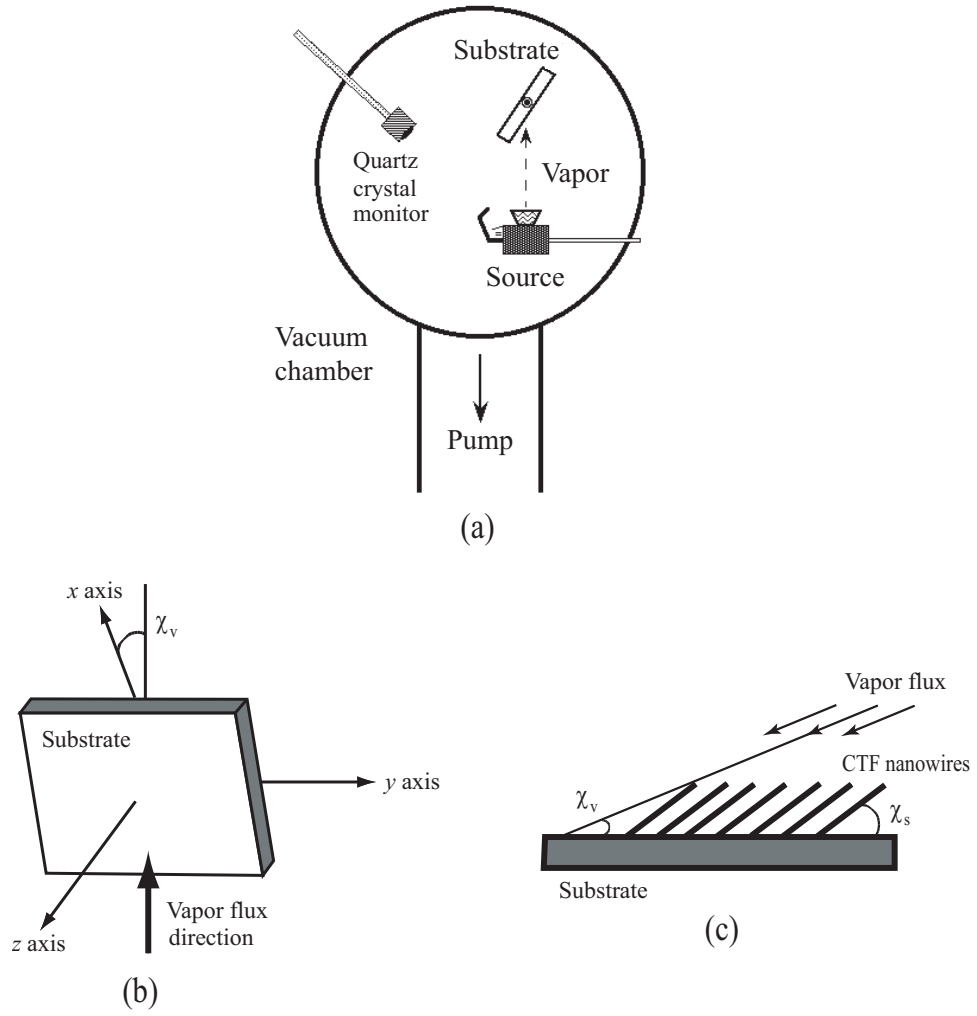

Figure 1.3: (a) Schematic of the basic system for PVD of STFs on planar substrates. (b) Coordinate system with the y and the z axes indicated as the two fundamental axes of rotation of the substrate. (c) Vapor incidence angle χ_v and the tilt angle χ_s.

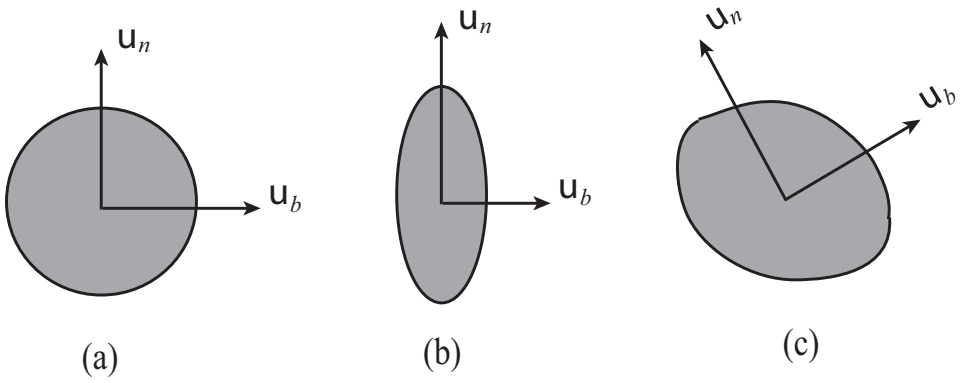

Figure 1.4: Local orthorhombicity of STFs as implied by nanowire cross–sections of STFs. The shape of nanowire cross–section is (a) circular, (b) elliptical, and (c) arbitrarily convex.

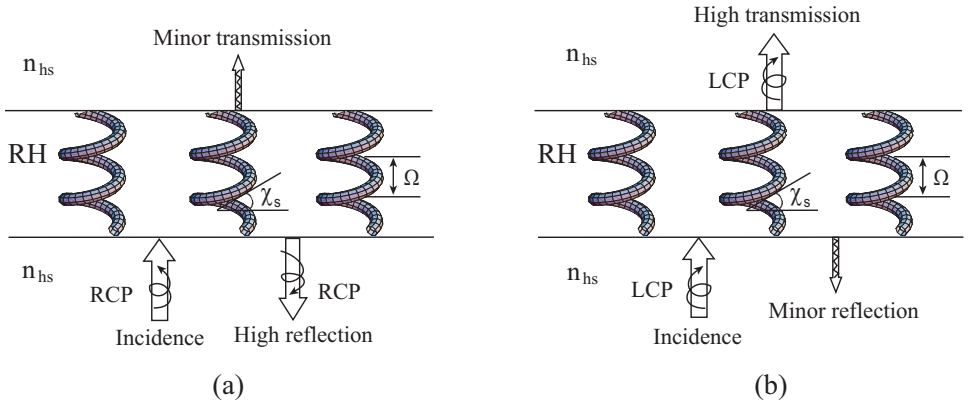

Figure 1.5: Schematic of circular Bragg phenomenon exhibited by a chiral STF. The chiral STF is right–handed (RH), while the normally incident plane wave is either (a) RCP or (b) LCP. Reflection and transmission occur in the two half–spaces occupied by a homogeneous, isotropic, and dielectric medium of refractive index n_{hs}.

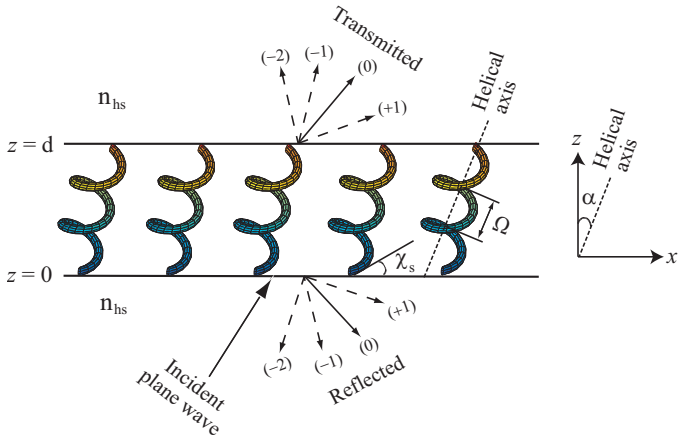

Figure 1.6: Schematic of the boundary value problem involving a slanted chiral STF. Specular reflection and transmission carry the label $n = 0$ and are identified by solid arrows, while nonspecular reflection and transmission carry the labels $n \neq 0$ and are identified by dashed arrows.

Chapter 2

Rigorous Coupled–Wave Analysis for Slanted Chiral STFs[‡]

Rigorous coupled–wave analysis (RCWA) is a relatively straightforward and semianalytical technique for solution of the Maxwell postulates for planewave diffraction by superlattices and diffraction gratings [60, 61]. It is a noniterative, deterministic technique utilizing a state–variable approach, and provides a convergent solution in terms of infinite series of Floquet harmonics without inherent numerical instabilities. A remarkable advantage of the RCWA is its internal consistency: Many constraints, such as those of energy conservation and reciprocity, are satisfied even with the truncation of the series of Floquet harmonics [61].

In contrast to the ordinary diffraction gratings that are periodic parallel to the substrate plane, a slanted chiral STF is periodic along an axis that is inclined to the substrate plane. Therefore, RCWA for planewave diffraction by slanted chiral STFs must be implemented in a different way than for ordinary procedures. Hence, the objective of this chapter is to

[‡] This chapter is partly adapted from the following paper: F. Wang, A. Lakhtakia, "Lateral shifts of optical beams on reflection by slanted chiral sculptured thin films", Opt. Commun. **235** 107–132 (2004).

establish a robust implementation of RCWA for the planewave responses of slanted chiral STFs.

2.1 Geometry of the Basic Problem

Let the region $0 \leq z \leq d$ be occupied by a slanted chiral STF, as shown in Figure 1.6, while the half–spaces $z \leq 0$ and $z \geq d$ are filled with a homogeneous, isotropic, and dielectric medium of refractive index n_{hs}. The general constitutive relations of a single–section slanted chiral STFs have been specified in (1.15). However, the focus hereafter is on dielectric slanted chiral STFs for which

$$\left.\begin{aligned} \mathbf{D}(\mathbf{r},\omega) &= \epsilon_0 \underline{\underline{\epsilon}}(\mathbf{r},\omega) \cdot \mathbf{E}(\mathbf{r},\omega) \\ \mathbf{B}(\mathbf{r},\omega) &= \mu_0 \mathbf{H}(\mathbf{r},\omega) \end{aligned}\right\}, \quad 0 < z < d\,, \tag{2.1}$$

where the relative permittivity dyadic

$$\underline{\underline{\epsilon}}(\mathbf{r},\omega) = \underline{\underline{s}}_y(-\alpha) \cdot \underline{\underline{s}}_z(\mathbf{r}) \cdot \underline{\underline{\epsilon}}_{ref}(\omega) \cdot \underline{\underline{s}}_z^{\mathrm{T}}(\mathbf{r}) \cdot \underline{\underline{s}}_y^{\mathrm{T}}(-\alpha)\,. \tag{2.2}$$

The reference relative permittivity dyadic $\underline{\underline{\epsilon}}_{ref}(\omega)$ in (2.2) can be visualized either from a microscopic perspective or from a phenomenological perspective. Microscopic modeling of $\underline{\underline{\epsilon}}_{ref}(\omega)$ takes account of the nanostructure, and links it to macroscopic observables. As exemplified by a nominal model for chiral STFs [16]–[19], $\underline{\underline{\epsilon}}_{ref}(\omega)$ can be derived from a local homogenization procedure by viewing a STF as an ensemble of oriented ellipsoidal particles of different material phases. The Bruggeman formalism is used to implement a local homogenization procedure in this model, but other formalisms can also be used [26].

From the macroscopic point of view, a dielectric STF is locally orthorhombic in most cases [6, 9]. Therefore, $\underline{\underline{\epsilon}}_{ref}(\omega)$ is set up as

$$\underline{\underline{\epsilon}}_{ref}(\omega) = \epsilon_a\, \mathbf{u}_n \mathbf{u}_n + \epsilon_b\, \mathbf{u}_\tau \mathbf{u}_\tau + \epsilon_c\, \mathbf{u}_b \mathbf{u}_b\,. \tag{2.3}$$

Most simply, the scalars $\epsilon_{a,b,c}(\omega)$ are assumed to emerge from a single–resonance Lorentzian model [64, 65] such that

$$\epsilon_\sigma(\omega) = 1 + \frac{p_\sigma}{\left[1 + \left(\mathrm{N}_\sigma^{-1} - i\,\omega_\sigma^{-1}\,\omega\right)^2\right]}\,, \quad \sigma = a, b, c\,. \tag{2.4}$$

Here, the parameters $p_{a,b,c}$ are the oscillator strengths, while $\omega_{a,b,c}$ and $\mathrm{N}_{a,b,c}$ determine the resonance frequencies and absorption linewidths. For later convenience, the composite scalar

$$\epsilon_d = \frac{\epsilon_a\,\epsilon_b}{\cos^2\chi_s\,\epsilon_a + \sin^2\chi_s\,\epsilon_b} \tag{2.5}$$

is introduced, which, combined with ϵ_c, suffices for optical investigations of axially excited chiral STFs [30]–[33].

For slanted chiral STFs, the restriction $|\alpha| < \chi_s$ should be made because the nanowires must always grow upwards in relation to the substrate plane [46]. Specially, $\alpha = 0$ specifies chiral STFs with the consequent reduction $\underline{\underline{\epsilon}}(\mathbf{r}, \omega) \to \underline{\underline{\epsilon}}(z, \omega)$ in (2.2). From here onwards, the dependences of various quantities on ω are implicit. Instead, the dependences on the free–space wavelength $\lambda_0 = 2\pi/\omega\sqrt{\mu_0\epsilon_0}$ may be written explicitly for emphasis.

2.1.1 Field Representation

A plane wave is incident from the half–space $z \leq 0$ on to the plane $z = 0$. As a result, reflection and transmission into the two half–spaces occur. Let the incident plane wave propagate with the wavevector $\mathbf{k}_+^{(0)} = k_x^{(0)}\,\mathbf{u}_x + k_y^{(0)}\,\mathbf{u}_y + k_z^{(0)}\,\mathbf{u}_z$. The incident, reflected, and transmitted electromagnetic field phasors are expressed in sets of Floquet harmonics

respectively as [46]

$$\mathbf{E}_i = \sum_{n\in\mathbb{Z}} \left(\mathbf{L}_+^{(n)}\, a_{\mathrm{L}}^{(n)} + \mathbf{R}_+^{(n)}\, a_{\mathrm{R}}^{(n)}\right) \exp\left(i\mathbf{k}_+^{(n)}\cdot\mathbf{r}\right)\,, \quad z\le 0\,, \tag{2.6}$$

$$\mathbf{H}_i = \frac{-in_{hs}}{\eta_0} \sum_{n\in\mathbb{Z}} \left(\mathbf{L}_+^{(n)}\, a_{\mathrm{L}}^{(n)} - \mathbf{R}_+^{(n)}\, a_{\mathrm{R}}^{(n)}\right) \exp\left(i\mathbf{k}_+^{(n)}\cdot\mathbf{r}\right)\,, \quad z\le 0\,, \tag{2.7}$$

$$\mathbf{E}_r = \sum_{n\in\mathbb{Z}} \left(\mathbf{L}_-^{(n)}\, r_{\mathrm{L}}^{(n)} + \mathbf{R}_-^{(n)}\, r_{\mathrm{R}}^{(n)}\right) \exp\left(i\mathbf{k}_-^{(n)}\cdot\mathbf{r}\right)\,, \quad z\le 0\,, \tag{2.8}$$

$$\mathbf{H}_r = \frac{-in_{hs}}{\eta_0} \sum_{n\in\mathbb{Z}} \left(\mathbf{L}_-^{(n)}\, r_{\mathrm{L}}^{(n)} - \mathbf{R}_-^{(n)}\, r_{\mathrm{R}}^{(n)}\right) \exp\left(i\mathbf{k}_-^{(n)}\cdot\mathbf{r}\right)\,, \quad z\le 0\,, \tag{2.9}$$

$$\mathbf{E}_t = \sum_{n\in\mathbb{Z}} \left(\mathbf{L}_+^{(n)}\, t_{\mathrm{L}}^{(n)} + \mathbf{R}_+^{(n)}\, t_{\mathrm{R}}^{(n)}\right) \exp\left(i\mathbf{k}_+^{(n)}\cdot\tilde{\mathbf{r}}\right)\,, \quad z\ge d\,, \tag{2.10}$$

$$\mathbf{H}_t = \frac{-in_{hs}}{\eta_0} \sum_{n\in\mathbb{Z}} \left(\mathbf{L}_+^{(n)}\, t_{\mathrm{L}}^{(n)} - \mathbf{R}_+^{(n)}\, t_{\mathrm{R}}^{(n)}\right) \exp\left(i\mathbf{k}_+^{(n)}\cdot\tilde{\mathbf{r}}\right)\,, \quad z\ge d\,. \tag{2.11}$$

In (2.6)–(2.11) and hereafter, $\eta_0 = \sqrt{\mu_0/\epsilon_0}$ is the intrinsic impedance of free space; while $\left\{a_{\mathrm{L}}^{(n)},\, a_{\mathrm{R}}^{(n)}\right\}$, $\left\{r_{\mathrm{L}}^{(n)},\, r_{\mathrm{R}}^{(n)}\right\}$ and $\left\{t_{\mathrm{L}}^{(n)},\, t_{\mathrm{R}}^{(n)}\right\}$, respectively, are complex–valued amplitudes of the LCP and RCP components of the Floquet harmonic of order n of the incident, reflected, and transmitted fields. The symbol $\mathbb{Z}$ represents the set $\{0,\, \pm1,\, \pm2,\, \ldots\}$ of all integers, and $\tilde{\mathbf{r}} = \mathbf{r} - d\mathbf{u}_z$.

The wavevectors $\mathbf{k}_\pm^{(n)}$ as well as the circular polarization vectors $\mathbf{L}_\pm^{(n)}$ and $\mathbf{R}_\pm^{(n)}$ of the Floquet harmonic of order n are specified as

$$\mathbf{k}_\pm^{(n)} = k_x^{(n)}\mathbf{u}_x + k_y^{(0)}\mathbf{u}_y \pm k_z^{(n)}\mathbf{u}_z\,, \tag{2.12}$$

$$\mathbf{L}_\pm^{(n)} = \pm\left(i\mathbf{s}^{(n)} - \mathbf{p}_\pm^{(n)}\right)/\sqrt{2}\,, \tag{2.13}$$

$$\mathbf{R}_\pm^{(n)} = \mp\left(i\mathbf{s}^{(n)} + \mathbf{p}_\pm^{(n)}\right)/\sqrt{2}\,. \tag{2.14}$$

In these expressions, the vectors

$$\left.\begin{aligned} \mathbf{s}^{(n)} &= \tfrac{-k_y^{(0)}}{k_{xy}^{(n)}}\mathbf{u}_x + \tfrac{k_x^{(n)}}{k_{xy}^{(n)}}\mathbf{u}_y \\ \mathbf{p}_\pm^{(n)} &= \mp\tfrac{k_z^{(n)}}{k_0 n_{hs}}\left(\tfrac{k_x^{(n)}}{k_{xy}^{(n)}}\mathbf{u}_x + \tfrac{k_y^{(0)}}{k_{xy}^{(n)}}\mathbf{u}_y\right) + \tfrac{k_{xy}^{(n)}}{k_0 n_{hs}}\,\mathbf{u}_z \end{aligned}\right\} \tag{2.15}$$

help denote linearly polarized fields of s– and p–types, in electromagnetics literature [44], with respect to the wavevector $\mathbf{k}_{\pm}^{(n)}$. The scalars

$$\left.\begin{aligned} \kappa_x &= (\pi/\Omega)|\sin\alpha| \\ k_x^{(n)} &= k_x^{(0)} + n\kappa_x \\ k_z^{(n)} &= +\sqrt{k_0^2\, n_{hs}^2 - \left(k_{xy}^{(n)}\right)^2} \\ k_{xy}^{(n)} &= +\sqrt{\left(k_x^{(n)}\right)^2 + \left(k_y^{(0)}\right)^2} \end{aligned}\right\} \tag{2.16}$$

depend on the x–period $\Lambda_x = 2\Omega/|\sin\alpha|$ of the slanted chiral STF. The free–space wavenumber is denoted by $k_0 = \omega\sqrt{\mu_0\epsilon_0} = 2\pi/\lambda_0$.

The incident plane wave is the Floquet harmonic of order 0; hence, $a_{\mathrm{L}}^{(n)} = a_{\mathrm{R}}^{(n)} = 0\,\forall\, n \neq 0$. Since all $\left\{a_{\mathrm{L}}^{(n)},\, a_{\mathrm{R}}^{(n)}\right\}$ are supposed to be known, the amplitude sets $\left\{r_{\mathrm{L}}^{(n)},\, r_{\mathrm{R}}^{(n)}\right\}$ and $\left\{t_{\mathrm{L}}^{(n)},\, t_{\mathrm{R}}^{(n)}\right\}$ need to be determined by the solution of certain coupled–wave ordinary differential equations (ODEs) augmented by boundary conditions at $z = 0$ and $z = d$.

2.1.2 Coupled–Wave ODEs

The spatially periodic variation of $\underline{\underline{\epsilon}}(\mathbf{r})$ of (2.2) is represented by the Fourier series

$$\underline{\underline{\epsilon}}(\mathbf{r}) = \sum_{n\in\mathbb{Z}} \underline{\underline{\epsilon}}^{(n)} \exp\left[in\left(\kappa_x x + \kappa_z z\right)\right]\,, \quad 0 < z < d\,, \tag{2.17}$$

where

$$\underline{\underline{\epsilon}}^{(n)} = \sum_{\sigma,\sigma'} \epsilon_{\sigma\sigma'}^{(n)} \mathbf{u}_\sigma \mathbf{u}_{\sigma'}\,, \quad \sigma,\sigma' = x,y,z\,, \tag{2.18}$$

are constant–value dyadics; and $\kappa_z = (\pi/\Omega)\cos\alpha$ is in accord with the z–period $\Lambda_z = 2\Omega/\cos\alpha$ of the slanted chiral STF.

Wave propagation occurs inside the thin–film material such that the electromagnetic

field phasors everywhere can be decomposed as

$$\left.\begin{aligned}\mathbf{E}\left(\mathbf{r}\right) &= \sum_{n\in\mathbb{Z}}\left[\mathrm{E}_x^{(n)}\left(z\right)\mathbf{u}_x + \mathrm{E}_y^{(n)}\left(z\right)\mathbf{u}_y + \mathrm{E}_z^{(n)}\left(z\right)\mathbf{u}_z\right]\exp\left[i\left(k_x^{(n)}x + k_y^{(0)}y\right)\right]\\ \mathbf{H}\left(\mathbf{r}\right) &= \sum_{n\in\mathbb{Z}}\left[\mathrm{H}_x^{(n)}\left(z\right)\mathbf{u}_x + \mathrm{H}_y^{(n)}\left(z\right)\mathbf{u}_y + \mathrm{H}_z^{(n)}\left(z\right)\mathbf{u}_z\right]\exp\left[i\left(k_x^{(n)}x + k_y^{(0)}y\right)\right]\end{aligned}\right\}, \quad (2.19)$$

where $\mathrm{E}_{x,y,z}^{(n)}$ and $\mathrm{H}_{x,y,z}^{(n)}$ are unknown functions of z. Following Chateau and Hugonin [66], it is useful to define

$$\left.\begin{aligned}\tilde{\mathrm{E}}_\sigma^{(n)}(z) &= \mathrm{E}_\sigma^{(n)}(z)\exp(-in\kappa_z z)\\ \tilde{\mathrm{H}}_\sigma^{(n)}(z) &= \mathrm{H}_\sigma^{(n)}(z)\exp(-in\kappa_z z)\end{aligned}\right\}, \quad \sigma = x, y, z\,. \quad (2.20)$$

On substituting (2.17)–(2.20) in the frequency–domain Maxwell curl postulates

$$\left.\begin{aligned}\nabla\times\mathbf{E}\left(\mathbf{r}\right) &= i\omega\mu_0\,\mathbf{H}\left(\mathbf{r}\right)\\ \nabla\times\mathbf{H}\left(\mathbf{r}\right) &= -i\omega\epsilon_0\,\underline{\underline{\epsilon}}(\mathbf{r})\;\bullet\,\mathbf{E}\left(\mathbf{r}\right)\end{aligned}\right\}, \quad 0 < z < d\,, \quad (2.21)$$

and exploiting the orthogonalities of the functions $\exp(i\,\mathbf{k}_\pm^{(n)}\cdot\mathbf{r})$ across any plane $z =$ constant, coupled–wave ODEs

$$\frac{\mathrm{d}}{\mathrm{d}z}\tilde{\mathrm{E}}_x^{(n)}\left(z\right) + in\kappa_z\tilde{\mathrm{E}}_x^{(n)}\left(z\right) - ik_x^{(n)}\tilde{\mathrm{E}}_z^{(n)}\left(z\right) = ik_0\eta_0\tilde{\mathrm{H}}_y^{(n)}\left(z\right), \quad (2.22)$$

$$\frac{\mathrm{d}}{\mathrm{d}z}\tilde{\mathrm{E}}_y^{(n)}\left(z\right) + in\kappa_z\tilde{\mathrm{E}}_y^{(n)}\left(z\right) - ik_y^{(0)}\tilde{\mathrm{E}}_z^{(n)}\left(z\right) = -ik_0\eta_0\tilde{\mathrm{H}}_x^{(n)}\left(z\right), \quad (2.23)$$

$$k_y^{(0)}\tilde{\mathrm{E}}_x^{(n)}\left(z\right) - k_x^{(n)}\tilde{\mathrm{E}}_y^{(n)}\left(z\right) = -\,k_0\eta_0\tilde{\mathrm{H}}_z^{(n)}\left(z\right), \quad (2.24)$$

$$\begin{aligned}\frac{\mathrm{d}}{\mathrm{d}z}\tilde{\mathrm{H}}_x^{(n)}\left(z\right) + in\kappa_z\tilde{\mathrm{H}}_x^{(n)}\left(z\right) - ik_x^{(n)}\tilde{\mathrm{H}}_z^{(n)}\left(z\right) &= -\frac{ik_0}{\eta_0}\sum_{n'\in\mathbb{Z}}\Big[\tilde{\epsilon}_{yx}^{(n-n')}\tilde{\mathrm{E}}_x^{(n')}\left(z\right)\\ &\quad + \tilde{\epsilon}_{yy}^{(n-n')}\tilde{\mathrm{E}}_y^{(n')}\left(z\right) + \tilde{\epsilon}_{yz}^{(n-n')}\tilde{\mathrm{E}}_z^{(n')}\left(z\right)\Big], \quad (2.25)\\ \frac{\mathrm{d}}{\mathrm{d}z}\tilde{\mathrm{H}}_y^{(n)}\left(z\right) + in\kappa_z\tilde{\mathrm{H}}_y^{(n)}\left(z\right) - ik_y^{(0)}\tilde{\mathrm{H}}_z^{(n)}\left(z\right) &= \frac{ik_0}{\eta_0}\sum_{n'\in\mathbb{Z}}\Big[\tilde{\epsilon}_{xx}^{(n-n')}\tilde{\mathrm{E}}_x^{(n')}\left(z\right)\\ &\quad + \tilde{\epsilon}_{xy}^{(n-n')}\tilde{\mathrm{E}}_y^{(n')}\left(z\right) + \tilde{\epsilon}_{xz}^{(n-n')}\tilde{\mathrm{E}}_z^{(n')}\left(z\right)\Big], \quad (2.26)\\ k_y^{(0)}\,\tilde{\mathrm{H}}_x^{(n)}\left(z\right) - k_x^{(n)}\,\tilde{\mathrm{H}}_y^{(n)}\left(z\right) &= \frac{k_0}{\eta_0}\sum_{n'\in\mathbb{Z}}\Big[\tilde{\epsilon}_{zx}^{(n-n')}\tilde{\mathrm{E}}_x^{(n')}\left(z\right)\\ &\quad + \tilde{\epsilon}_{zy}^{(n-n')}\tilde{\mathrm{E}}_y^{(n')}\left(z\right) + \tilde{\epsilon}_{zz}^{(n-n')}\tilde{\mathrm{E}}_z^{(n')}\left(z\right)\Big] \quad (2.27)\end{aligned}$$

are derived for $z \in (0, d)$.

Equations (2.22)–(2.27) hold for all $n \in \mathbb{Z}$, and are thus an infinite system of first–order ODEs. For numerical solution, the restriction $|n| \leq \mathrm{N}_t$ is made, and then four $(2\mathrm{N}_t + 1)$–column vectors

$$\left.\begin{array}{ll} \left[\underline{\tilde{\mathrm{E}}}_\sigma(z)\right] = \left[\tilde{\mathrm{E}}_\sigma^{(n)}(z)\right] , & \left[\underline{\mathrm{E}}_\sigma(z)\right] = \left[\mathrm{E}_\sigma^{(n)}(z)\right] \\ \left[\underline{\tilde{\mathrm{H}}}_\sigma(z)\right] = \left[\tilde{\mathrm{H}}_\sigma^{(n)}(z)\right] , & \left[\underline{\mathrm{H}}_\sigma(z)\right] = \left[\mathrm{H}_\sigma^{(n)}(z)\right] \end{array}\right\} , \quad \sigma = x, y, z;\ n \in [-\mathrm{N}_t, \mathrm{N}_t] \tag{2.28}$$

are defined. Likewise, the diagonal $(2\mathrm{N}_t + 1) \times (2\mathrm{N}_t + 1)$ matrixes

$$\left.\begin{array}{l} \left[\underline{\underline{\mathrm{K}}}_x\right] = \mathrm{Diag}\left[k_x^{(n)}\right]_{[-\mathrm{N}_t, \mathrm{N}_t]} \\ \left[\underline{\underline{\kappa}}_z\right] = \kappa_z \mathrm{Diag}\left[n\right]_{[-\mathrm{N}_t, \mathrm{N}_t]} \end{array}\right\} \tag{2.29}$$

are defined; and so are the Toeplitz matrixes

$$\left[\underline{\underline{\epsilon}}_{\sigma\sigma'}\right] = \left[\epsilon_{\sigma\sigma'}^{(n-n')}\right] , \quad \sigma = x, y, z;\ n, n' \in [-\mathrm{N}_t, \mathrm{N}_t] . \tag{2.30}$$

Here, $\mathrm{Diag}[\wp(n)]_{[m,m']}$ denotes the diagonal matrix with the diagonal entries $\wp(n)$ for $n \in [m, m']$, with m and m' being integers.

After substituting (2.24) and (2.27) into (2.22), (2.23), (2.25) and (2.26), in order to eliminate the normal electromagnetic field components (i.e., $\tilde{\mathrm{E}}_z^{(n)}$ and $\tilde{\mathrm{H}}_z^{(n)}$), and performing some algebraic manipulations, the first–order matrix ODE

$$\frac{\mathrm{d}}{\mathrm{d}z}\left[\underline{\tilde{\mathbf{f}}}(z)\right] = i\left[\underline{\underline{\tilde{\mathbf{P}}}}\right]\left[\underline{\tilde{\mathbf{f}}}(z)\right] , \quad 0 < z < d \tag{2.31}$$

is derived. The column vector

$$\left[\underline{\tilde{\mathbf{f}}}(z)\right] = \left[\ \left[\underline{\tilde{\mathrm{E}}}_x(z)\right]^{\mathrm{T}},\ \left[\underline{\tilde{\mathrm{E}}}_y(z)\right]^{\mathrm{T}},\ \eta_0\left[\underline{\tilde{\mathrm{H}}}_x(z)\right]^{\mathrm{T}},\ \eta_0\left[\underline{\tilde{\mathrm{H}}}_y(z)\right]^{\mathrm{T}}\ \right]^{\mathrm{T}} \tag{2.32}$$

contains $4(2\mathrm{N}_t + 1)$ components, and the constant–valued matrix $\left[\underline{\underline{\tilde{\mathbf{P}}}}\right]$ has the form

$$\left[\underline{\underline{\tilde{\mathbf{P}}}}\right] = \left[\begin{array}{cccc} \left[\underline{\underline{\tilde{\mathrm{P}}}}_{11}\right] & \left[\underline{\underline{\tilde{\mathrm{P}}}}_{12}\right] & \left[\underline{\underline{\tilde{\mathrm{P}}}}_{13}\right] & \left[\underline{\underline{\tilde{\mathrm{P}}}}_{14}\right] \\ \left[\underline{\underline{\tilde{\mathrm{P}}}}_{21}\right] & \left[\underline{\underline{\tilde{\mathrm{P}}}}_{22}\right] & \left[\underline{\underline{\tilde{\mathrm{P}}}}_{23}\right] & \left[\underline{\underline{\tilde{\mathrm{P}}}}_{24}\right] \\ \left[\underline{\underline{\tilde{\mathrm{P}}}}_{31}\right] & \left[\underline{\underline{\tilde{\mathrm{P}}}}_{32}\right] & \left[\underline{\underline{\tilde{\mathrm{P}}}}_{33}\right] & \left[\underline{\underline{\tilde{\mathrm{P}}}}_{34}\right] \\ \left[\underline{\underline{\tilde{\mathrm{P}}}}_{41}\right] & \left[\underline{\underline{\tilde{\mathrm{P}}}}_{42}\right] & \left[\underline{\underline{\tilde{\mathrm{P}}}}_{43}\right] & \left[\underline{\underline{\tilde{\mathrm{P}}}}_{44}\right] \end{array}\right] , \tag{2.33}$$

wherein the sixteen $(2\mathrm{N}_t+1)\times(2\mathrm{N}_t+1)$ submatrixes are defined as follows:

$$\begin{aligned}
\left[\underline{\underline{\tilde{\mathrm{P}}}}_{11}\right] &= -\left[\underline{\underline{\kappa}}_z\right] - \left[\underline{\underline{\mathrm{K}}}_x\right]\left[\underline{\underline{\epsilon}}_{zz}\right]^{-1}\left[\underline{\underline{\epsilon}}_{zx}\right] , \\
\left[\underline{\underline{\tilde{\mathrm{P}}}}_{12}\right] &= -\left[\underline{\underline{\mathrm{K}}}_x\right]\left[\underline{\underline{\epsilon}}_{zz}\right]^{-1}\left[\underline{\underline{\epsilon}}_{zy}\right] , \\
\left[\underline{\underline{\tilde{\mathrm{P}}}}_{13}\right] &= \tfrac{k_y^{(0)}}{k_0}\left[\underline{\underline{\mathrm{K}}}_x\right]\left[\underline{\underline{\epsilon}}_{zz}\right]^{-1} , \\
\left[\underline{\underline{\tilde{\mathrm{P}}}}_{14}\right] &= k_0\left[\underline{\underline{\mathrm{I}}}\right]_{2\mathrm{N}_t+1} - \tfrac{1}{k_0}\left[\underline{\underline{\mathrm{K}}}_x\right]\left[\underline{\underline{\epsilon}}_{zz}\right]^{-1}\left[\underline{\underline{\mathrm{K}}}_x\right] ,
\end{aligned} \tag{2.34}$$

$$\begin{aligned}
\left[\underline{\underline{\tilde{\mathrm{P}}}}_{21}\right] &= -k_y^{(0)}\left[\underline{\underline{\epsilon}}_{zz}\right]^{-1}\left[\underline{\underline{\epsilon}}_{zx}\right] , \\
\left[\underline{\underline{\tilde{\mathrm{P}}}}_{22}\right] &= -\left[\underline{\underline{\kappa}}_z\right] - k_y^{(0)}\left[\underline{\underline{\epsilon}}_{zz}\right]^{-1}\left[\underline{\underline{\epsilon}}_{zy}\right] , \\
\left[\underline{\underline{\tilde{\mathrm{P}}}}_{23}\right] &= -k_0\left[\underline{\underline{\mathrm{I}}}\right]_{2\mathrm{N}_t+1} + \tfrac{\left(k_y^{(0)}\right)^2}{k_0}\left[\underline{\underline{\epsilon}}_{zz}\right]^{-1} , \\
\left[\underline{\underline{\tilde{\mathrm{P}}}}_{24}\right] &= -\tfrac{k_y^{(0)}}{k_0}\left[\underline{\underline{\epsilon}}_{zz}\right]^{-1}\left[\underline{\underline{\mathrm{K}}}_x\right] ,
\end{aligned} \tag{2.35}$$

$$\begin{aligned}
\left[\underline{\underline{\tilde{\mathrm{P}}}}_{31}\right] &= -\tfrac{k_y^{(0)}}{k_0}\left[\underline{\underline{\mathrm{K}}}_x\right] + k_0\left(\left[\underline{\underline{\epsilon}}_{yz}\right]\left[\underline{\underline{\epsilon}}_{zz}\right]^{-1}\left[\underline{\underline{\epsilon}}_{zx}\right] - \left[\underline{\underline{\epsilon}}_{yx}\right]\right) , \\
\left[\underline{\underline{\tilde{\mathrm{P}}}}_{32}\right] &= \tfrac{1}{k_0}\left[\underline{\underline{\mathrm{K}}}_x\right]\left[\underline{\underline{\mathrm{K}}}_x\right] + k_0\left(\left[\underline{\underline{\epsilon}}_{yz}\right]\left[\underline{\underline{\epsilon}}_{zz}\right]^{-1}\left[\underline{\underline{\epsilon}}_{zy}\right] - \left[\underline{\underline{\epsilon}}_{yy}\right]\right) , \\
\left[\underline{\underline{\tilde{\mathrm{P}}}}_{33}\right] &= -\left[\underline{\underline{\kappa}}_z\right] - k_y^{(0)}\left[\underline{\underline{\epsilon}}_{yz}\right]\left[\underline{\underline{\epsilon}}_{zz}\right]^{-1} , \\
\left[\underline{\underline{\tilde{\mathrm{P}}}}_{34}\right] &= \left[\underline{\underline{\epsilon}}_{yz}\right]\left[\underline{\underline{\epsilon}}_{zz}\right]^{-1}\left[\underline{\underline{\mathrm{K}}}_x\right] ,
\end{aligned} \tag{2.36}$$

$$\begin{aligned}
\left[\underline{\underline{\tilde{\mathrm{P}}}}_{41}\right] &= -\tfrac{\left(k_y^{(0)}\right)^2}{k_0}\left[\underline{\underline{\mathrm{I}}}\right]_{2\mathrm{N}_t+1} - k_0\left(\left[\underline{\underline{\epsilon}}_{xz}\right]\left[\underline{\underline{\epsilon}}_{zz}\right]^{-1}\left[\underline{\underline{\epsilon}}_{zx}\right] - \left[\underline{\underline{\epsilon}}_{xx}\right]\right) , \\
\left[\underline{\underline{\tilde{\mathrm{P}}}}_{42}\right] &= \tfrac{k_y^{(0)}}{k_0}\left[\underline{\underline{\mathrm{K}}}_x\right] - k_0\left(\left[\underline{\underline{\epsilon}}_{xz}\right]\left[\underline{\underline{\epsilon}}_{zz}\right]^{-1}\left[\underline{\underline{\epsilon}}_{zy}\right] - \left[\underline{\underline{\epsilon}}_{xy}\right]\right) , \\
\left[\underline{\underline{\tilde{\mathrm{P}}}}_{43}\right] &= k_y^{(0)}\left[\underline{\underline{\epsilon}}_{xz}\right]\left[\underline{\underline{\epsilon}}_{zz}\right]^{-1} , \\
\left[\underline{\underline{\tilde{\mathrm{P}}}}_{44}\right] &= -\left[\underline{\underline{\kappa}}_z\right] - \left[\underline{\underline{\epsilon}}_{xz}\right]\left[\underline{\underline{\epsilon}}_{zz}\right]^{-1}\left[\underline{\underline{\mathrm{K}}}_x\right] .
\end{aligned} \tag{2.37}$$

Here, $\left[\underline{\underline{\mathrm{I}}}\right]_m$ denotes the $m\times m$ identity matrix.

2.1.3 Solution of Boundary Value Problem

The matrix ODE (2.31) has the solution [67]

$$\left[\tilde{\underline{\mathbf{f}}}(z_2)\right] = \left[\tilde{\underline{\underline{\mathrm{G}}}}\right] \exp\left\{i(z_2 - z_1)\left[\tilde{\underline{\underline{\mathrm{D}}}}\right]\right\}\left[\tilde{\underline{\underline{\mathrm{G}}}}\right]^{-1}\left[\tilde{\underline{\mathbf{f}}}(z_1)\right] , \tag{2.38}$$

where the columns of the square matrix $\left[\tilde{\underline{\underline{\mathrm{G}}}}\right]$ are the successive eigenvectors of $\left[\tilde{\underline{\underline{\mathbf{P}}}}\right]$, and the diagonal matrix $\left[\tilde{\underline{\underline{\mathrm{D}}}}\right]$ contains the corresponding eigenvalues of $\left[\tilde{\underline{\underline{\mathbf{P}}}}\right]$. The assumption here is that $\left[\tilde{\underline{\underline{\mathbf{P}}}}\right]$ is diagonalizable, i.e., it has $4(2\mathrm{N}_t + 1)$ linearly independent eigenvectors [68].

In order to solve the boundary value problem for determining $\left\{r_{\mathrm{L}}^{(n)},\, r_{\mathrm{R}}^{(n)}\right\}$ and $\left\{t_{\mathrm{L}}^{(n)},\, t_{\mathrm{R}}^{(n)}\right\}$, it is necessary to determine the column vector

$$[\underline{\mathbf{f}}\,(z)] = \left[\, [\underline{\mathrm{E}}_x\,(z)]^{\mathrm{T}},\ \left[\underline{\mathrm{E}}_y\,(z)\right]^{\mathrm{T}},\ \eta_0\,[\underline{\mathrm{H}}_x\,(z)]^{\mathrm{T}},\ \eta_0\left[\underline{\mathrm{H}}_y\,(z)\right]^{\mathrm{T}}\,\right]^{\mathrm{T}} \tag{2.39}$$

instead of $\left[\tilde{\underline{\mathbf{f}}}(z)\right]$. The two column vectors are simply related to each other as

$$[\underline{\mathbf{f}}\,(z)] = \left[\underline{\underline{c}}(z)\right]\left[\tilde{\underline{\mathbf{f}}}(z)\right] , \tag{2.40}$$

where the diagonal matrix

$$\left[\underline{\underline{c}}(z)\right] = \mathrm{Diag}\left[\exp\left(in_{\mathrm{M}}\kappa_z z\right)\right] ; \tag{2.41}$$

$n_{\mathrm{M}} = \mathrm{Mod}[n-1,\, 2\mathrm{N}_t+1] - \mathrm{N}_t$; and $\mathrm{Mod}[m, m']$ denotes the remainder when m is divided by m'.

Equations (2.38) and (2.40) yield the relation

$$[\underline{\mathbf{f}}(z_2)] = \left[\underline{\underline{\mathrm{G}}}(z_2)\right]\exp\left\{i(z_2 - z_1)\left[\tilde{\underline{\underline{\mathrm{D}}}}\right]\right\}\left[\underline{\underline{\mathrm{G}}}(z_1)\right]^{-1}[\underline{\mathbf{f}}(z_1)] , \tag{2.42}$$

where the matrix

$$\left[\underline{\underline{\mathrm{G}}}(z)\right] = \left[\underline{\underline{c}}(z)\right]\left[\tilde{\underline{\underline{\mathrm{G}}}}\right] \tag{2.43}$$

is a periodic function of z; hence,

$$[\underline{\mathbf{f}}(d)] = \left[\underline{\underline{\mathrm{G}}}(d)\right]\exp\left\{id\left[\tilde{\underline{\underline{\mathrm{D}}}}\right]\right\}\left[\underline{\underline{\mathrm{G}}}(0)\right]^{-1}[\underline{\mathbf{f}}(0)] . \tag{2.44}$$

The continuity of the tangential components of the electric and magnetic field phasors across the two boundaries $z = 0$ and $z = d$ must be enforced with respect to the Floquet harmonic of any order n. From (2.6)–(2.11), the boundary values

$$[\underline{\mathbf{f}}\,(0)] = \begin{bmatrix} \left[\underline{\underline{\mathrm{Y}}}_e^+\right] & \left[\underline{\underline{\mathrm{Y}}}_e^-\right] \\ \left[\underline{\underline{\mathrm{Y}}}_h^+\right] & \left[\underline{\underline{\mathrm{Y}}}_h^-\right] \end{bmatrix} \begin{bmatrix} [\underline{\mathrm{A}}] \\ [\underline{\mathrm{R}}] \end{bmatrix}, \quad [\underline{\mathbf{f}}\,(d)] = \begin{bmatrix} \left[\underline{\underline{\mathrm{Y}}}_e^+\right] & \left[\underline{\underline{0}}\right]_{4\mathrm{N}_t+2} \\ \left[\underline{\underline{\mathrm{Y}}}_h^+\right] & \left[\underline{\underline{0}}\right]_{4\mathrm{N}_t+2} \end{bmatrix} \begin{bmatrix} [\underline{\mathrm{T}}] \\ [\underline{0}]_{4\mathrm{N}_t+2} \end{bmatrix} \tag{2.45}$$

are available. Here, $[\underline{0}]_m$ is the m–column null vector; while $\left[\underline{\underline{0}}\right]_m$ is the $m \times m$ null matrix. The column vectors

$$[\underline{\mathrm{A}}] = \begin{bmatrix} a_{\mathrm{L}}^{(n)} \\ a_{\mathrm{R}}^{(n)} \end{bmatrix}, \quad [\underline{\mathrm{R}}] = \begin{bmatrix} r_{\mathrm{L}}^{(n)} \\ r_{\mathrm{R}}^{(n)} \end{bmatrix}, \quad [\underline{\mathrm{T}}] = \begin{bmatrix} t_{\mathrm{L}}^{(n)} \\ t_{\mathrm{R}}^{(n)} \end{bmatrix} \tag{2.46}$$

in (2.45) are of size $4\mathrm{N}_t+2$. The square matrixes $\left[\underline{\underline{\mathrm{Y}}}_e^{\pm}\right]$ and $\left[\underline{\underline{\mathrm{Y}}}_h^{\pm}\right]$ of size $(4\mathrm{N}_t+2)\times(4\mathrm{N}_t+2)$ are quite sparse; and their nonzero entries are calculated as follows:

$$\left.\begin{aligned} \left[\underline{\underline{\mathrm{Y}}}_e^{\pm}\right]_{nn'} &= (-i/n_{hs})\left[\underline{\underline{\mathrm{Y}}}_h^{\pm}\right]_{nn'} = \mathbf{L}_{\pm}^{(n)} \cdot \mathbf{u}_x\,, && \text{if } n = n' \in [1,\ (2\mathrm{N}_t+1)] \\ \left[\underline{\underline{\mathrm{Y}}}_e^{\pm}\right]_{nn'} &= (-i/n_{hs})\left[\underline{\underline{\mathrm{Y}}}_h^{\pm}\right]_{nn'} = \mathbf{L}_{\pm}^{(n)} \cdot \mathbf{u}_y\,, && \text{if } n = n' + 2\mathrm{N}_t + 1 \\ \left[\underline{\underline{\mathrm{Y}}}_e^{\pm}\right]_{nn'} &= (i/n_{hs})\left[\underline{\underline{\mathrm{Y}}}_h^{\pm}\right]_{nn'} = \mathbf{R}_{\pm}^{(n)} \cdot \mathbf{u}_x\,, && \text{if } n = n' - 2\mathrm{N}_t - 1 \\ \left[\underline{\underline{\mathrm{Y}}}_e^{\pm}\right]_{nn'} &= (i/n_{hs})\left[\underline{\underline{\mathrm{Y}}}_h^{\pm}\right]_{nn'} = \mathbf{R}_{\pm}^{(n)} \cdot \mathbf{u}_y\,, && \text{if } n = n' \in [(2\mathrm{N}_t+2),\ (4\mathrm{N}_t+2)] \end{aligned}\right\}. \tag{2.47}$$

Finally, the substitution of (2.45) into (2.44) yields

$$\begin{bmatrix} \left[\underline{\underline{\mathrm{U}}}_{\mathrm{T}}\right] \\ \left[\underline{\underline{\mathrm{V}}}_{\mathrm{T}}\right] \end{bmatrix} [\underline{\mathrm{T}}] + \begin{bmatrix} e^{id\left[\underline{\underline{\tilde{\mathrm{D}}}}_u\right]} & \left[\underline{\underline{0}}\right]_{4\mathrm{N}_t+2} \\ \left[\underline{\underline{0}}\right]_{4\mathrm{N}_t+2} & e^{id\left[\underline{\underline{\tilde{\mathrm{D}}}}_l\right]} \end{bmatrix} \begin{bmatrix} \left[\underline{\underline{\mathrm{U}}}_{\mathrm{R}}\right] \\ \left[\underline{\underline{\mathrm{V}}}_{\mathrm{R}}\right] \end{bmatrix} [\underline{\mathrm{R}}] = \begin{bmatrix} e^{id\left[\underline{\underline{\tilde{\mathrm{D}}}}_u\right]} & \left[\underline{\underline{0}}\right]_{4\mathrm{N}_t+2} \\ \left[\underline{\underline{0}}\right]_{4\mathrm{N}_t+2} & e^{id\left[\underline{\underline{\tilde{\mathrm{D}}}}_l\right]} \end{bmatrix} \begin{bmatrix} \left[\underline{\underline{\mathrm{U}}}_{\mathrm{A}}\right] \\ \left[\underline{\underline{\mathrm{V}}}_{\mathrm{A}}\right] \end{bmatrix} [\underline{\mathrm{A}}]\,, \tag{2.48}$$

where $\left[\underline{\underline{\tilde{\mathrm{D}}}}_u\right]$ and $\left[\underline{\underline{\tilde{\mathrm{D}}}}_l\right]$ are the upper and lower diagonal submatrixes of $\left[\underline{\underline{\tilde{\mathrm{D}}}}\right]$, respectively,

and the following three rectangular matrixes assist in notational brevity:

$$\begin{bmatrix} \left[\underline{\underline{\mathrm{U}}}_{\mathrm{T}}\right] \\ \left[\underline{\underline{\mathrm{V}}}_{\mathrm{T}}\right] \end{bmatrix} = \left[\underline{\underline{\mathrm{G}}}(d)\right]^{-1} \begin{bmatrix} \left[\underline{\underline{\mathrm{Y}}}_{e}^{+}\right] \\ \left[\underline{\underline{\mathrm{Y}}}_{h}^{+}\right] \end{bmatrix}, \tag{2.49}$$

$$\begin{bmatrix} \left[\underline{\underline{\mathrm{U}}}_{\mathrm{R}}\right] \\ \left[\underline{\underline{\mathrm{V}}}_{\mathrm{R}}\right] \end{bmatrix} = -\left[\underline{\underline{\mathrm{G}}}(0)\right]^{-1} \begin{bmatrix} \left[\underline{\underline{\mathrm{Y}}}_{e}^{-}\right] \\ \left[\underline{\underline{\mathrm{Y}}}_{h}^{-}\right] \end{bmatrix}, \tag{2.50}$$

$$\begin{bmatrix} \left[\underline{\underline{\mathrm{U}}}_{\mathrm{A}}\right] \\ \left[\underline{\underline{\mathrm{V}}}_{\mathrm{A}}\right] \end{bmatrix} = \left[\underline{\underline{\mathrm{G}}}(0)\right]^{-1} \begin{bmatrix} \left[\underline{\underline{\mathrm{Y}}}_{e}^{+}\right] \\ \left[\underline{\underline{\mathrm{Y}}}_{h}^{+}\right] \end{bmatrix}. \tag{2.51}$$

For calculating the unknown $[\underline{\mathrm{R}}]$ and $[\underline{\mathrm{T}}]$, the so–called R–matrix propagating algorithm [66, 69] — which is based on the rearrangement of the positions of the eigenvalues of $\left[\underline{\underline{\tilde{\mathbf{P}}}}\right]$ in the diagonal matrix $\left[\underline{\underline{\tilde{\mathrm{D}}}}\right]$ — helps in avoiding numerical instabilities, especially when N_t is large [70, 71]. Therefore, the entries on the diagonal of $\left[\underline{\underline{\tilde{\mathrm{D}}}}\right]$ (thus $\left[\underline{\underline{\tilde{\mathrm{D}}}}_{u}\right]$ and $\left[\underline{\underline{\tilde{\mathrm{D}}}}_{l}\right]$ also) are rearranged in the order of increasing magnitude of the imaginary part, and the columns of $\left[\underline{\underline{\tilde{\mathrm{G}}}}\right]$ are rearranged accordingly. The final algebraic equation

$$\begin{bmatrix} e^{-id\left[\underline{\underline{\tilde{\mathrm{D}}}}_{u}\right]} \left[\underline{\underline{\mathrm{U}}}_{\mathrm{T}}\right] & \left[\underline{\underline{\mathrm{U}}}_{\mathrm{R}}\right] \\ \left[\underline{\underline{\mathrm{V}}}_{\mathrm{T}}\right] & e^{id\left[\underline{\underline{\tilde{\mathrm{D}}}}_{l}\right]} \left[\underline{\underline{\mathrm{V}}}_{\mathrm{R}}\right] \end{bmatrix} \begin{bmatrix} [\underline{\mathrm{T}}] \\ [\underline{\mathrm{R}}] \end{bmatrix} = \begin{bmatrix} \left[\underline{\underline{\mathrm{U}}}_{\mathrm{A}}\right] \\ e^{id\left[\underline{\underline{\tilde{\mathrm{D}}}}_{l}\right]} \left[\underline{\underline{\mathrm{V}}}_{\mathrm{A}}\right] \end{bmatrix} [\underline{\mathrm{A}}], \tag{2.52}$$

yielded by (2.48) for the determination of $[\underline{\mathrm{R}}]$ and $[\underline{\mathrm{T}}]$ is algorithmically stable due to the fact that the exponential terms $e^{-id\left[\underline{\underline{\tilde{\mathrm{D}}}}_{u}\right]}$ and $e^{id\left[\underline{\underline{\tilde{\mathrm{D}}}}_{l}\right]}$ never become overwhelming in magnitude because of the rearrangement of the eigenvalues. The matrix inverse operation required to solve (2.52) for $[\underline{\mathrm{R}}]$ and $[\underline{\mathrm{T}}]$ is then easily accomplished for arbitrary d and N_{t}.

Thus, the RCWA has been used to devise a robust numerical solution procedure for planewave diffraction by slanted chiral STFs: Calculation of the planewave response is reduced to the solution of the algebraic equation (2.52) for $[\underline{\mathrm{R}}]$ and $[\underline{\mathrm{T}}]$. In Chapters 3 and 4, the results obtained after implementing the devised procedure are presented.

Chapter 3

Response of Slanted Chiral STFs to Normally Incident Plane Waves[‡]

The response of a dielectric slanted chiral STF to an incident plane wave is expressed through the column vectors [R] and [T], which can be determined by following the procedure devised in Chapter 2. Several quantities of significance such as reflectances and transmittances for Floquet harmonics of different orders can then be calculated. The objective of this chapter is to identify the characteristics of the response of slanted chiral STFs to normally incident plane waves (i.e., $k_x^{(0)} = k_y^{(0)} = 0$), with a focus on the circular Bragg phenomenon.

[‡] This chapter is partly adapted from the following paper: F. Wang, A. Lakhtakia, R. Messier, "Coupling of Raleigh–Wood anomalies with the circular Bragg phenomenon in the slanted sculptured thin films", Eur. Phys. J. Appl. Phys. **20** 91–103 (2002); corrections: **24** 91 (2003).

3.1 Preliminaries

Once the column vectors [$\underline{\mathrm{R}}$] and [$\underline{\mathrm{T}}$] have been determined using the RCWA described in Chapter 2, the reflection and transmission coefficients

$$r^{(n)}_{\sigma\sigma'} = \frac{r^{(n)}_{\sigma}}{a^{(0)}_{\sigma'}}\,, \quad t^{(n)}_{\sigma\sigma'} = \frac{t^{(n)}_{\sigma}}{a^{(0)}_{\sigma'}}\,, \quad \sigma,\sigma' = \mathrm{L},\mathrm{R} \tag{3.1}$$

can be computed as functions of the incidence wavevector $\mathbf{k}^{(0)}_{+}$. Reflectances ($\mathrm{R}^{(n)}_{\mathrm{LL}}$, etc.) and transmittances ($\mathrm{T}^{(n)}_{\mathrm{LL}}$, etc.) of order n are thereby defined as

$$\mathrm{R}^{(n)}_{\sigma\sigma'} = \frac{\mathrm{Re}[k^{(n)}_z]}{\mathrm{Re}[k^{(0)}_z]}|r^{(n)}_{\sigma\sigma'}|^2\,, \quad \mathrm{T}^{(n)}_{\sigma\sigma'} = \frac{\mathrm{Re}[k^{(n)}_z]}{\mathrm{Re}[k^{(0)}_z]}|t^{(n)}_{\sigma\sigma'}|^2\,, \quad \sigma,\sigma' = \mathrm{L},\mathrm{R}\,, \tag{3.2}$$

where Re[ ] stands for the real part. Coefficients and remittances with both subscripts identical are co–polarized, and those with two different subscripts are cross–polarized. Co–polarized coefficients and remittances subscripted RR (LL) are labeled as co–handed, and those subscripted LL (RR) are labeled as cross–handed, when the chiral STF is structurally right(left)–handed.

The principle of conservation of energy mandates the inequalities

$$\sum_{n\in[-\mathrm{N}_t,\mathrm{N}_t]} \left(\mathrm{R}^{(n)}_{\mathrm{LL}} + \mathrm{R}^{(n)}_{\mathrm{RL}} + \mathrm{T}^{(n)}_{\mathrm{LL}} + \mathrm{T}^{(n)}_{\mathrm{RL}}\right) \leq 1\,, \tag{3.3}$$

$$\sum_{n\in[-\mathrm{N}_t,\mathrm{N}_t]} \left(\mathrm{R}^{(n)}_{\mathrm{LR}} + \mathrm{R}^{(n)}_{\mathrm{RR}} + \mathrm{T}^{(n)}_{\mathrm{LR}} + \mathrm{T}^{(n)}_{\mathrm{RR}}\right) \leq 1\,. \tag{3.4}$$

The inequalities reduce to equalities for non–dissipative slanted chiral STFs.

Care must be taken for the special case $\alpha = 0$. All nonspecular coefficients then fold into the specular ones, i.e.,

$$r^{(0)}_{\sigma\sigma'} \Leftarrow \sum_{|n|\leq \mathrm{N}_t} r^{(n)}_{\sigma\sigma'}\,, \quad t^{(0)}_{\sigma\sigma'} \Leftarrow \sum_{|n|\leq \mathrm{N}_t} t^{(n)}_{\sigma\sigma'}\,, \quad \sigma,\sigma' = \mathrm{L},\mathrm{R}\,, \tag{3.5}$$

because $\Lambda_x \to \infty$. Similarly, the remittances for $\alpha = 0$ can only be specular; hence,

$$\mathrm{R}^{(0)}_{\sigma\sigma'} = |r^{(0)}_{\sigma\sigma'}|^2\,, \quad \mathrm{T}^{(0)}_{\sigma\sigma'} = |t^{(0)}_{\sigma\sigma'}|^2\,, \quad \sigma,\sigma' = \mathrm{L},\mathrm{R}\,. \tag{3.6}$$

The numerical solution procedure of Chapter 2 was implemented using double–precision arithmetic in Fortran 90 on a Solaris computer. A structurally right–handed slanted chiral STF was chosen for the results presented here; thus, $h = 1$. The constitutive scalars $\epsilon_{a,b,c}$ were determined by the single–resonance Lorentzian model (2.4) with the following parameters: $p_a = 2.0$, $p_b = 2.6$, $p_c = 2.1$, $\mathrm{N}_a = \mathrm{N}_b = \mathrm{N}_c = 100$, $\lambda_a = \lambda_c = 140$ nm, and $\lambda_b = 150$ nm. Here, $\lambda_{a,b,c} = 2\pi/\omega_{a,b,c}\sqrt{\mu_0\epsilon_0}$ are resonance wavelengths. Structural parameters were specified as $\Omega = 300$ nm, $d = 27\Omega$, and $\chi_s = 30^\circ$. The slant angle $\alpha \in (-\chi_s, \chi_s)$ was kept as a variable. The chosen slanted chiral STF is potentially realizable using silicon dioxide, and is thus likely to be compatible with semiconductor technology.

Let the wavevector $\mathbf{k}_+^{(0)}$ make the angles (i) $\theta_{\mathrm{i}}^p \in (-90^\circ, 90^\circ)$ to the z axis and (ii) $\psi_{\mathrm{i}}^p \in [0, 180^\circ)$ to the x axis in the xy plane[‡]. Only the normal–incidence case is examined in this chapter; hence, $\theta_{\mathrm{i}}^p = \psi_{\mathrm{i}}^p = 0$.

From numerous computational tests, it was confirmed that every reflectance and transmittance greater than 0.001 converged to 1% accuracy for the wavelength–regime $\lambda_0 \in$ [900, 1200] nm focused on, when $\mathrm{N}_t = 20$ and $n_{hs} = 1$ were chosen. All propagating harmonics and some evanescent harmonics were thereby covered. Moreover, the left sides of both (3.3) and (3.4) converged to have neither condition violated by more than 1 ppm.

[‡]An exception to the specification of the domain of ψ_i^p is that $\psi_i^p \in [-180^\circ, 180^\circ)$ when θ_i^p is fixed to illustrate the effect of ψ_i^p. Analogously, this regulation applies to the specification of the domains of θ_i^b and ψ_i^b in Chapter 7 for beam incidence.

3.2 Circular Bragg Phenomenon

3.2.1 Chiral STFs

To begin with, chiral STFs ($\alpha = 0$) must be examined. The response of this film to normally incident plane waves has been extensively studied, theoretically [9] as well as experimentally [5, 33, 72].

The hallmark of an axially excited chiral STF is the circular Bragg phenomenon: Provided the ratio $\mathrm{N}_d = d/\Omega$ is sufficiently large and λ_0 lies within the Bragg regime, the reflectance is much higher if the handedness of the incident circularly polarized plane wave matches the structural handedness of the film than if otherwise. The center–wavelength of the Bragg regime is estimated as [9]

$$\lambda_0^{\mathrm{Br}} = \Omega \left[\sqrt{\epsilon_c \left(\lambda_0^{\mathrm{Br}} \right)} + \sqrt{\epsilon_d \left(\lambda_0^{\mathrm{Br}} \right)} \right] . \tag{3.7}$$

Coupled–wave theory provides an explanation for the polarization–sensitive Bragg phenomenon — a plane wave of matching handedness effectively encounters a Bragg grating, while that of the other handedness does not [30]–[32].

Figure 3.1 shows a comparison of the reflectances and transmittances computed using the numerical solution procedure of Chapter 2 against those computed using the analytical procedure available elsewhere [9]. All reflectances and transmittances must be specular when $\alpha = 0$, regardless of their order n, in view of (3.5) and (3.6). The Bragg regime — specified by $\lambda_0 \in (1050, 1150)$ nm — is obvious in the plots: $\mathrm{R}_{\mathrm{RR}}^{(0)} >> \mathrm{R}_{\mathrm{LL}}^{(0)}$ and $\mathrm{T}_{\mathrm{RR}}^{(0)} << \mathrm{T}_{\mathrm{LL}}^{(0)}$, while $\mathrm{R}_{\mathrm{RL}}^{(0)} \approx \mathrm{R}_{\mathrm{LR}}^{(0)}$ and $\mathrm{T}_{\mathrm{RL}}^{(0)} \approx \mathrm{T}_{\mathrm{LR}}^{(0)}$ are very small, especially around $\lambda_0^{\mathrm{Br}} = 1090$ nm as predicted by (3.7). The coincidence of the two sets of computed remittances is evident in Figure 3.1.

3.2.2 Slanted Chiral STF

Only for $\alpha \neq 0$ does a distinction between Floquet harmonics of order $n = 0$ and $n \neq 0$ appears, the former being classified as *specular* and the latter as *nonspecular* in the literature on diffraction gratings [44]. Non–negligible remittances were found to be only of orders $n = \mp 2$ and $n = 0$. The remittances of other orders turned out to be negligible (< 0.01) in the wavelength–regime $\lambda_0 \in [900, 1200]$ nm.

Figures 3.2 and 3.3 comprise spectral plots of the reflectances and the transmittances of order $n = 0$ and -2 as functions of λ_0 when $\alpha = 10^\circ$ and 15°, respectively. The characteristic signature of the circular Bragg phenomenon is found as a broad crest in the plot of $\mathrm{R}_{\mathrm{RR}}^{(-2)}$ and a trough in the plot of $\mathrm{T}_{\mathrm{RR}}^{(0)}$, positioned between the 1030–nm and 1120–nm wavelengths. Thus, a normally incident RCP plane wave is mostly reflected obliquely: at an angle $\sin^{-1}\left[(\lambda_0/\Omega)\sin\alpha\right]$ to the $+z$ axis. Since $\lambda_0/\Omega \sim 3.3$, even a slight increase in $|\alpha|$ results in more oblique reflection.

When the incident plane wave is LCP, however, $\mathrm{T}_{\mathrm{LL}}^{(0)}$ dominates all the other remittances in the same wavelength regime. Hence, the LCP plane wave is mostly transmitted without change of direction — in a fashion similar to that for $\alpha = 0$.

Clearly, the circular Bragg phenomenon is partly nonspecular for slanted chiral STFs, as indicated by a high co–handed reflectance of order $n = \mp 2$ for $\alpha \gtrless 0$ and a low co–handed specular transmittance in the Bragg regime. This characteristic of the circular Bragg phenomenon can be exploited for circular–polarization beamsplitters and direction couplers.

The center–wavelength of the Bragg regime shifts to smaller values with increasing $|\alpha|$. This blue–shift is captured by the modification of (3.7) to

$$\lambda_0^{\mathrm{Br}} = (\Omega\cos\alpha)\left[\sqrt{\epsilon_c\left(\lambda_0^{\mathrm{Br}}\right)} + \sqrt{\epsilon_d\left(\lambda_0^{\mathrm{Br}}\right)}\right] \tag{3.8}$$

for $|\alpha| << \chi_s$, as suggested by the values of λ_0^{Br} computed using the numerical solution

procedure of Chapter 2 for various $|\alpha|$. Figure 3.4(a) shows the comparison of the $|\alpha|$–dependence of λ_0^{Br} obtained using the RCWA procedure with (3.8), and the excellent correspondence for $|\alpha| \leq 15^\circ$ is illustrated. No surprisingly, this $|\alpha|$–dependence of λ_0^{Br} as predicted by (3.8) is in accord with the orange color of multi–domain cholesteric liquid crystals that were fabricated to reflect the red color [73].

Figure 3.4(b) contains a plot of the full–width–at–half–maximum (FWHM) bandwidth $\Delta\lambda_0^{\mathrm{Br}}$ as a function of $|\alpha|$. This plot clearly shows the thinning of the Bragg regime with increase in $|\alpha|$. Indeed, the circular Bragg phenomenon vanishes for $|\alpha| > 17.1^\circ$. The reason for the disappearance of that phenomenon is best explained *via* the so–called Rayleigh–Wood anomalies as follows.

Just as for the commonplace surface–relief gratings [44], nonspecular Floquet harmonics exist in the two half–spaces $z \leq 0$ and $z \geq d$. A Floquet harmonic of order n propagates energy away from the slanted chiral STF, provided $k_z^{(n)}$ is real–valued, i.e., for wavelengths $\lambda_0 < \lambda_{0_n}^{\mathrm{RW}}$, where the relation

$$\lambda_{0_n}^{\mathrm{RW}} = \frac{2n_{hs}\Omega}{|n|\,|\sin\alpha|} \tag{3.9}$$

follows from (2.16). The conversion of the Floquet harmonic of order n from propagating to evanescent, or *vice versa*, as λ_0 either increases or decreases across $\lambda_{0_n}^{\mathrm{RW}}$ is a Rayleigh–Wood anomaly.

Table 3.1 shows computed values of $\lambda_{0_n}^{\mathrm{RW}}$, ($n = \pm1, \pm2, \pm3$), for several different values of $|\alpha| \leq 17.1^\circ$. Specifically, as $|\alpha|$ increases from 0, $\lambda_{0_{\mp2}}^{\mathrm{RW}}$ decreases from "infinity" and begins to approach the center–wavelength λ_0^{Br} of the Bragg regime predicted by (3.8). Table 3.1 records the blue–shifts of both $\lambda_{0_{\mp2}}^{\mathrm{RW}}$ and λ_0^{Br} as $|\alpha|$ increases, but the decrease in $\lambda_{0_{\mp2}}^{\mathrm{RW}}$ is more rapid than the decrease in λ_0^{Br}.

When $|\alpha| = 15^\circ$, $\lambda_{0_{\mp2}}^{\mathrm{RW}}$ is about 100 nm larger than λ_0^{Br}. Still, the spectrums of $\mathrm{R}_{\mathrm{RR}}^{(\mp2)}$ and $\mathrm{T}_{\mathrm{RR}}^{(0)}$ are clearly affected, as implied by Figure 3.3 for $\alpha = 15^\circ$. The signature features of the circular Bragg phenomenon become irregular in Figure 3.3, in comparison to those

Table 3.1: Center–wavelength λ_0^{Br} of the Bragg regime and the wavelength $\lambda_{0_n}^{\mathrm{RW}}$ of the Rayleigh–Wood anomaly of order n for normal incidence. See Figure 3.1 for the various parameters used for the data presented in this table.

$\lvert\alpha\rvert$	0	10°	15°	16.7°	17.1°
λ_0^{Br} (nm)	1090	1073	1053	1044	1042
$\lambda_{0_{\mp1}}^{\mathrm{RW}}$ (nm)	$\star$	3456	2318	2088	2040
$\lambda_{0_{\mp2}}^{\mathrm{RW}}$ (nm)	$\star$	1728	1159	1044	1020
$\lambda_{0_{\mp3}}^{\mathrm{RW}}$ (nm)	$\star$	1152	773	696	680

$\star$ not applicable

in Figure 3.1 for $\alpha = 0$.

A further increase in $|\alpha|$ makes $\lambda_{0_{\mp2}}^{\mathrm{RW}}$ come even closer to λ_0^{Br} as predicted by (3.8). For example, the two wavelengths are equal in Table 3.1 when $|\alpha| = 16.7°$. The actual Bragg regime in Figure 3.5 for $\alpha = 16.7°$ is blue–shifted relative to the prediction from (3.8); the peak value of $\mathrm{R}_{\mathrm{RR}}^{(-2)}$ is noticeably smaller than that in Figures 3.1–3.3; and the Bragg regime is also narrower.

The circular Bragg phenomenon almost disappears when $|\alpha| = 17.1°$, with the peak value of $\mathrm{R}_{\mathrm{RR}}^{(\mp2)}$ (for $\alpha \gtrless 0$) dropping to one–half of its value for $\alpha = 0$. As $|\alpha|$ increases further, the rapid blue–shift of $\lambda_{0_{\mp2}}^{\mathrm{RW}}$ subverts the circular Bragg phenomenon considerably, leaving some minor peaks of nonspecular reflectances and transmittances.

3.3 Concluding Remarks

In conclusion,

- the partly nonspecular nature of the circular Bragg phenomenon, and

- the diminishment and even subversion of the circular Bragg phenomenon by the Rayleigh–Wood anomaly

are the two remarkable features of slanted chiral STFs in comparison to chiral STFs. Both have technological consequences which deserve exploration by experimentalists.

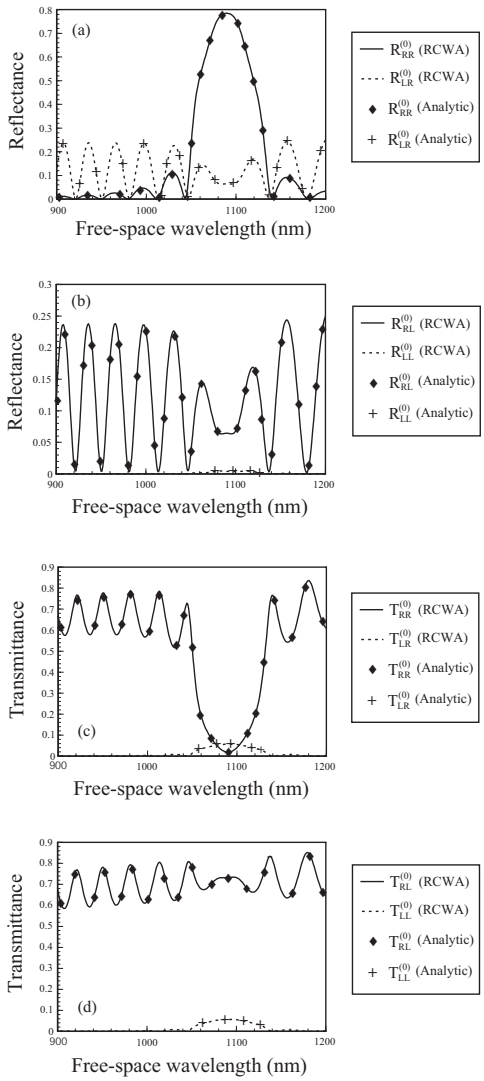

Figure 3.1: Reflectances and transmittances computed using the RCWA of Chapter 2 are compared against the results obtained from the analytical method available elsewhere [9]. The various parameters used are as follows: $p_a = 2.0$, $p_b = 2.6$, $p_c = 2.1$, $\mathrm{N}_a = \mathrm{N}_b = \mathrm{N}_c = 100$, $\lambda_a = \lambda_c = 140$ nm, $\lambda_b = 150$ nm, $\Omega = 300$ nm, $d = 27\Omega$, $\alpha = 0$, $\chi_s = 30°$, $h = 1$, $n_{hs} = 1$, and $\theta^p_{\mathrm{i}} = \psi^p_{\mathrm{i}} = 0$.

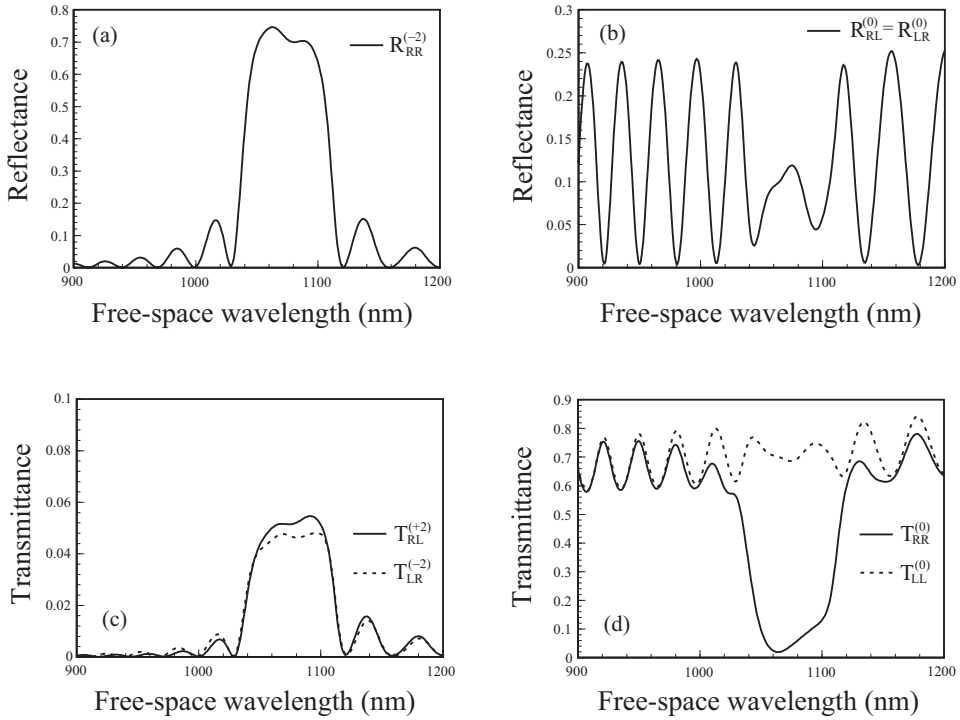

Figure 3.2: Reflectances and transmittances of order n, computed for the same parameters as for Figure 3.1 but with $\alpha = 10°$. Reflectances and transmittances of maximum magnitudes less than 0.01 are not shown.

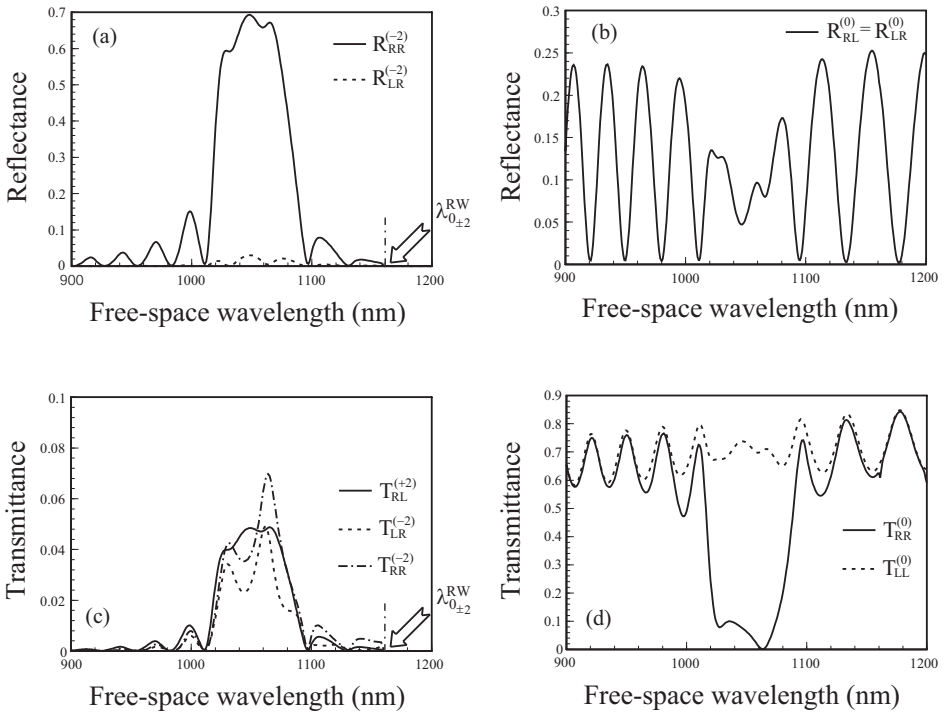

Figure 3.3: Same as Figure 3.2, but for $\alpha = 15°$.

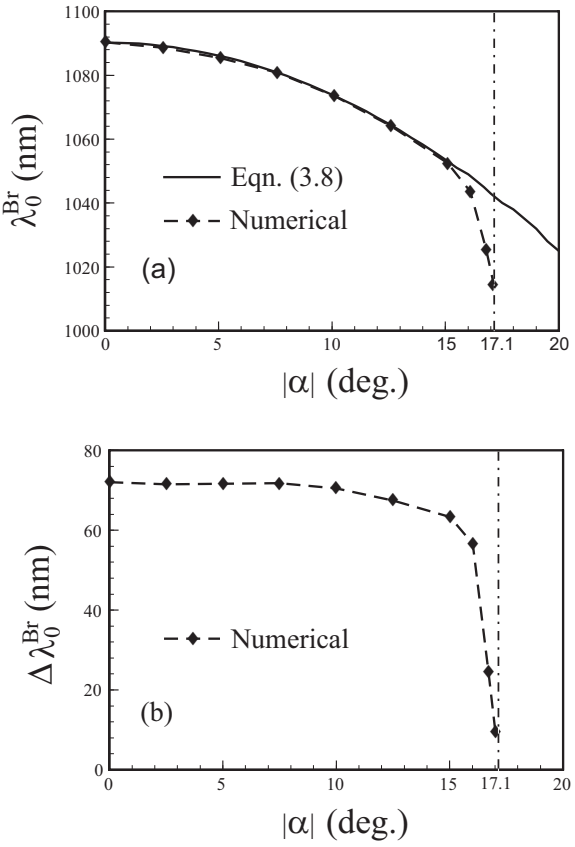

Figure 3.4: (a) Center–wavelength λ_0^{Br} of the Bragg regime as a function of $|\alpha|$, computed using (3.8) (solid line) and the RCWA of Chapter 2 (square–dashed line). (b) The FWHM bandwith $\Delta\lambda_0^{\mathrm{Br}}$ of the Bragg regime computed using the RCWA of Chapter 2.

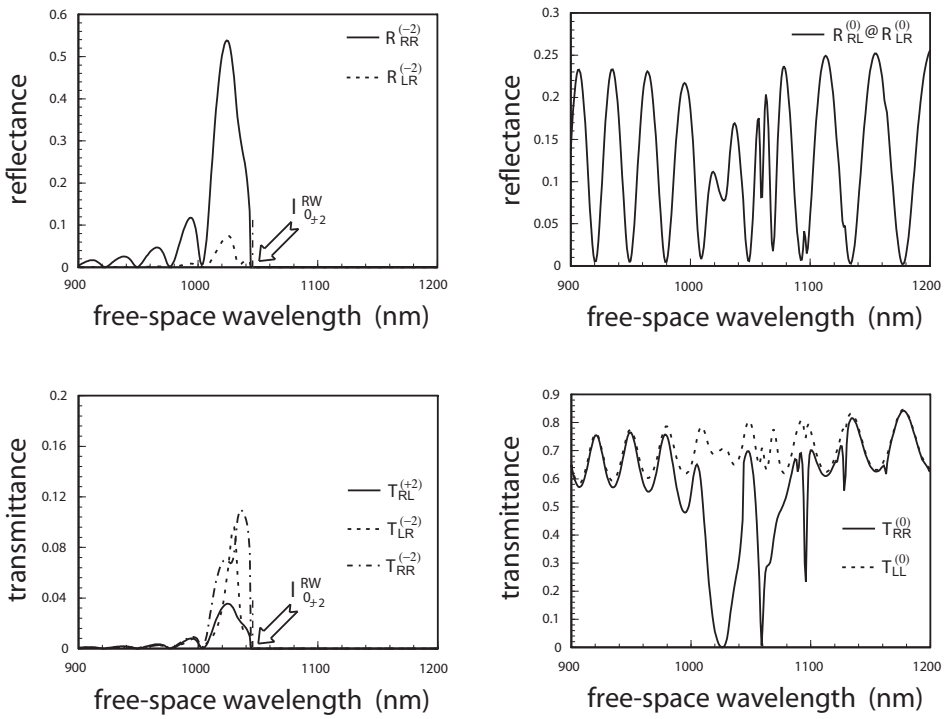

Figure 3.5: Same as Figure 3.2, but for $\alpha = 16.7°$.

Chapter 4

Response of Slanted Chiral STFs to Obliquely Incident Plane Waves[‡]

The response of slanted chiral STFs to normally incident plane waves in Chapter 3 shows that the circular Bragg phenomenon is partly nonspecular for $\alpha \neq 0$, and a Rayleigh–Wood anomaly exerts a dramatic influence on the Bragg regime as $|\alpha|$ increases.

In general, the circular Bragg phenomenon exists also for oblique incidence of plane waves, but it is greatly influenced by the directionality of planewave incidence, as is known for $\alpha = 0$ [27, 28]. Therefore, both spectral (i.e., wavelength–dependence) and angular–spread (i.e., wavevector–dependence) features of the circular Bragg phenomenon need to be characterized for the case of oblique incidence. In this chapter, the response of slanted chiral STFs to obliquely incident plane waves is presented, with a focus on the circular Bragg phenomenon that is affected by both the directionality of planewave incidence and

[‡] This chapter is partly adapted from the following paper: F. Wang, A. Lakhtakia, "Lateral shifts of optical beams on reflection by slanted chiral sculptured thin films", Opt. Commun. **235** 107–132 (2004).

the refractive index n_{hs}. Two problems are considered:

- **Problem A:** The half–spaces of reflection and transmission are vacuous.
- **Problem B:** The half–spaces of reflection and transmission are occupied by a dielectric medium that is optically denser than the slanted chiral STF.

For Problem A, the focus lies on the interaction of circular Bragg phenomenon with the Rayleigh–Wood anomalies; for Problem B, the focus lies on the truncation of the angular spread of the Bragg regime due to the occurrence of total reflection.

4.1 Problem A: Circular Bragg Phenomenon

The most prominent feature of the planewave response of slanted chiral STFs is due to the circular Bragg phenomenon, which is CP–selective reflection in the Bragg regime. The circular Bragg phenomenon is indicated by a high co–handed reflectance in the Bragg regime. Although this reflectance is purely specular for $\alpha = 0$, it is nonspecular for $\alpha \neq 0$ as it occurs in the order $n = \mp 2$ for $\alpha \gtrless 0$, regardless of the structural handedness of the film. The Bragg regime blue–shifts as $|\alpha|$ increases, and diminishes due to the effect of a Rayleigh–Wood anomaly of order $n = \mp 2$ for $\alpha \gtrless 0$. These trends hold for both normal– and oblique–incidence conditions.

Figure 4.1 shows the characteristic spectrums of $\mathrm{R}_{\mathrm{RR}}^{(-2)}$ and $\mathrm{T}_{\mathrm{RR}}^{(0)}$ for arbitrary incidence in either the xz plane (i.e., $\psi_i^p = 0$) or the yz plane (i.e., $\psi_i^p = 90^\circ$) for $\alpha = 10^\circ$. The circular Bragg phenomenon is clearly identifiable as a ridge in plots of $\mathrm{R}_{\mathrm{RR}}^{(-2)}$ and as a trough in the plots of $\mathrm{T}_{\mathrm{RR}}^{(0)}$ for various $\sin\theta_i^p \in (-1, 1)$ in the wavelength–regime $\lambda_0 \in [650, 750]$ nm, because the chosen film is structurally right–handed. Had the film been structurally left–handed, the ridge would be seen in the plots of $\mathrm{R}_{\mathrm{LL}}^{(-2)}$ and the trough in the plots of $\mathrm{T}_{\mathrm{LL}}^{(0)}$.

Figure 4.1 indicates that the Bragg regime blue–shifts more for more obliquely incident plane waves. Moreover, the influence of a Rayleigh–Wood anomaly on the circular Bragg phenomenon is very explicit for obliquely incident plane waves. The angular spread of the Bragg regime — quantitated as the θ_i^p–span of the broad ridge in the plot of $\mathrm{R}_{\mathrm{RR}}^{(-2)}$ — becomes asymmetric with respect to θ_i^p in the xz plane (Figure 4.1(a)), but not in the yz plane (Figure 4.1(c)).

In fact, because of the incidence being oblique, both λ_0^{Br} and $\lambda_{0_n}^{\mathrm{RW}}$ depend on the values of θ_i^p and ψ_i^p. Therefore, (3.8) and (3.9) must undergo changes for oblique incidence. On the one hand, computations suggest that

$$\lambda_0^{\mathrm{Br}} = \Omega \cos\alpha \sqrt{\cos\theta_i^p} \left[\sqrt{\epsilon_c(\lambda_0^{\mathrm{Br}})} + \sqrt{\epsilon_d(\lambda_0^{\mathrm{Br}})} \right] \tag{4.1}$$

provides a good quantitative estimate of λ_0^{Br} when $|\theta_i^p| \leq 30^\circ$, although the actual functional dependence of λ_0^{Br} on both θ_i^p and ψ_i^p might be very complicated. On the other hand, the Rayleigh–Wood anomalies of different orders occur at

$$\lambda_{0_n}^{\mathrm{RW}} = \frac{n_{hs}\Omega}{|n \sin\alpha|} \left[\sqrt{1 - \left(\sin\theta_i^p \sin\psi_i^p\right)^2} - \sin\theta_i^p \cos\psi_i^p \, \mathrm{sign}(n\alpha) \right] \tag{4.2}$$

for oblique incidence in general. Clearly, $\lambda_{0_n}^{\mathrm{RW}} \neq \lambda_{0_{-n}}^{\mathrm{RW}}$ when $\theta_i^p \neq 0$ and $\psi_i^p \neq \pm 90^\circ$.

As the wavevector $\mathbf{k}_+^{(0)}$ tilts away from the z axis, both λ_0^{Br} and $\lambda_{0_{\mp 2}}^{\mathrm{RW}}$ (for $\alpha \gtrless 0$) change noticeably. If $\lambda_{0_{\mp 2}}^{\mathrm{RW}}$ becomes smaller than λ_0^{Br}, the signature of the circular Bragg phenomenon disappears. The wavelength–neighborhood of the disappearance depends strongly on the orientation of the plane of incidence with respect to the plane containing the helical axis (i.e., xz plane); hence, the circular Bragg phenomenon is far from displaying circular symmetry with respect to ψ_i^p when $\alpha \neq 0$, as seen from the contrast between Figures 4.1(a) and 4.1(c).

The dependence of $\lambda_{0_{\mp 2}}^{\mathrm{RW}}$ (for $\alpha \gtrless 0$) on $\sin\theta_i^p \cos\psi_i^p$ is different from that on $\sin\theta_i^p \sin\psi_i^p$. When $\sin\theta_i^p \sin\psi_i^p$ is constant–valued, $\lambda_{0_{\mp 2}}^{\mathrm{RW}}$ changes linearly with $\sin\theta_i^p \cos\psi_i^p$; and the Bragg regime is susceptible to subversion by the Rayleigh–Wood anomaly of order $n = \mp 2$

if $\sin\theta_i^p \cos\psi_i^p \lessgtr 0$. That is the reason for the absence of the Bragg regime in Figures 4.1(a) and 4.1(b) ($\psi_i^p = 0$), for $\sin\theta_i^p \in (-1, -0.37)$. In contrast, $\lambda_{0_{\mp 2}}^{\mathrm{RW}}$ is a monotonically decreasing function of $|\sin\theta_i^p \sin\psi_i^p|$ for constant–valued $\sin\theta_i^p \cos\psi_i^p$. Therefore, in Figures 4.1(c) and 4.1(d) ($\psi_i^p = 90^\circ$), the Bragg regime is completely subverted by the Rayleigh–Wood anomaly of order $n = -2$ in the angular regime $|\sin\theta_i^p| \in (0.83, 1)$.

The influence of the slant angle $\alpha \gtrless 0$ on the subversion of the circular Bragg phenomenon by the Rayleigh–Wood anomaly of order $n = \mp 2$ is available in Chapter 3 for normal incidence. Figures 4.2 and 4.3 present characteristic remittances for arbitrary incidence in either the xz plane or the yz plane for $\alpha = 0$, 5°, 10°, and 15°. For these plots, the wavelength λ_0 was fixed equal to $\lambda_0^{\mathrm{Br}}\Big|_{\theta_i^p = 0}$, which is the center–wavelength of the Bragg regime for normal incidence. Both figures clearly show that the angular spread of the Bragg regime is asymmetric with respect to θ_i^p in the xz plane but symmetric in the yz plane.

The effect of $\alpha \neq 0$ is fairly trivial when the incident plane wave is cross–handed (Figure 4.2), but not when the incident plane wave is co–handed (Figure 4.3). The asymmetric shift of the Bragg regime due to the increase of $\alpha > 0$ is clearly demonstrated in Figures 4.3 by the $\sin\theta_i^p$–span of $\mathrm{R}_{\mathrm{RR}}^{(-2)}$ and $\mathrm{T}_{\mathrm{RR}}^{(0)}$ in the xz plane. When α rises to 15°, new features appear in the plots of $\mathrm{R}_{\mathrm{RR}}^{(-2)}$ and $\mathrm{T}_{\mathrm{RR}}^{(0)}$, as shown by the contrast between 4.3(g) and 4.3(h). While partially subverted by a Rayleigh–Wood anomaly, the crest(trough) feature in $\mathrm{R}_{\mathrm{RR}}^{(-2)}(\mathrm{T}_{\mathrm{RR}}^{(0)})$ splits into two narrower and disconnected portions in Figure 4.3(g), but not in Figure 4.3(h). This major difference implies that the circular Bragg phenomenon, whether or not subverted by a Rayleigh–Wood anomaly, becomes strongly sensitive to the plane of incidence when $|\alpha|$ crosses a threshold value.

4.2 Problem B: Truncation of Angular Spread of Bragg Regime

Experience with chiral STFs indicates that the circular Bragg phenomenon must be affected by the value of n_{hs} [63]. Typically, when the half–spaces $z \leq 0$ and $z \geq d$ are not vacuous, but filled with a homogeneous medium that is optically denser than the slanted chiral STF, the angular spread of the Bragg regime is restricted by the occurrence of total reflection. That is the basic attraction of Problem B for being considered here.

Figures 4.4 and 4.5 present the planewave reflectances for arbitrary incidences when $n_{hs} = 4$ and $\lambda_0 = 727$ nm. The circular Bragg phenomenon still exists but its angular spread is highly restrained, as seen from comparing Figures 4.4 and 4.5. Instead, total reflection into the half–space of incidence occurs when $|\theta_i^p|$ reaches the critical value $\theta_{ic}^p \approx \sin^{-1}0.47$ for both LCP and RCP plane waves, as may be concluded from the plots of $\mathrm{R}_{\mathrm{LL}}^{(0)} + \mathrm{R}_{\mathrm{RL}}^{(0)}$ (Figure 4.4) and the plots of $\mathrm{R}_{\mathrm{LR}}^{(0)} + \mathrm{R}_{\mathrm{RR}}^{(0)}$ (Figure 4.5).

Although the circular Bragg phenomenon is not specular when $\alpha \neq 0$, total reflection is purely specular whether $\alpha = 0$ or not. Indeed, the reflectance plots in Figures 4.4 and 4.5 look independent of α in the total–reflection regime $|\sin\theta_i^p| \in [0.47,\, 1)$, thereby implying the insensitivity of the total–reflection phenomenon to either the structural handedness or the slantedness of the chosen thin film.

4.3 Concluding Remarks

In conclusion, the circular Bragg phenomenon exhibits two remarkable angular–spread features for slanted chiral STFs. These features are summarized as follows:

- The angular spread of the Bragg regime is significantly asymmetric because of the subversion of the circular Bragg phenomenon by the Rayleigh–Wood anomaly, and

- the angular spread is affected by the value of n_{hs} such that it is highly constrained by the occurrence of total reflection.

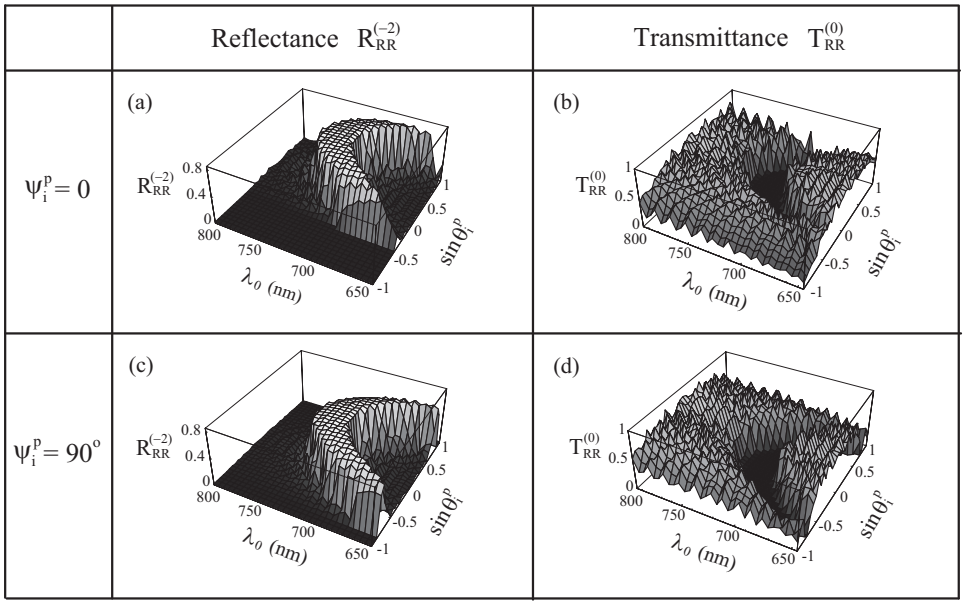

Figure 4.1: Spectrums of reflectance $\mathrm{R}_{\mathrm{RR}}^{(-2)}$ and transmittance $\mathrm{T}_{\mathrm{RR}}^{(0)}$, computed for a slanted chiral STF for oblique planewave incidence. (a, b) $\psi_i^p = 0$; (c, d) $\psi_i^p = 90°$. The various parameters used are as follows: $p_a = 2.0$, $p_b = 2.6$, $p_c = 2.1$, $\mathrm{N}_a = \mathrm{N}_b = \mathrm{N}_c = 500$, $\lambda_a = \lambda_c = 140$ nm, $\lambda_b = 150$ nm, $\Omega = 200$ nm, $d = 60\Omega$, $\alpha = 10°$, $\chi_s = 30°$, $h = 1$, and $n_{hs} = 1$.

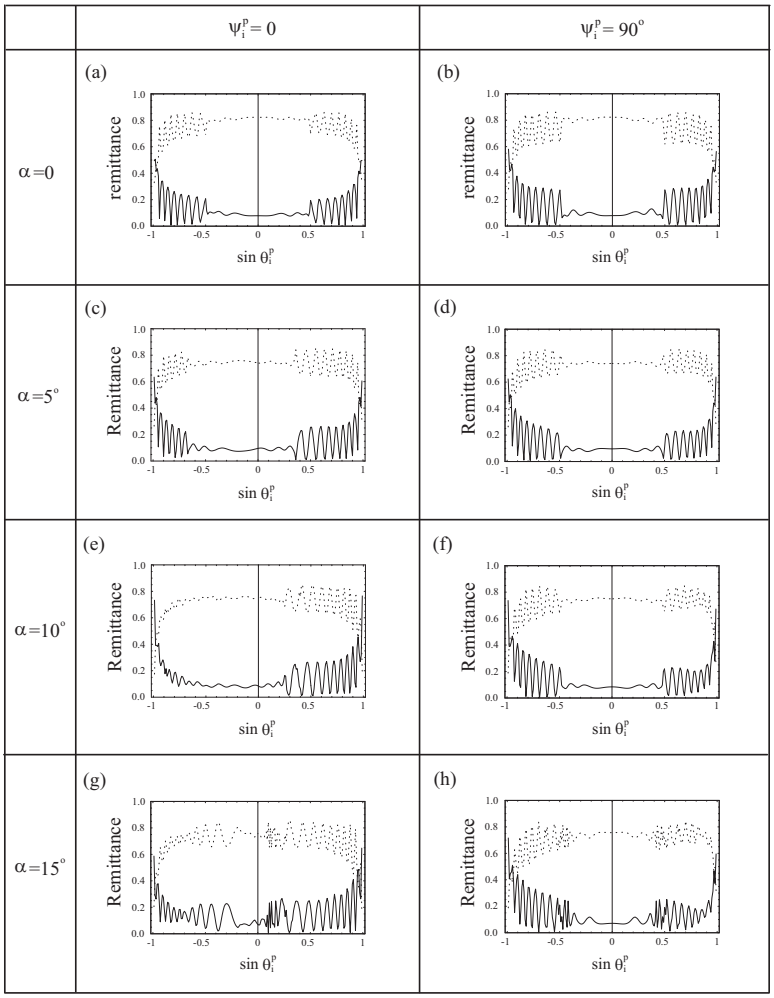

Figure 4.2: Dependences of the remittances $\mathrm{R}^{(0)}_{\mathrm{RL}}+\mathrm{R}^{(0)}_{\mathrm{LL}}$ (solid lines) and $\mathrm{T}^{(0)}_{\mathrm{RL}}+\mathrm{T}^{(0)}_{\mathrm{LL}}$ (dashed lines) on the obliqueness of planewave incidence: (a, c, e, g) $\psi_i^p = 0$; (b, d, f, h) $\psi_i^p = 90°$. The slanted chiral STF has the same parameters as Figure 4.1, but for different values of α: (a, b) $\alpha = 0$; (c, d) $\alpha = 5°$; (e, f) $\alpha = 10°$; and (g, h) $\alpha = 15°$. The wavelength $\lambda_0 = \lambda_0^{\mathrm{Br}}|_{\theta_i^p=0}$, which is the center–wavelength of the Bragg regime for normal incidence.

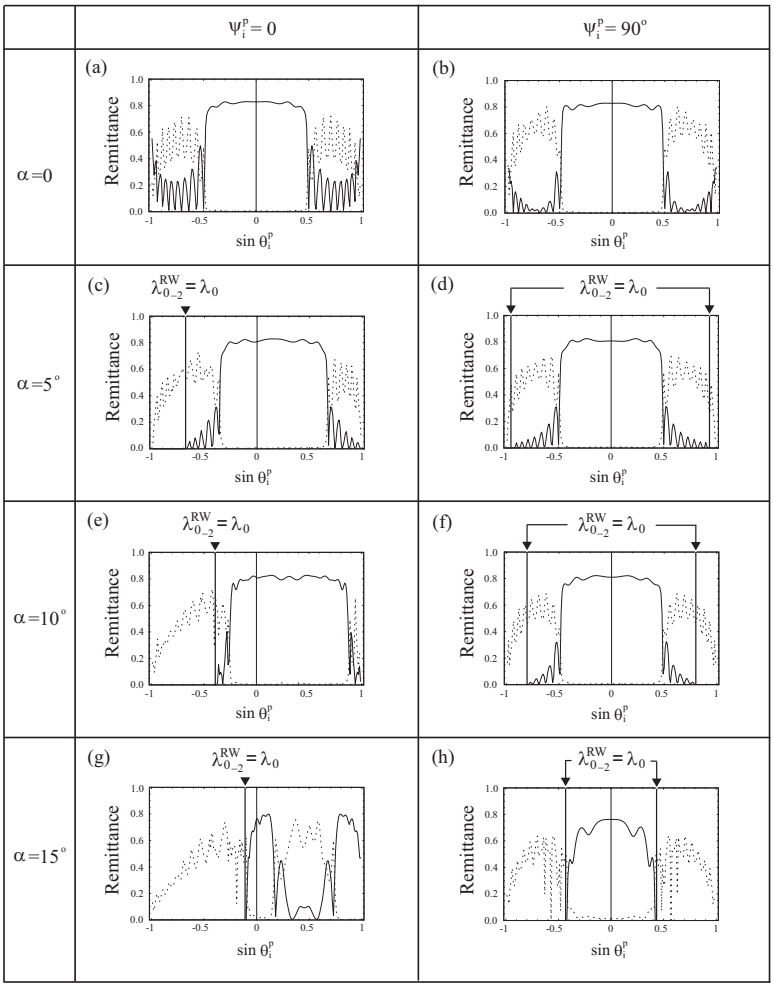

Figure 4.3: Same as Figure 4.2, except that the remittances plotted are $R_{RR}^{(-2)}$ (solid lines) and $T_{RR}^{(0)}$ (dashed lines).

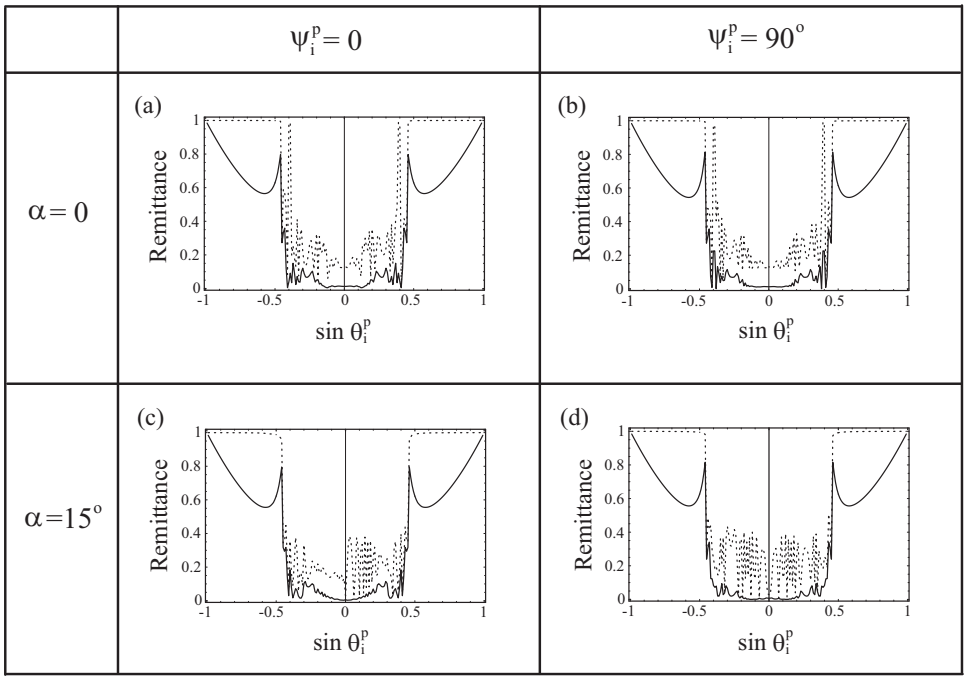

Figure 4.4: Spectrums of reflectances $R_{LL}^{(0)}$ (solid lines) and $R_{LL}^{(0)} + R_{RL}^{(0)}$ (dotted lines), calculated for (a, b) $\alpha = 0$ and (c, d) $\alpha = 15°$. Same parameters as for Figure 4.1, except that $n_{hs} = 4$ and $\lambda_0 = 727$ nm.

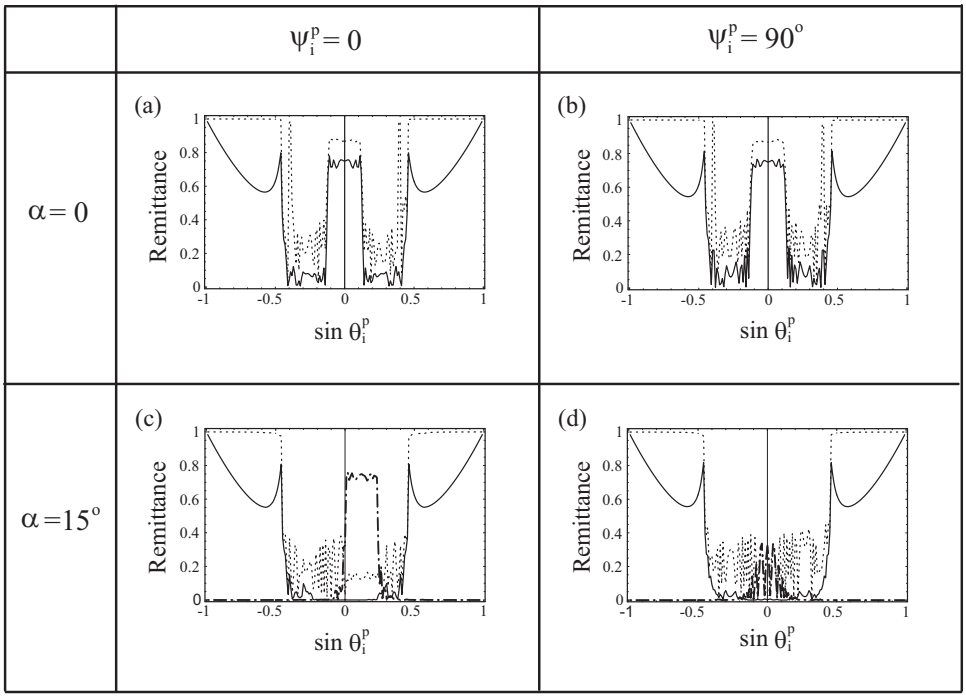

Figure 4.5: Same as Figure 4.4, except that the reflectances plotted are $R_{RR}^{(0)}$ (solid lines), $R_{LR}^{(0)} + R_{RR}^{(0)}$ (dotted lines) and $R_{RR}^{(-2)}$ (dashed–dotted lines). The plots of $R_{RR}^{(-2)}$ are shown only for $\alpha = 15°$.

Chapter 5

Spectral Holes in Slanted Chiral STFs[‡]

The planewave responses of a single–section slanted chiral STF are examined in Chapters 3 and 4, based on the solution procedure devised in Chapter 2. A similar solution procedure can be devised for the planewave responses of multisection slanted chiral STFs. One of the benefits of the construction of multisection slanted chiral STFs is that structural defects can be purposely incorporated to induce resonance phenomenons.

Previous studies have shown the emergence of spectral holes in the Bragg regime of two–section chiral STFs containing either layer or twist defects or both [15, 37, 56]. There are two types of spectral holes in a chiral STF with a central defect, and the evolution of these spectral holes with the thickness of the chiral STF sections gives evidence of a remarkable crossover phenomenon. The objective of this chapter is to identify the spectral holes and the associated crossover phenomenon in slanted chiral STFs with central twist

[‡] This chapter is partly adapted from the following paper: F. Wang, A. Lakhtakia, "Specular and nonspecular, thickness–dependent, spectral holes in a slanted chiral sculptured thin film with a central twist defect", Opt. Commun. **215** 79–92 (2003).

defects.

5.1 Geometry of Twist Defect

The geometry of a slanted chiral STF with a central twist defect is sketched in Figure 5.1. The slanted chiral STF has a thickness of d and is bounded by two vacuous half–spaces (i.e., $n_{hs} = 1$). The central twist defect is introduced by a twist angle $\phi \neq m\pi$ ($m \in \mathbb{Z}$) between the upper and the lower halves about their common axis of nonhomogeneity. The constitutive relations of the slanted chiral STF are delineated in the same way as presented in (2.1) and (2.2), except that the rotational dyadic $\underline{\underline{s}}_z(\mathbf{r})$ of (2.2) is reformulated as

$$\begin{aligned}\underline{\underline{s}}_z(\mathbf{r}) = {} & (\mathbf{u}_x\mathbf{u}_x + \mathbf{u}_y\mathbf{u}_y)\,\cos\left[\frac{\pi}{\Omega}\,(\mathbf{r}\cdot\mathbf{u}_\ell) + \phi_{layer}\right] \\ & + h\,(\mathbf{u}_y\mathbf{u}_x - \mathbf{u}_x\mathbf{u}_y)\,\sin\left[\frac{\pi}{\Omega}\,(\mathbf{r}\cdot\mathbf{u}_\ell) + \phi_{layer}\right] + \mathbf{u}_z\mathbf{u}_z\,,\end{aligned} \tag{5.1}$$

where the auxiliary angle

$$\phi_{layer} = \begin{cases} 0\,, & 0 < z < d/2\,, \\ \phi\,, & d/2 < z < d\,. \end{cases} \tag{5.2}$$

5.2 Solution Procedure for Planewave Response

The slanted chiral STF with a central twist defect can be viewed as a two–section slanted chiral STF, each section of which has a different permittivity dyadic. A numerical solution procedure is devised in Chapter 2 for the planewave response of a single–section slanted chiral STF. Therefore, a similar solution procedure can be devised through RCWA for the planewave response of a slanted chiral STF with a central twist defect.

After following the exact steps from (2.6) to (2.31), the first–order matrix ODE

$$\frac{\mathrm{d}}{\mathrm{d}z}\left[\tilde{\underline{\mathbf{f}}}(z)\right] = i\left[\tilde{\underline{\underline{\mathbf{P}}}}(z)\right]\left[\tilde{\underline{\mathbf{f}}}(z)\right]\,, \quad 0 < z < d \tag{5.3}$$

is derived for the slanted chiral STF being considered. In the presence of a central twist defect, the matrix $\left[\underline{\underline{\tilde{\mathbf{P}}}}(z)\right]$ becomes piecewise uniform such that

$$\left[\underline{\underline{\tilde{\mathbf{P}}}}(z)\right] = \begin{cases} \left[\underline{\underline{\tilde{\mathbf{P}}}}\right]_1 , & 0 < z < d/2 , \\ \left[\underline{\underline{\tilde{\mathbf{P}}}}\right]_2 , & d/2 < z < d . \end{cases} \tag{5.4}$$

where $\left[\underline{\underline{\tilde{\mathbf{P}}}}\right]_\sigma$, $(\sigma = 1, 2)$, is a constant–valued matrix. In accord with (5.2), it is evident that $\left[\underline{\underline{\tilde{\mathbf{P}}}}\right]_1 = \left[\underline{\underline{\tilde{\mathbf{P}}}}\right]$ and $\left[\underline{\underline{\tilde{\mathbf{P}}}}\right]_2$ is related to $\left[\underline{\underline{\tilde{\mathbf{P}}}}\right]$ with the replacement

$$\left[\underline{\underline{\epsilon}}_{\sigma,\sigma'}\right] \Rightarrow \mathrm{Diag}[e^{in\phi}]_{[-\mathrm{N}_t,\mathrm{N}_t]} \left[\underline{\underline{\epsilon}}_{\sigma,\sigma'}\right] \mathrm{Diag}[e^{-in\phi}]_{[-\mathrm{N}_t,\mathrm{N}_t]} \tag{5.5}$$

in (2.33)–(2.37).

To be concise, let $d_\sigma = \sigma d/2$, $(\sigma = 0, 1, 2)$. According to (2.38), the matrix ODE (5.3) has the solution

$$[\underline{\mathbf{f}}(d_{\sigma-1})] = \left[\underline{\underline{\tilde{\mathrm{G}}}}\right]_\sigma \exp\left\{\frac{-id}{2}\left[\underline{\underline{\tilde{\mathrm{D}}}}\right]_\sigma\right\} \left[\underline{\underline{\tilde{\mathrm{G}}}}\right]_\sigma^{-1} [\underline{\mathbf{f}}(d_\sigma)] , \quad \sigma = 1, 2 , \tag{5.6}$$

where the square matrix $\left[\underline{\underline{\tilde{\mathrm{G}}}}\right]_\sigma$ consists of the eigenvectors of $\left[\underline{\underline{\tilde{\mathbf{P}}}}\right]_\sigma$ as its columns; and the diagonal matrix $\left[\underline{\underline{\tilde{\mathrm{D}}}}\right]_\sigma$ contains the eigenvalues of $\left[\underline{\underline{\tilde{\mathbf{P}}}}\right]_\sigma$ in the same order. Combination of (2.40) and (5.6) yields

$$[\underline{\mathbf{f}}(d_{\sigma-1})] = \left[\underline{\underline{\mathrm{G}}}(d_{\sigma-1})\right]_\sigma \exp\left\{\frac{-id}{2}\left[\underline{\underline{\tilde{\mathrm{D}}}}\right]_\sigma\right\} \left[\underline{\underline{\mathrm{G}}}(d_\sigma)\right]_\sigma^{-1} [\underline{\mathbf{f}}(d_\sigma)] , \quad \sigma = 1, 2 , \tag{5.7}$$

where the matrix

$$\left[\underline{\underline{\mathrm{G}}}(z)\right]_\sigma = \left[\underline{\underline{c}}(z)\right] \left[\underline{\underline{\tilde{\mathrm{G}}}}\right]_\sigma \tag{5.8}$$

for $0 \le z \le d$.

Augmented by the boundary values (2.45), the iterative relation (5.7) suffices to determine the unknown $[\underline{\mathrm{R}}]$ and $[\underline{\mathrm{T}}]$. To avoid numerical instability, it is necessary to formulate a stable algorithm from (5.7). This can be done as follows [70, 71, 74]: Let

$$[\underline{\mathbf{f}}(d_\sigma)] = \left[\underline{\underline{\Upsilon}}\right]_\sigma [\underline{\mathrm{T}}]_\sigma , \quad \sigma = 0, 1, 2 , \tag{5.9}$$

where

$$[\underline{\mathrm{T}}]_2 = [\underline{\mathrm{T}}]\ , \quad \left[\underline{\underline{\Upsilon}}\right]_2 = \begin{bmatrix} \left[\underline{\underline{\mathrm{Y}}}_e^+\right] \\ \left[\underline{\underline{\mathrm{Y}}}_h^+\right] \end{bmatrix}\ , \tag{5.10}$$

and

$$[\underline{\mathrm{T}}]_{\sigma-1} = e^{\frac{-id}{2}\left[\tilde{\underline{\underline{\mathrm{D}}}}_u\right]_\sigma} \left[\underline{\underline{v}}_u\right]_\sigma [\underline{\mathrm{T}}]_\sigma\ , \quad \sigma = 1, 2\,. \tag{5.11}$$

Here, $\left[\tilde{\underline{\underline{\mathrm{D}}}}_u\right]_\sigma$ (and $\left[\tilde{\underline{\underline{\mathrm{D}}}}_l\right]_\sigma$) is the upper(lower) diagonal submatrixes of $\left[\tilde{\underline{\underline{\mathrm{D}}}}\right]_\sigma$, while $\left[\underline{\underline{v}}_u\right]_\sigma$ and $\left[\underline{\underline{v}}_l\right]_\sigma$ are defined through the relation

$$\begin{bmatrix} \left[\underline{\underline{v}}_u\right]_\sigma \\ \left[\underline{\underline{v}}_l\right]_\sigma \end{bmatrix} = \left[\underline{\underline{\mathrm{G}}}(d_\sigma)\right]_\sigma^{-1} \left[\underline{\underline{\Upsilon}}\right]_\sigma\ , \quad \sigma = 1, 2\,. \tag{5.12}$$

The substitution of (5.9) and (5.12) into (5.6) yields

$$\left[\underline{\underline{\Upsilon}}\right]_{\sigma-1} = \left[\underline{\underline{\mathrm{G}}}(d_{\sigma-1})\right]_\sigma \begin{bmatrix} \left[\underline{\underline{\mathrm{I}}}\right]_{4\mathrm{N}_t+2} \\ e^{\frac{-id}{2}\left[\tilde{\underline{\underline{\mathrm{D}}}}_l\right]_\sigma} \left[\underline{\underline{v}}_l\right]_\sigma \left\{\left[\underline{\underline{v}}_u\right]_\sigma\right\}^{-1} e^{\frac{id}{2}\left[\tilde{\underline{\underline{\mathrm{D}}}}_u\right]_\sigma} \end{bmatrix}\ , \tag{5.13}$$

which, combined with (5.12), establishes the iterative relation for $\left[\underline{\underline{\Upsilon}}\right]_\sigma$. Algorithm stability is guaranteed for (5.13) by rearrangement of eigenvalues on the diagonal of $\left[\tilde{\underline{\underline{\mathrm{D}}}}\right]_\sigma$ in the order of decreasing magnitude of the imaginary part.

From (5.11)–(5.13), the expressions of $[\underline{\mathrm{T}}]_0$ and $\left[\underline{\underline{\Upsilon}}\right]_0$ are obtained in terms of $[\underline{\mathrm{T}}]_2$ and $\left[\underline{\underline{\Upsilon}}\right]_2$ of (5.10). After partitioning

$$\left[\underline{\underline{\Upsilon}}\right]_0 = \begin{bmatrix} \left[\underline{\underline{\Upsilon}}_u\right]_0 \\ \left[\underline{\underline{\Upsilon}}_l\right]_0 \end{bmatrix}\ , \tag{5.14}$$

and on account of (2.45) and (5.9), $[\underline{\mathrm{R}}]$ and $[\underline{\mathrm{T}}]_0$ are determined as

$$\begin{bmatrix} [\underline{\mathrm{T}}]_0 \\ [\underline{\mathrm{R}}] \end{bmatrix} = \begin{bmatrix} \left[\underline{\underline{\Upsilon}}_u\right]_0 & -\left[\underline{\underline{\mathrm{Y}}}_e^-\right] \\ \left[\underline{\underline{\Upsilon}}_l\right]_0 & -\left[\underline{\underline{\mathrm{Y}}}_h^-\right] \end{bmatrix}^{-1} \begin{bmatrix} \left[\underline{\underline{\mathrm{Y}}}_e^+\right] \\ \left[\underline{\underline{\mathrm{Y}}}_h^+\right] \end{bmatrix} [\underline{\mathrm{A}}]\,. \tag{5.15}$$

Once $[\underline{\mathrm{T}}]_0$ has been determined thus, $[\underline{\mathrm{T}}] = [\underline{\mathrm{T}}]_2$ is easily obtained by reverse iteration of (5.11).

5.3 Characterization of Spectral Holes

5.3.1 Preliminaries

Equations (5.3)–(5.15) suffice to establish a robust solution procedure for the planewave response of a slanted chiral STF with a central twist defect, and calculation of the planewave response is reduced to solving the algebraic equation (5.15) for $[\underline{\mathrm{R}}]$ and $[\underline{\mathrm{T}}]$. Thereafter, reflectances and transmittances can be defined in the same way as in Chapter 3 to characterize the planewave response in the presence of a central twist defect.

The solution procedure was implemented by choosing the following parameters: $p_a = 2.0$, $p_b = 2.6$, $p_c = 2.1$; $\mathrm{N}_a = \mathrm{N}_b = \mathrm{N}_c = 40000$; $\lambda_a = \lambda_c = 140$ nm, $\lambda_b = 150$ nm; $\Omega = 300$ nm; $\chi_s = 30^\circ$; $h = 1$; $\theta_i^p = \psi_i^p = 0$; and $\mathrm{N}_t = 20$. Only integer values of $\mathrm{N}_d = d/\Omega$ were considered, while $\phi = 45^\circ$ and $\phi = 90^\circ$ were selected. The slant angle α was left as a variable. The chosen slanted chiral STF was structurally right–handed, and only the normal–incidence case was examined, although similar results are expected for the oblique–incidence case.

5.3.2 Crossover Phenomenon

Chiral STF with a Central 90°–Twist Defect

Let $\alpha = 0$ first, which provides the chiral STF analog of the CLC considered elsewhere [57]–[55]. The Bragg regime of the otherwise defect–free chiral STF is centered at $\lambda_0^{\mathrm{Br}} = 1090$ nm and the bandwidth $\Delta\lambda_0^{\mathrm{Br}} = 72$ nm; the circular Bragg phenomenon is indicated by a peak in $\mathrm{R}_{\mathrm{RR}}^{(0)}$ and a trough in $\mathrm{T}_{\mathrm{RR}}^{(0)}$, because the chosen chiral STF is structurally right–handed.

In the presence of a central 90°–twist defect, a spectral hole is produced in the center of the Bragg regime, as the preceding studies had suggested [37, 56]. Figure 5.2 shows a nar-

row co–handed reflectance hole (of about 2–nm bandwidth) in $R^{(0)}_{RR}$ and correspondingly, a co–handed transmittance peak in the $T^{(0)}_{RR}$ around $\lambda_0^{Br} = 1090$ nm, when $N_d = 54$.

A cross–handed spectral hole must also be excitable, provided the ratio N_d is sufficiently large. Indeed, Figure 5.3 shows an ultra–narrow cross–handed transmittance hole (about 0.02–nm bandwidth) in $T^{(0)}_{LL}$ and a corresponding cross–handed reflection peak in $R^{(0)}_{LL}$ at the peak wavelength $\lambda_0^p = 1090.328$ nm, when $N_d = 182$.

Therefore, there are two types of spectral holes of opposite circular polarization states, depending on different values of N_d. As the two types of spectral holes evolve with the increase of N_d, a crossover phenomenon can be identified. Figure 5.4 shows the plots of $T^{(0)}_{RR}$ and $R^{(0)}_{LL}$ versus N_d at $\lambda_0^p = 1090.328$ nm. The crossover value of N_d, denoted by N_d^{co}, is that value at which $T^{(0)}_{RR} = R^{(0)}_{LL}$ for $\alpha = 0$. As N_d increases above N_d^{co}, the co–handed reflectance hole wanes and the cross–handed transmittance hole enhances to a steady state.

Slanted Chiral STF with a Central 90°–Twist Defect

For a slanted chiral STF, $\alpha \neq 0$. The circular Bragg phenomenon of a slanted chiral STF is partly nonspecular, indicated by a high co–handed reflectance of order $n = \mp 2$ for $\alpha \gtrless 0$ and a low co–handed specular transmittance in the Bragg regime. The center–wavelength of the Bragg regime for the otherwise defect–free slanted chiral STF blue–shifts as $|\alpha|$ increases, and the width of the Bragg regime decreases towards zero, due to the influence of a Rayleigh–Wood anomaly.

In the presence of a central 90°–twist defect, Figure 5.5 shows the remittance spectrums for $\alpha = 15°$ and $N_d = 54$. A co–handed reflectance hole centered at $\lambda_0^{Br} = 1053$ nm in $R^{(-2)}_{RR}$, and a corresponding co–handed transmittance peak in $T^{(0)}_{RR}$, are clearly evident in Figure 5.5, because the chosen slanted chiral STF is structurally right–handed. The bandwidth of the co–handed reflectance hole is still about 2 nm. Thus, a major effect of

$\alpha \neq 0$ is to also produce a co–handed reflectance hole, but nonspecularly.

That co–handed reflectance hole is absent in the remittance spectrums of Figure 5.6, for which $\alpha = 15°$ and $N_d = 182$. Instead, a cross–handed transmittance hole appears in $T_{LL}^{(0)}$, which is specular; and it is accompanied by cross–handed transmittance/reflectance peaks in $R_{LL}^{(-2)}$, $R_{LL}^{(0)}$, and $T_{LL}^{(-2)}$. The peak wavelength $\lambda_0^p = 1052.80$ nm [‡] and the bandwidth is about 0.15 nm.

Therefore, the crossover phenomenon as shown for $\alpha = 0$ is exhibited for $\alpha \neq 0$ as well, though with different values of N_d^{co}. The value of N_d^{co} for $\alpha \neq 0$ can be estimated from the plots of the peak remittances against N_d, as illustrated in Figure 5.7 for $\alpha = 15°$. The peak remittances at $\lambda_0 = \lambda_0^p$ seem to be varying somewhat irregularly with N_d in Figure 5.7, in contrast to that in Figure 5.4 for $\alpha = 0$. However, the values of $T_{RR}^{(0)}$ and $R_{LL}^{(-2)} + R_{LL}^{(0)} + T_{LL}^{(+2)}$ at $\lambda_0 = \lambda_0^p$ do vary quite smoothly with N_d. From their plots therefore, the value $N_d^{co} = 84$ is determined for $\alpha = 15°$. Only for $N_d < N_d^{co}$ does the co–handed reflectance hole exist in $R_{RR}^{(\mp 2)}$ for $\alpha \gtrless 0$; when $N_d > N_d^{co}$, the cross–handed transmittance hole in $T_{LL}^{(0)}$ takes over just as for $\alpha = 0$.

5.3.3 Parametric Characterization

Effect of Slant Angle α

While the cross–handed transmittance hole always occurs in $T_{LL}^{(0)}$ for $N_d > N_d^{co}$, the corresponding cross–handed reflectance peaks appear in Floquet harmonics of different orders as $\alpha \neq 0$ changes. Figure 5.8 shows the cross–handed reflectance peaks of different orders for $\alpha = 5°$, $10°$, $15°$ and $16.7°$ respectively, when $N_d = 182$. The cross–handed transmittance hole in $T_{LL}^{(0)}$ shown in Figure 5.8 is nearly unaffected by α, though its bandwidth increases

[‡]Actually, λ_0^p turns out to be a function of both α and N_d. For $\alpha = 0$, $\lambda_0^p = 1090.328$ nm for all N_d. In contrast, λ_0^p varies from 1052.65 nm to 1053.75 nm as N_d changes from 50 to 200, when $\alpha = 15°$.

with $\alpha > 0$ (with the exception of $\alpha = 16.7°$). But the co–handed reflectance peak shifts from a nonspecular order ($R_{LL}^{(+2)}$) to the specular order ($R_{LL}^{(0)}$), and then is shared by the specular and the other nonspecular orders ($R_{LL}^{(0)}$ and $R_{LL}^{(-2)}$), as $\alpha > 0$ increases up to 15°. A further increase in α returns the peak in Figure 5.8 to the specular order.

In fact, as $|\alpha|$ increases beyond 15°, the circular Bragg phenomenon is subverted by a Rayleigh–Wood anomaly, as shown in Chapter 3. That is the reason why the co–handed reflectance hole in $R_{RR}^{(-2)}$ is absent in Figure 5.9 for $\alpha = 16.7°$ and $N_d = 54$. But the cross–handed transmittance hole in $T_{LL}^{(0)}$ survives at about $\lambda_0^p = 1043.98$ nm when $N_d = 182$ (Figure 5.8(d)). For $|\alpha| > 17.1°$, the circular Bragg phenomenon vanishes completely, and in consequence, neither of the two types of spectral holes exists.

Effect of Dissipation

Though the slanted chiral STF is very weakly dissipative, significant absorption occurs for an incident cross–handed CP plane wave in the wavelength–regime of the cross–handed transmittance hole. In contrast, the absorbance for an incident co–handed CP plane wave first increases to a small value (< 0.1) as N_d increases to N_d^{co}, and then drops to a minuscule value (< 0.01). Figure 5.10 shows the absorbance spectrums for LCP incidence in a chiral STF ($\alpha = 0$) and a slanted chiral STF ($\alpha = 15°$) as before, when $N_d = 182$. Clearly, absorbance is higher for the chiral STF than for the slanted chiral STF, in their respective cross–handed transmittance hole regimes.

When dissipation in the slanted chiral STF is enhanced — for example, by choosing smaller $N_{a,b,c}$ in (2.4) — it is found that the cross–handed transmittance hole for $N_d > N_d^{co}$ fades away, although the co–handed reflectance hole still exists for $N_d < N_d^{co}$. This conclusion is not surprising because the cross–handed transmittance hole is affected by the entire thickness d of the thin film, whereas the co–handed reflectance hole is affected only by the first few structural periods [75].

Effect of Twist Angle ϕ

Finally, the twist angle $\phi \neq \frac{m_o\pi}{2}$ (m_o is an odd integer) affects the spectral holes too. Most significantly, the spectral holes are not located roughly in the center of the Bragg regime as for $\phi = \frac{m_o\pi}{2}$, but are shifted towards the edges of the Bragg regime when $\phi \neq \frac{m\pi}{2}$. This is illustrated by Figures 5.11 and 5.12 — which show the spectral holes of the slanted chiral STF as before ($\alpha = 15°$), but with $\phi = 45°$. Evidently, the spectral holes, located close to 1071 nm, are blue–shifted in the Bragg regime.

5.4 Concluding Remarks

In conclusion, there are several remarkable features of the spectral holes exhibited in a slanted chiral STF with a central twist defect. These features are summarized as follows:

- Two types of spectral holes are excitable by CP plane waves — one is the co–handed reflectance hole, and the second is the cross–handed transmittance hole.
- There is a crossover phenomenon associated with the evolution of the two types of spectral holes with the increase of thickness.
- The bandwidth of the cross–handed transmittance hole is significantly smaller than that of the co–handed reflectance hole.
- The co–handed reflectance hole is nonspecular for $\alpha \neq 0$, while the cross–handed transmittance hole is always specular.
- The spectral holes occur in the center of the Bragg regime, when the twist angle $\alpha = \frac{m_o\pi}{2}$ (m_o is an odd integer); they are shifted towards the edges of the Bragg regime when $\phi \neq \frac{m\pi}{2}$ ($m \in \mathbb{Z}$).

- The spectral holes are accompanied by spectral peaks in the corresponding transmittance and reflectance spectrums. In contrast to the co–handed transmittance peak which is always specular for $\alpha \neq 0$, the cross–handed reflectance peak happens in Floquet harmonics of different orders as $\alpha \neq 0$ changes.

- Even for weakly dissipative slanted chiral STFs, the cross–handed transmittance hole is accompanied by substantial absorption.

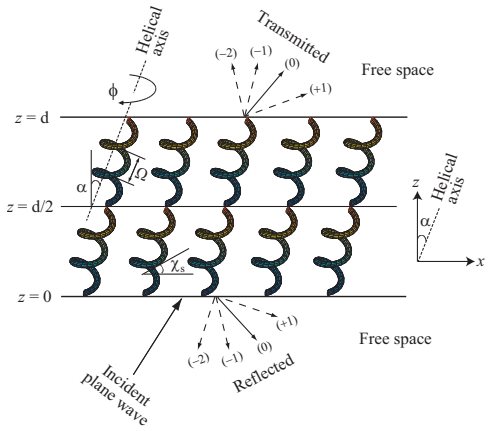

Figure 5.1: Schematic of the boundary value problem involving a slanted chiral STF with a central twist defect. The twist defect is introduced by a twist angle $\phi \neq m\pi$ ($m \in \mathbb{Z}$) between the upper and the lower halves about the axis of nonhomogeneity. Nonspecular reflection and transmission can occur because $\alpha \neq 0$.

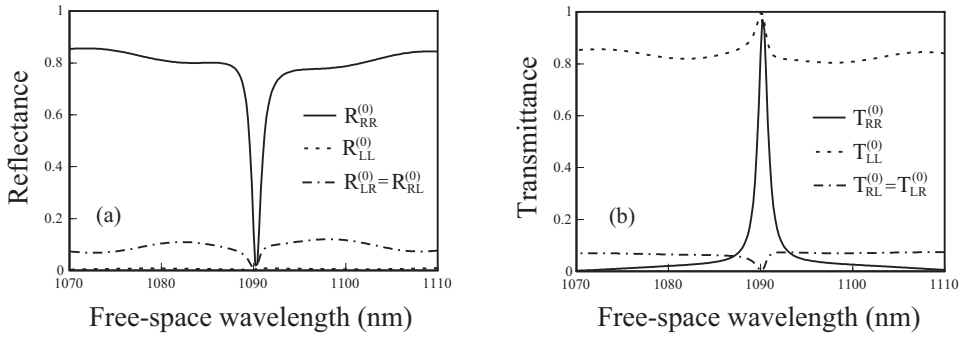

Figure 5.2: (a) Reflectances $\mathrm{R}^{(0)}_{\mathrm{RR}}$, etc., and (b) transmittances $\mathrm{T}^{(0)}_{\mathrm{RR}}$, etc., computed for the chiral STF with the following parameters: $p_a = 2.0$, $p_b = 2.6$, $p_c = 2.1$, $\mathrm{N}_a = \mathrm{N}_b = \mathrm{N}_c = 40000$, $\lambda_a = \lambda_c = 140$ nm, $\lambda_b = 150$ nm, $\Omega = 300$ nm, $\mathrm{N}_d = 54$, $\alpha = 0$, $\chi_s = 30°$, $\phi = 90°$, $h = 1$, $n_{hs} = 1$, and $\theta_i^p = \psi_i^p = 0$.

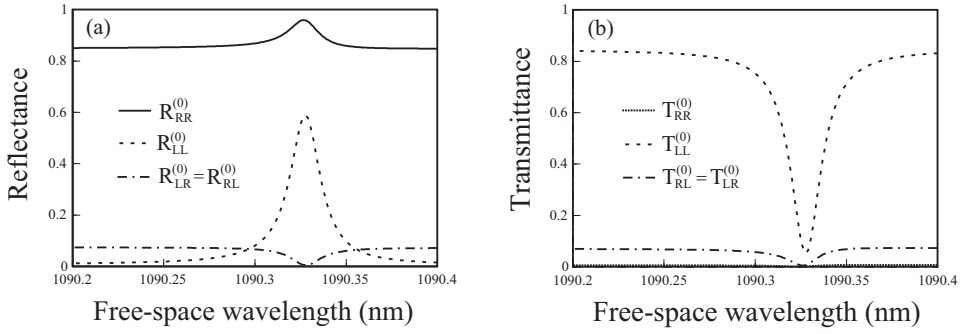

Figure 5.3: Same as Figure 5.2, but for $\mathrm{N}_d = 182$.

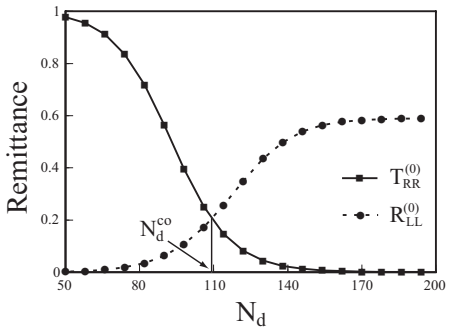

Figure 5.4: Transmittance $T_{RR}^{(0)}$ and reflectance $R_{LL}^{(0)}$ versus N_d at the peak wavelength $\lambda_0^p = 1090.328$ nm for $\alpha = 0$. The crossover value of N_d is determined as $N_d^{co} = 109$.

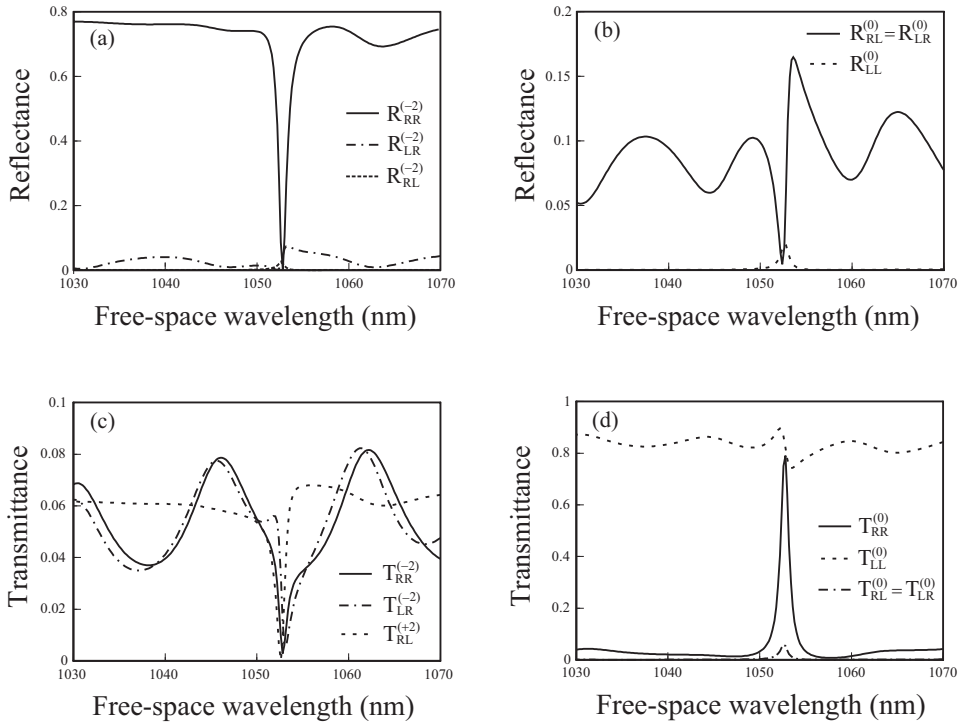

Figure 5.5: (a, b) Nonspecular and specular reflectances and (c, d) nonspecular and specular transmittances of order n, computed with the same parameters as those for Figure 5.2 but with $\alpha = 15°$. Remittances of maximum magnitudes less than 0.01 are not shown.

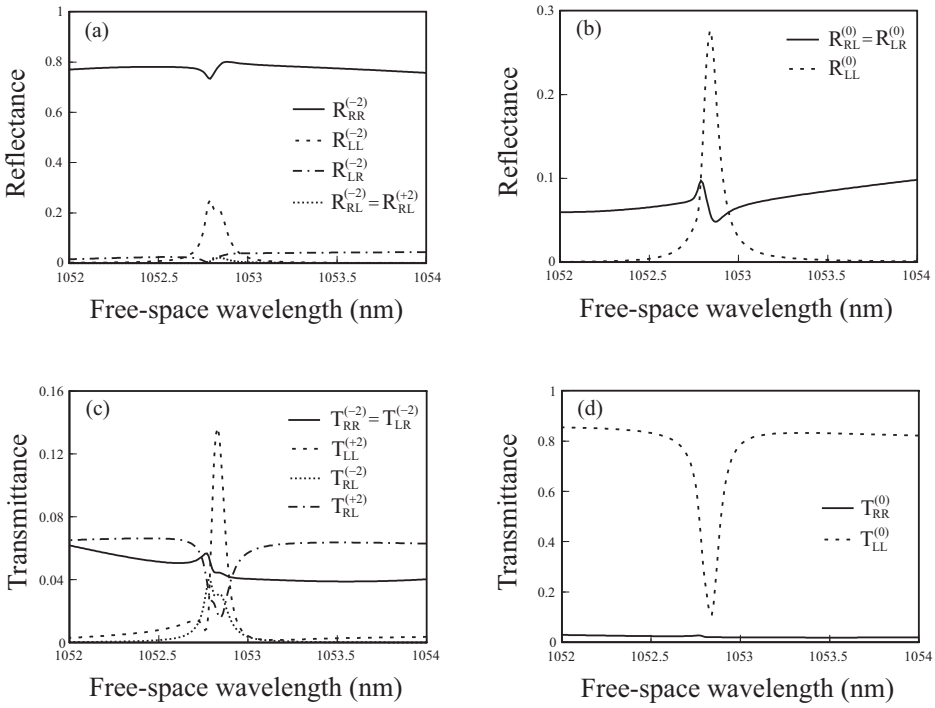

Figure 5.6: Same as Figure 5.5, but for $N_d = 182$.

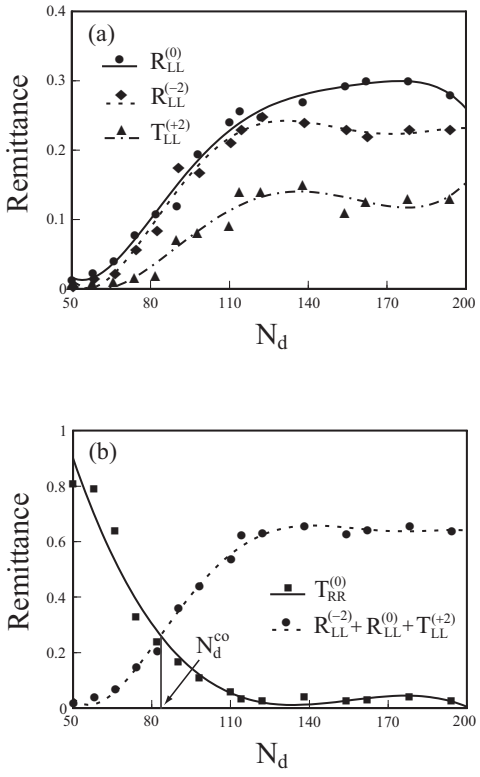

Figure 5.7: (a) $R_{LL}^{(-2)}$, $R_{LL}^{(0)}$ and $T_{LL}^{(+2)}$, and (b) $T_{RR}^{(0)}$ and $R_{LL}^{(-2)} + R_{LL}^{(0)} + T_{LL}^{(+2)}$ versus N_d at the peak wavelength λ_0^p for $\alpha = 15°$. The curves are obtained by least–squares fitting of the fifth–order polynomials to the computed data (shown by heavy dots). The crossover value of N_d is determined as $N_d^{co} = 84$.

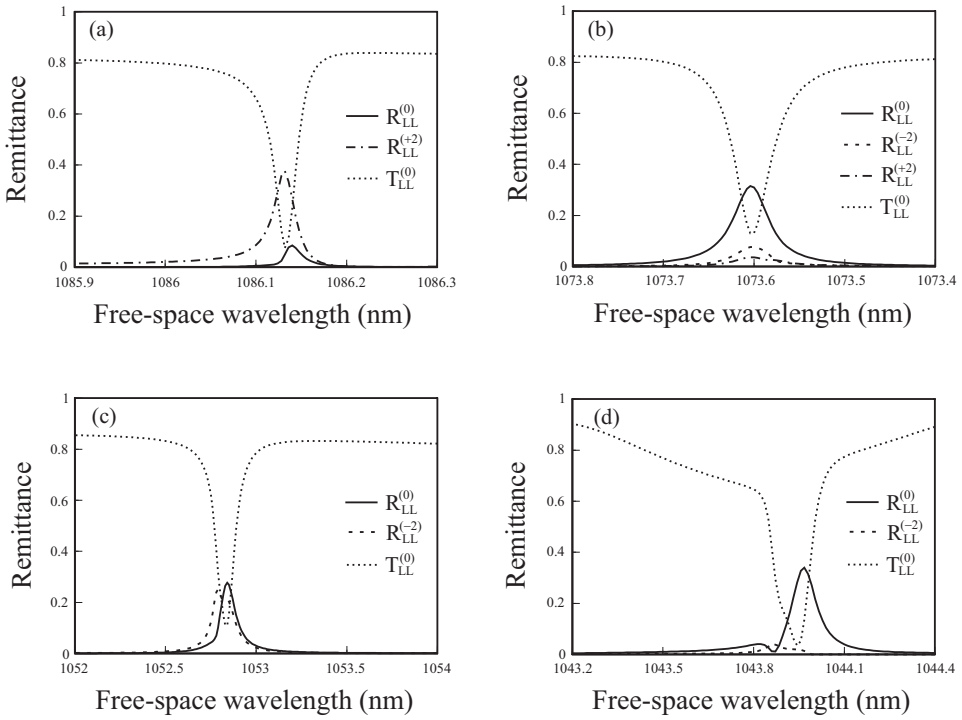

Figure 5.8: Reflectances $R_{LL}^{(n)}$ $(n = 0, \pm 2)$ and transmittance $T_{LL}^{(0)}$, computed for (a) $\alpha = 5°$, (b) $\alpha = 10°$, (c) $\alpha = 15°$ and (d) $\alpha = 16.7°$. See Figure 5.6 for other parameters.

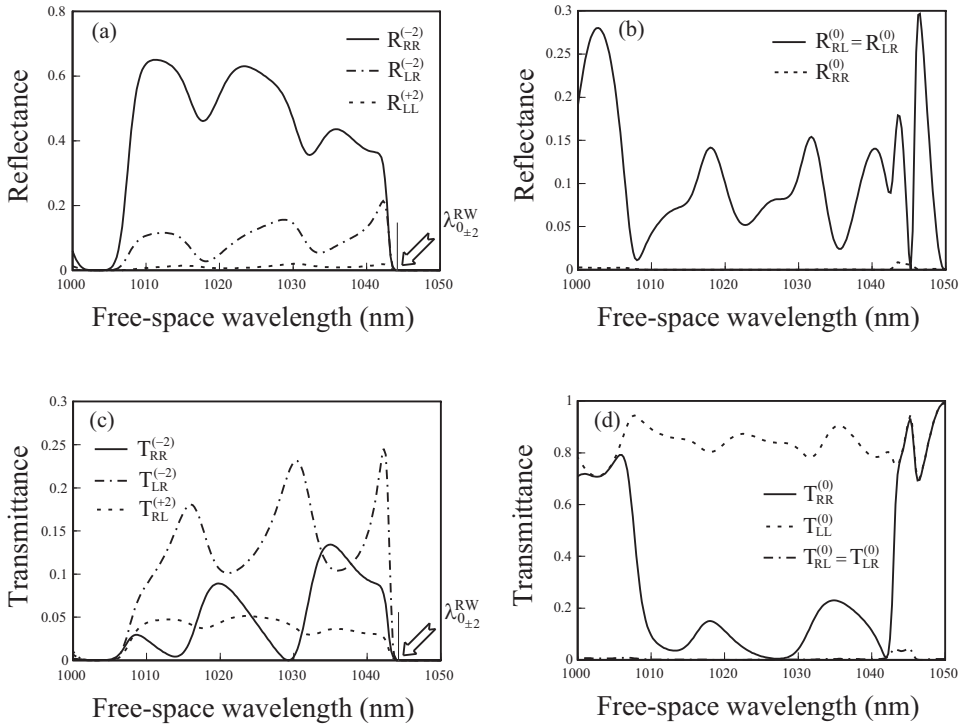

Figure 5.9: Same as Figure 5.5, but for $\alpha = 16.7°$.

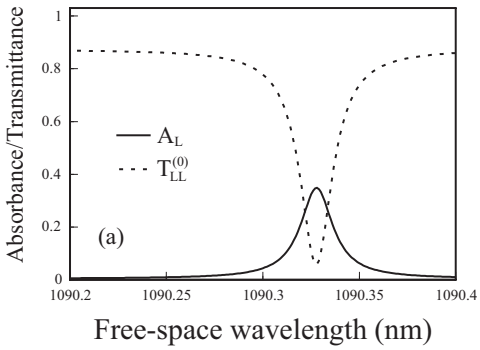

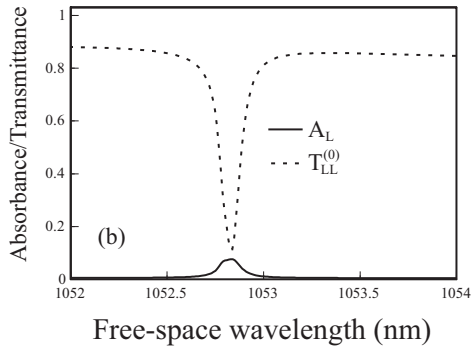

Figure 5.10: Absorbance $A_{\mathrm{L}} = 1 - \sum_{|n|\leq \mathrm{N}_t} \left[\mathrm{R}_{\mathrm{RL}}^{(n)} + \mathrm{R}_{\mathrm{LL}}^{(n)} + \mathrm{T}_{\mathrm{RL}}^{(n)} + \mathrm{T}_{\mathrm{LL}}^{(n)} \right]$ for LCP incidence for (a) $\alpha = 0$ and (b) $\alpha = 15°$, when $\mathrm{N}_d = 182$. For comparison, $\mathrm{T}_{\mathrm{LL}}^{(0)}$ is also plotted. See Figure 5.6 for other parameters.

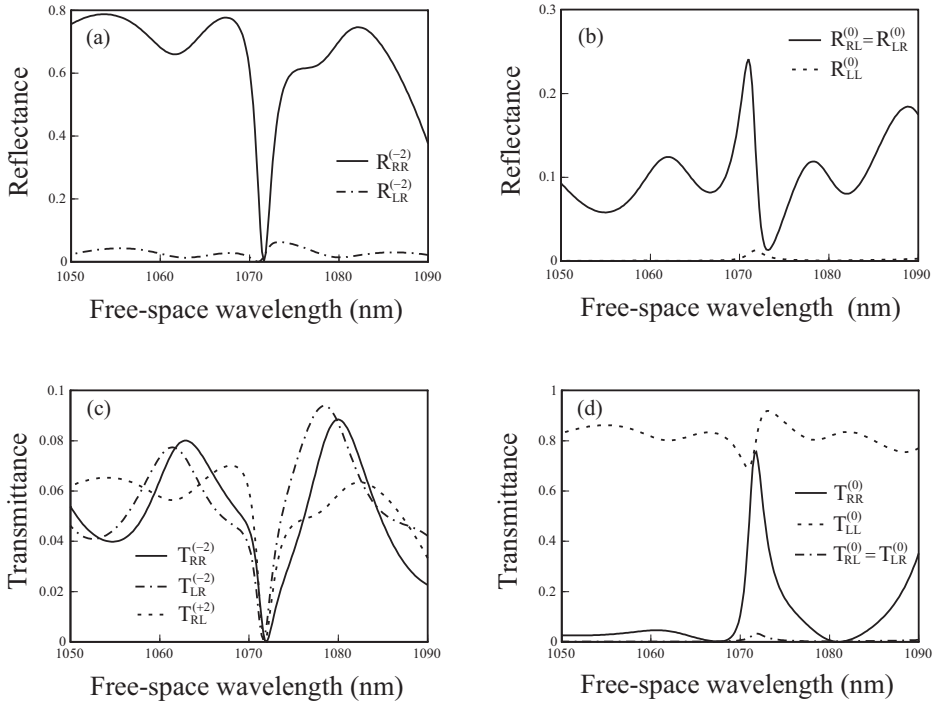

Figure 5.11: Same as Figure 5.5, but for $\phi = 45°$.

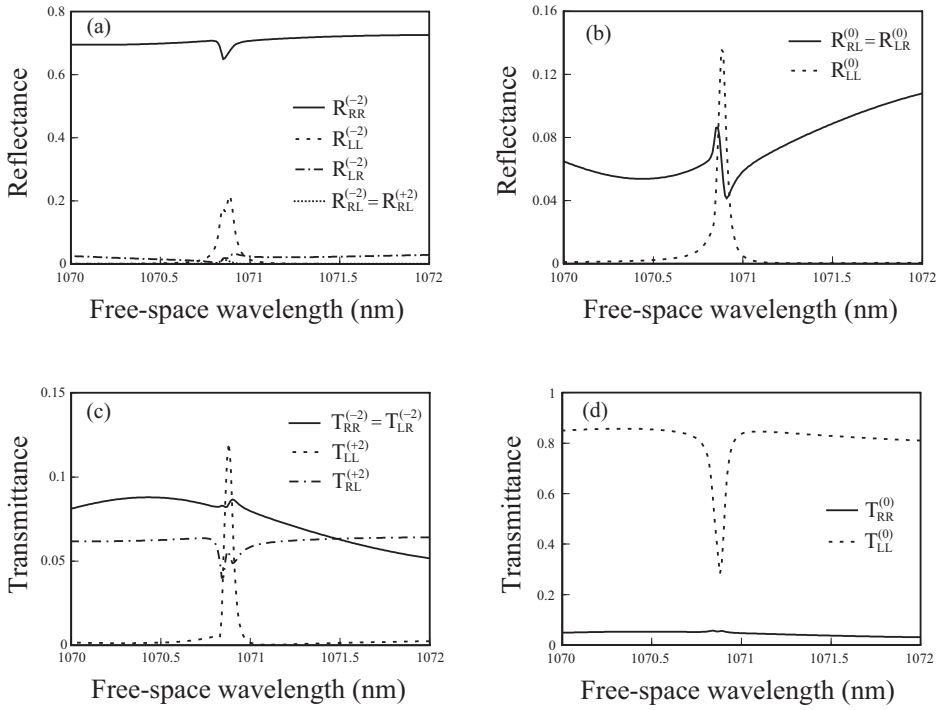

Figure 5.12: Same as Figure 5.6, but for $\phi = 45°$.

Chapter 6

Analytical Approach to the Crossover Phenomenon in Chiral STFs

The exhibition of two types of spectral holes in a slanted chiral STF with a central twist defect is established in Chapter 5, based on a numerical solution procedure devised using RCWA. Notably, there is a crossover phenomenon associated with the occurrence of the two types of spectral holes: A co–handed reflectance hole is seen when the chosen thin film is relatively thin, but a cross–handed transmittance hole takes over when the thickness is large. The same crossover phenomenon also occurs in other types of chiral structures, such as chiral STFs and CLCs.

There is a need to theoretically understand the crossover phenomenon rather than simply examine it numerically. Kopp & Genack [57] and Schmidtke & Stille [59] formulated the existence of a localized defect mode to explain the crossover phenomenon in CLCs. Oldano [76] and Becchi *et al.* [58] pointed out that the defect mode in CLCs has both

spatially localized and nonlocalized components, because the electromagnetic modes in an axially excited CLC or chiral STF are not circularly polarized, in general [77]. Both Oldano and Kopp & Genack agreed that an analytic explanation of the crossover phenomenon is greatly desirable.

The objective of this chapter is to present an analytical explanation of the crossover phenomenon for chiral STFs. A similar explanation should hold for slanted chiral STFs as well, but the focus is kept on $\alpha = 0$ to keep analysis tractable. An analytic treatment of the central 90°–twist defect in a chiral STF is presented here.

6.1 Formalism of Coupled–Wave Theory

6.1.1 Geometry of the Problem

Let the region $0 < z < d$ be occupied by a chiral STF with a central twist defect of $\phi = 90°$, as shown in Figure 6.1, while the two half–spaces $z \leq 0$ and $z \geq d$ are filled with a homogenous, isotropic, dielectric medium of refractive index n_{hs}. The formulas of Chapter 5 apply with $\alpha = 0$ and $\phi = \pi/2$.

6.1.2 Coupled–Wave ODEs

A plane wave is normally incident on to the plane $z = 0$ from the half–space $z \leq 0$. As a result, the chiral STF is axially excited, such that the electromagnetic field phasors $\mathbf{E}(\mathbf{r})$ and $\mathbf{H}(\mathbf{r})$ are independent of x and y, i.e.,

$$\mathbf{E}(\mathbf{r}) \equiv \mathbf{E}(z) = \sum_{\sigma=x,y,z} \mathrm{E}_\sigma(z)\mathbf{u}_\sigma \tag{6.1}$$

and

$$\mathbf{H}(\mathbf{r}) \equiv \mathbf{H}(z) = \sum_{\sigma=x,y,z} \mathrm{H}_\sigma(z)\mathbf{u}_\sigma \,. \tag{6.2}$$

The Maxwell curl postulates in (2.21) now reduce to the ODEs

$$\left.\begin{array}{l} \mathbf{u}_z \times \frac{\mathrm{d}}{\mathrm{d}z}\mathbf{E}(z) = i\omega\mu_0\mathbf{H}(z) \\ \mathbf{u}_z \times \frac{\mathrm{d}}{\mathrm{d}z}\mathbf{H}(z) = -i\omega\epsilon_0\underline{\underline{\epsilon}}(z)\cdot\mathbf{E}(z) \end{array}\right\}, \quad 0 < z < d\,, \tag{6.3}$$

for axial wave propagation in the chiral STF. By projecting (6.3) onto the subspace perpendicular to the z axis (i.e., xy plane), the following matrix ODEs for axial wave propagation are obtained [32]:

$$\left.\begin{array}{l} \frac{\mathrm{d}}{\mathrm{d}z}\left(\left[\begin{array}{cc} 0 & -1 \\ 1 & 0 \end{array}\right] \, [\underline{\mathrm{E}}_\perp(z)] \right) = ik_0 \, [\underline{\mathrm{H}}'_\perp(z)] \\ \frac{\mathrm{d}}{\mathrm{d}z}\left(\left[\begin{array}{cc} 0 & -1 \\ 1 & 0 \end{array}\right] \, [\underline{\mathrm{H}}'_\perp(z)] \right) = -ik_0 \, \left[\underline{\underline{\epsilon}}_{perp}(z)\right] \, [\underline{\mathrm{E}}_\perp(z)] \end{array}\right\}, \qquad 0 < z < d\,. \tag{6.4}$$

Here,

$$[\underline{\mathrm{E}}_\perp(z)] = [\mathrm{E}_x(z)\,,\ \mathrm{E}_y(z)]^{\mathrm{T}}\,, \quad \left[\underline{\mathrm{H}}'_\perp(z)\right] = [\eta_0\mathrm{H}_x(z)\,,\ \eta_0\mathrm{H}_y(z)]^{\mathrm{T}} \tag{6.5}$$

are 2–column vectors;

$$\left[\underline{\underline{\epsilon}}_{perp}(z)\right] = \left\{ \left[\underline{\underline{\epsilon}}(z)\right]_\perp^{-1} \right\}^{-1} \tag{6.6}$$

is a 2×2 matrix; $\left[\underline{\underline{\epsilon}}(z)\right]$ is the matrix form of $\underline{\underline{\epsilon}}(z)$; and $\left[\underline{\underline{\epsilon}}(z)\right]_\perp^{-1}$ is obtained by neglecting all components of $\left[\underline{\underline{\epsilon}}(z)\right]^{-1}$ on the z axis.

By simply eliminating $[\underline{\mathrm{H}}'_\perp(z)]$ in (6.4), the matrix ODE

$$\frac{\mathrm{d}^2}{\mathrm{d}z^2}\,[\underline{\mathrm{E}}_\perp(z)] + k_0^2\left[\underline{\underline{\epsilon}}_{perp}(z)\right]\,[\underline{\mathrm{E}}_\perp(z)] = [\underline{0}]_2\,, \tag{6.7}$$

analogous to the homogenous Helmholtz equation, is obtained for the axial variation of $[\underline{\mathrm{E}}_\perp(z)]$.

Analytic solution of the second–order ODE (6.7) needs an appropriate expansion of the matrix $\left[\underline{\underline{\epsilon}}_{perp}(z)\right]$. The axial periodicity of chiral STFs suggests that $\left[\underline{\underline{\epsilon}}_{perp}(z)\right]$ can be decomposed into a Fourier series [78]. According to (2.2) and (5.2), the Fourier represen-

tation of $\left[\underline{\underline{\epsilon}}_{perp}(z)\right]$ in (6.6) is

$$\left[\underline{\underline{\epsilon}}_{perp}(z)\right] = \begin{cases} \bar{\epsilon}\,\left[\underline{\underline{\mathrm{I}}}\right]_2 + \delta_\epsilon\,\left[\underline{\underline{\mathrm{F}}}\right] e^{i2\pi z/\Omega} + \delta_\epsilon\left[\underline{\underline{\mathrm{F}}}\right]^* e^{-i2\pi z/\Omega}\,, & 0 < z < d\,, \\ \bar{\epsilon}\,\left[\underline{\underline{\mathrm{I}}}\right]_2 - \delta_\epsilon\,\left[\underline{\underline{\mathrm{F}}}\right] e^{i2\pi z/\Omega} - \delta_\epsilon\left[\underline{\underline{\mathrm{F}}}\right]^* e^{-i2\pi z/\Omega}\,, & d < z < 2d\,, \end{cases} \tag{6.8}$$

where the scalars

$$\left.\begin{aligned} \bar{\epsilon} &= (\epsilon_d + \epsilon_c)/2 \\ \delta_\epsilon &= (\epsilon_d - \epsilon_c)/2 \end{aligned}\right\}, \tag{6.9}$$

the 2×2 matrix

$$\left[\underline{\underline{\mathrm{F}}}\right] = \begin{bmatrix} 1 & -hi \\ -hi & -1 \end{bmatrix}, \tag{6.10}$$

and the superscript * denotes the complex conjugate.

Now, on neglecting the perturbation factor δ_ϵ in (6.8), the ODE (6.7) yields the solution

$$\left[\underline{\mathrm{E}}_\perp(z)\right] = \left[\underline{\mathrm{B}}^+\right] e^{ikz} + \left[\underline{\mathrm{B}}^-\right] e^{-ikz}\,, \tag{6.11}$$

where $k = k_0\bar{n}$, $\bar{n} = \sqrt{\bar{\epsilon}}$, and $\left[\underline{\mathrm{B}}^\pm\right]$ are constant–valued 2–column vectors. Therefore, it is natural to render

$$\left[\underline{\mathrm{E}}_\perp(z)\right] = \left[\underline{\mathrm{B}}^+(z)\right] e^{ikz} + \left[\underline{\mathrm{B}}^-(z)\right] e^{-ikz} \tag{6.12}$$

as the solution of ODE (6.7) without ignoring δ_ϵ. Thus, (6.12) is nothing but a modification of (6.11) with variable $\left[\underline{\mathrm{B}}^\pm(z)\right]$ accounting for the periodic nature of $\left[\underline{\underline{\epsilon}}_{perp}(z)\right]$.

Furthermore, in light of the circular–polarization–discriminatory optical responses of chiral STFs, it is useful to transform $\left[\underline{\mathrm{B}}^\pm(z)\right]$ into their CP counterparts $\left[\tilde{\underline{\mathrm{B}}}^\pm(z)\right]$ by

$$\left[\underline{\mathrm{B}}^\pm(z)\right] = \left[\underline{\underline{\mathrm{Y}}}\right]\left[\tilde{\underline{\mathrm{B}}}^\pm(z)\right], \tag{6.13}$$

where the transformation matrix

$$\left[\underline{\underline{\mathrm{Y}}}\right] = \frac{1}{\sqrt{2}}\begin{bmatrix} 1 & 1 \\ i & -i \end{bmatrix}. \tag{6.14}$$

While the components of the 2–column vectors

$$\left[\underline{\mathrm{B}}^{\pm}(z)\right] = \begin{bmatrix} \mathrm{B}_x^{\pm}(z) \\ \mathrm{B}_y^{\pm}(z) \end{bmatrix} \tag{6.15}$$

are understood in the cartesian coordinate system, the components of the 2–column vectors

$$\left[\tilde{\underline{\mathrm{B}}}^{+}(z)\right] = \begin{bmatrix} \mathrm{B}_{\mathrm{L}}^{+}(z) \\ \mathrm{B}_{\mathrm{R}}^{+}(z) \end{bmatrix}, \quad \left[\tilde{\underline{\mathrm{B}}}^{-}(z)\right] = \begin{bmatrix} \mathrm{B}_{\mathrm{R}}^{-}(z) \\ \mathrm{B}_{\mathrm{L}}^{-}(z) \end{bmatrix} \tag{6.16}$$

are LCP and RCP, as indicated by the subscripts $_{\mathrm{L}}$ and $_{\mathrm{R}}$.

By substituting (6.8), (6.12) and (6.13) into the ODE (6.7), and enforcing the mutual orthogonalities of LCP and RCP phasors, the following coupled–wave ODEs are derived:

$$\left.\begin{aligned} \tfrac{1}{k_0^2}\tfrac{\mathrm{d}^2}{\mathrm{d}z^2}\left[\tilde{\underline{\mathrm{B}}}^{+}(z)\right] + \tfrac{2ik}{k_0^2}\tfrac{\mathrm{d}}{\mathrm{d}z}\left[\tilde{\underline{\mathrm{B}}}^{+}(z)\right] &= \mp\delta_\epsilon \left\{ \left[\tilde{\underline{\underline{\mathrm{F}}}}^{+}\right]\left[\tilde{\underline{\mathrm{B}}}^{-}(z)\right] e^{-2i(k-\pi/\Omega)z} \right. \\ &\quad \left. + \left[\tilde{\underline{\underline{\mathrm{F}}}}^{-}\right]\left[\tilde{\underline{\mathrm{B}}}^{-}(z)\right] e^{-2i(k+\pi/\Omega)z} \right\} \\ \tfrac{1}{k_0^2}\tfrac{\mathrm{d}^2}{\mathrm{d}z^2}\left[\tilde{\underline{\mathrm{B}}}^{-}(z)\right] - \tfrac{2ik}{k_0^2}\tfrac{\mathrm{d}}{\mathrm{d}z}\left[\tilde{\underline{\mathrm{B}}}^{-}(z)\right] &= \mp\delta_\epsilon \left\{ \left[\tilde{\underline{\underline{\mathrm{F}}}}^{-}\right]\left[\tilde{\underline{\mathrm{B}}}^{+}(z)\right] e^{2i(k-\pi/\Omega)z} \right. \\ &\quad \left. + \left[\tilde{\underline{\underline{\mathrm{F}}}}^{+}\right]\left[\tilde{\underline{\mathrm{B}}}^{+}(z)\right] e^{2i(k+\pi/\Omega)z} \right\} \end{aligned}\right\}. \tag{6.17}$$

In these equations, the upper signs (before δ_ϵ) apply for $0 < z < d/2$ and the lower signs for $d/2 < z < d$, while the 2×2 matrixes

$$\left[\tilde{\underline{\underline{\mathrm{F}}}}^{\pm}\right] = \frac{1}{2}\begin{bmatrix} 0 & 1 \mp h \\ 1 \pm h & 0 \end{bmatrix} \tag{6.18}$$

are anti–diagonal. Hence, the ODEs (6.17) decouple $\mathrm{B}_{\mathrm{L}}^{\pm}(z)$ from $\mathrm{B}_{\mathrm{R}}^{\pm}(z)$, but $\mathrm{B}_{\mathrm{L}}^{-}(z)$ is coupled to $\mathrm{B}_{\mathrm{L}}^{+}(z)$, and $\mathrm{B}_{\mathrm{R}}^{-}(z)$ to $\mathrm{B}_{\mathrm{R}}^{+}(z)$.

6.1.3 Transfer Matrixes

After substituting

$$\left[\tilde{\underline{\mathrm{e}}}^{\pm}(z)\right] = \left[\tilde{\underline{\mathrm{B}}}^{\pm}(z)\right] e^{\pm ikz} \tag{6.19}$$

in (6.17) and neglecting the second–order derivatives, the solutions of the ODEs (6.17) are obtained as

$$\begin{bmatrix} [\underline{\tilde{e}}^{+}(z)] \\ [\underline{\tilde{e}}^{-}(z)] \end{bmatrix} = [\underline{\underline{W}}^{+}(z-z_0)] \begin{bmatrix} [\underline{\tilde{e}}^{+}(z_0)] \\ [\underline{\tilde{e}}^{-}(z_0)] \end{bmatrix}, \quad 0^{+} \leq z_0, z \leq d/2^{-}, \tag{6.20}$$

and

$$\begin{bmatrix} [\underline{\tilde{e}}^{+}(z)] \\ [\underline{\tilde{e}}^{-}(z)] \end{bmatrix} = [\underline{\underline{W}}^{-}(z-z_0)]^{\mathrm{T}} \begin{bmatrix} [\underline{\tilde{e}}^{+}(z_0)] \\ [\underline{\tilde{e}}^{-}(z_0)] \end{bmatrix}, \quad d/2^{+} \leq z_0, z \leq d^{-}. \tag{6.21}$$

The transfer 4×4 matrixes $[\underline{\underline{W}}^{\pm}(z)]$ are defined as

$$[\underline{\underline{W}}^{\pm}(z)] = \begin{bmatrix} \mathrm{P}_{-}(z) & 0 & 0 & \pm\mathrm{Q}_{-}(z) \\ 0 & \mathrm{P}_{+}(z) & \pm\mathrm{Q}_{+}(z) & 0 \\ 0 & \pm\mathrm{Q}_{+}^{*}(z) & \mathrm{P}_{+}^{*}(z) & 0 \\ \pm\mathrm{Q}_{-}^{*}(z) & 0 & 0 & \mathrm{P}_{-}^{*}(z) \end{bmatrix}, \quad 0 \leq z \leq d/2, \tag{6.22}$$

where

$$\mathrm{P}_{\pm}(z) = e^{\pm ih\pi z/\Omega} \left[\cosh(\Delta_{\mp} z) + \frac{i(k \mp h\pi/\Omega)}{\Delta_{\mp}} \sinh(\Delta_{\mp} z) \right], \tag{6.23}$$

$$\mathrm{Q}_{\pm}(z) = e^{\pm ih\pi z/\Omega} \left[\frac{ik_{\delta}}{\Delta_{\mp}} \sinh(\Delta_{\mp} z) \right], \tag{6.24}$$

$k_{\delta} = k_0\delta_n$, $\delta_n = \delta_{\epsilon}/2\bar{n}$, and $\Delta_{\pm} = \sqrt{k_{\delta}^2 - (k \pm h\pi/\Omega)^2}$.

The structure of $[\underline{\underline{W}}^{\pm}(z)]$ confirms the decoupling of LCP and RCP phasors for all $z \in (0,\, d)$, within the approximate framework of CWT. Furthermore, it is worth mentioning that neglect of the terms containing $e^{\pm 2i(k+\pi/\Omega)z}$ in (6.17) would mean that

$$\left.\begin{aligned} &\mathrm{P}_{+}(z)\delta_{h,-1} + \mathrm{P}_{-}(z)\delta_{h,1} \Rightarrow e^{ikz} \\ &\mathrm{Q}_{+}(z)\delta_{h,-1} + \mathrm{Q}_{-}(z)\delta_{h,1} \Rightarrow 0 \end{aligned}\right\}, \tag{6.25}$$

thereby defeating the purpose of explaining the crossover phenomenon in the chiral STF. Here, $\delta_{m,m'}$ is the Kronecker delta.

6.1.4 Boundary Conditions

Expressions for $[\underline{\mathrm{E}}_{\perp}(z)]$ and $[\underline{\mathrm{H}}'_{\perp}(z)]$ are to be obtained after combining (6.20) and (6.21) with the boundary conditions on the interfaces $z = 0$, $z = d/2$, and $z = d$. The continuity of the tangential components of the electric and magnetic field phasors across these interfaces implies that $[\underline{\mathrm{E}}_{\perp}(z)]$ and $[\underline{\mathrm{H}}'_{\top}(z)] = (ik_0)^{-1}\frac{\mathrm{d}}{\mathrm{d}z}[\underline{\mathrm{E}}_{\perp}(z)]$ should be continuous, according to the ODEs (6.4).

Consistently with developments in Section 6.1.2, it is useful to define the circular counterparts of $[\underline{\mathrm{E}}_{\perp}(z)]$ and $[\underline{\mathrm{H}}'_{\top}(z)]$ as

$$\left[\underline{\tilde{\mathrm{E}}}_{\perp}(z)\right] = \left[\underline{\underline{\mathrm{Y}}}\right]^{\dagger}[\underline{\mathrm{E}}_{\perp}(z)] = \left[\underline{\tilde{\mathrm{e}}}^{+}(z)\right] + \left[\underline{\tilde{\mathrm{e}}}^{-}(z)\right] \tag{6.26}$$

and

$$\left[\underline{\tilde{\mathrm{H}}}'_{\top}(z)\right] = \left[\underline{\underline{\mathrm{Y}}}\right]^{\dagger}\left[\underline{\mathrm{H}}'_{\top}(z)\right] = (ik_0)^{-1}\left[\frac{\mathrm{d}}{\mathrm{d}z}\left[\underline{\tilde{\mathrm{e}}}^{+}(z)\right] + \frac{\mathrm{d}}{\mathrm{d}z}\left[\underline{\tilde{\mathrm{e}}}^{-}(z)\right]\right], \tag{6.27}$$

where the superscript † denotes the Hermitian adjoint [68]. These 2–column vectors must be continuous across the interfaces as well; i.e.,

$$\left.\begin{array}{l}\left[\underline{\tilde{\mathrm{E}}}_{\perp}(z^{-})\right] = \left[\underline{\tilde{\mathrm{E}}}_{\perp}(z^{+})\right] \\ \left[\underline{\tilde{\mathrm{H}}}'_{\top}(z^{-})\right] = \left[\underline{\tilde{\mathrm{H}}}'_{\top}(z^{+})\right]\end{array}\right\}, \quad z \in \{0,\, d/2,\, d\}\,. \tag{6.28}$$

In accordance with (6.20), (6.21), (6.26) and (6.27), one can obtain the expressions

$$\left[\begin{array}{c}\left[\underline{\tilde{\mathrm{E}}}_{\perp}(z)\right] \\ \left[\underline{\tilde{\mathrm{H}}}'_{\top}(z)\right]\end{array}\right] = \left[\underline{\underline{\mathrm{Z}}}^{+}\right]\left[\begin{array}{c}\left[\underline{\tilde{\mathrm{e}}}^{+}(z)\right] \\ \left[\underline{\tilde{\mathrm{e}}}^{-}(z)\right]\end{array}\right], \quad z \in \{0^{+},\, d/2^{-}\}\,, \tag{6.29}$$

and

$$\left[\begin{array}{c}\left[\underline{\tilde{\mathrm{E}}}_{\perp}(z)\right] \\ \left[\underline{\tilde{\mathrm{H}}}'_{\top}(z)\right]\end{array}\right] = \left[\underline{\underline{\mathrm{Z}}}^{-}\right]\left[\begin{array}{c}\left[\underline{\tilde{\mathrm{e}}}^{+}(z)\right] \\ \left[\underline{\tilde{\mathrm{e}}}^{-}(z)\right]\end{array}\right], \quad z \in \{d/2^{+},\, d^{-}\}\,, \tag{6.30}$$

where the 4×4 matrixes

$$\left[\underline{\underline{\mathrm{Z}}}^{\pm}\right] = \left[\underline{\underline{\mathrm{Z}}}(\bar{n})\right] \mp \delta_n \left[\begin{array}{cccc} 0 & 0 & 0 & 0 \\ 0 & 0 & 0 & 0 \\ 0 & 1 & 0 & -1 \\ 1 & 0 & -1 & 0 \end{array}\right] \tag{6.31}$$

and

$$\left[\underline{\underline{\mathrm{Z}}}(\sigma)\right] = \begin{bmatrix} \left[\underline{\underline{\mathrm{I}}}\right]_2 & \left[\underline{\underline{\mathrm{I}}}\right]_2 \\ \sigma\left[\underline{\underline{\mathrm{I}}}\right]_2 & -\sigma\left[\underline{\underline{\mathrm{I}}}\right]_2 \end{bmatrix} . \tag{6.32}$$

Parenthetically, it is noted that the approximation of $\left[\underline{\underline{\mathrm{W}}}^{\pm}(z)\right]$ *via* (6.25) must not be made for the establishment of the boundary conditions (6.29) and (6.30), which are crucial to provide an analytic expression of the crossover phenomenon.

The values of the field phasors at $z = 0^-$ and $z = d^+$ should be related to the electromagnetic field in the two half–spaces. The incident, reflected and transmitted plane waves propagate along the z axis in the two half–spaces $z \leq 0$ and $z \geq d$. Following Venugopal and Lakhtakia [27, 28], and in analogy with (6.19) and (6.26), the electric field phasors in the two half–spaces are represented as

$$\left.\begin{aligned} \left[\tilde{\underline{\mathrm{E}}}_{\perp}(z)\right] &= [\,\underline{\mathcal{A}}\,]\, e^{in_{hs}k_0 z} + [\,\underline{\mathcal{R}}\,]\, e^{-in_{hs}k_0 z}\,, \; z \leq 0^- \\ \left[\tilde{\underline{\mathrm{E}}}_{\perp}(z)\right] &= [\,\underline{\mathcal{T}}\,]\, e^{in_{hs}k_0 z}\,, \qquad\qquad z \geq d^+ \end{aligned}\right\} , \tag{6.33}$$

where the 2–column vectors

$$[\,\underline{\mathcal{A}}\,] = \begin{bmatrix} a_{\mathrm{L}} \\ a_{\mathrm{R}} \end{bmatrix} , \quad [\,\underline{\mathcal{R}}\,] = \begin{bmatrix} r_{\mathrm{R}} \\ r_{\mathrm{L}} \end{bmatrix} , \quad [\,\underline{\mathcal{T}}\,] = \begin{bmatrix} t_{\mathrm{L}} \\ t_{\mathrm{R}} \end{bmatrix} , \tag{6.34}$$

respectively, comprise amplitudes of the LCP and RCP components of the incident, reflected, and transmitted plane waves. Finally, similarly to (6.29) and (6.30), the expressions

$$\begin{bmatrix} \left[\tilde{\underline{\mathrm{E}}}_{\perp}(z)\right] \\ \left[\tilde{\underline{\mathrm{H}}}'_{\top}(z)\right] \end{bmatrix} = \left[\underline{\underline{\mathrm{Z}}}_{hs}\right] \begin{bmatrix} [\,\underline{\mathcal{A}}\,] \\ [\,\underline{\mathcal{R}}\,] \end{bmatrix} , \quad z = 0^- , \tag{6.35}$$

and

$$\begin{bmatrix} \left[\tilde{\underline{\mathrm{E}}}_{\perp}(z)\right] \\ \left[\tilde{\underline{\mathrm{H}}}'_{\top}(z)\right] \end{bmatrix} = \left[\underline{\underline{\mathrm{Z}}}_{hs}\right] \begin{bmatrix} [\,\underline{\mathcal{T}}\,] \\ [\underline{0}]_2 \end{bmatrix} , \quad z = d^+ \tag{6.36}$$

are obtained, where $\left[\underline{\underline{\mathrm{Z}}}_{hs}\right] = \left[\underline{\underline{\mathrm{Z}}}(n_{hs})\right]$.

6.1.5 Reflection and Transmission

By combining the equalities (6.20), (6.21), (6.29), (6.30), (6.35) and (6.36) with the boundary conditions (6.28), the unknown $[\underline{\mathcal{R}}]$ and $[\underline{\mathcal{T}}]$ are determined by the algebraic equation

$$\begin{bmatrix} [\underline{\mathcal{T}}] \\ [\underline{0}]_2 \end{bmatrix} = \left[\underline{\underline{\tau}}\right] \begin{bmatrix} [\underline{\mathcal{A}}] \\ [\underline{\mathcal{R}}] \end{bmatrix} , \tag{6.37}$$

where the 4×4 transmission matrix

$$\left[\underline{\underline{\tau}}\right] = \left[\underline{\underline{Z}}_{hs}\right]^{-1} \left[\underline{\underline{Z}}^{-}\right] \left[\hat{\underline{\underline{\tau}}}\right] \left[\underline{\underline{Z}}^{+}\right]^{-1} \left[\underline{\underline{Z}}_{hs}\right] \tag{6.38}$$

employs the matrix

$$\left[\hat{\underline{\underline{\tau}}}\right] = \left[\underline{\underline{W}}^{-}(d/2)\right] \left[\underline{\underline{Z}}^{-}\right]^{-1} \left[\underline{\underline{Z}}^{+}\right] \left[\underline{\underline{W}}^{+}(d/2)\right] \tag{6.39}$$

which does not depend on n_{hs}. The transmission matrix $\left[\hat{\underline{\underline{\tau}}}\right]$ of (6.39), through specified here for the central 90°–twist defect, applies in a general sense for any ϕ.

In fact, because of structural chirality, $\left[\underline{\underline{W}}^{-}(d/2)\right]$ is related to $\left[\underline{\underline{W}}^{+}(d/2)\right]$, and $\left[\underline{\underline{Z}}^{-}\right]$ to $\left[\underline{\underline{Z}}^{+}\right]$, by a rotational transformation:

$$\left.\begin{aligned} \left[\underline{\underline{W}}^{-}(d/2)\right] &= \left[\underline{\underline{\mathfrak{R}}}(\phi)\right] \left[\underline{\underline{W}}^{+}(d/2)\right] \left[\underline{\underline{\mathfrak{R}}}(\phi)\right]^{-1} \\ \left[\underline{\underline{Z}}^{-}\right] &= \left[\underline{\underline{\mathfrak{R}}}(\phi)\right] \left[\underline{\underline{Z}}^{+}\right] \left[\underline{\underline{\mathfrak{R}}}(\phi)\right]^{-1} \end{aligned}\right\} . \tag{6.40}$$

The 4×4 rotational matrix $\left[\underline{\underline{\mathfrak{R}}}(\phi)\right]$ consists of two diagonal blocks as follows:

$$\left[\underline{\underline{\mathfrak{R}}}(\phi)\right] = \begin{bmatrix} \left[\underline{\underline{Y}}\right]^{\dagger} \left[\underline{\underline{R}}(\phi)\right] \left[\underline{\underline{Y}}\right] & \left[\underline{0}\right]_2 \\ \left[\underline{0}\right]_2 & \left[\underline{\underline{Y}}\right]^{\dagger} \left[\underline{\underline{R}}(\phi)\right] \left[\underline{\underline{Y}}\right] \end{bmatrix} . \tag{6.41}$$

The 2×2 matrix

$$\left[\underline{\underline{R}}(\phi)\right] = \begin{bmatrix} \cos\phi & -\sin\phi \\ \sin\phi & \cos\phi \end{bmatrix} \tag{6.42}$$

denotes a rotation about the z axis by an angle ϕ. When $\phi = m\pi$, $(m \in \mathbb{Z})$, the matrix $\left[\underline{\underline{\mathfrak{R}}}(\phi)\right] = \left[\underline{\underline{I}}\right]_4$; therefore, (6.40) simplifies to

$$\left[\underline{\underline{W}}^{-}(d/2)\right] = \left[\underline{\underline{W}}^{+}(d/2)\right] , \quad \left[\underline{\underline{Z}}^{-}\right] = \left[\underline{\underline{Z}}^{+}\right] . \tag{6.43}$$

As a result, the transmission matrix

$$\left[\underline{\underline{\hat{\tau}}}\right] = \left[\underline{\underline{\mathrm{W}}}^{+}(d/2)\right]^2 = \left[\underline{\underline{\mathrm{W}}}^{+}(d)\right] \,, \tag{6.44}$$

which applies to a defect–free chiral STF. When $\phi \neq m\pi$, $\left[\underline{\underline{\mathrm{W}}}^{-}(d/2)\right] \neq \left[\underline{\underline{\mathrm{W}}}^{+}(d/2)\right]$ in general, which gives rise to the spectral characteristics of $\left[\underline{\underline{\hat{\tau}}}\right]$ responsible for the crossover phenomenon.

Although the transmission matrix $\left[\underline{\underline{\tau}}\right]$ seems very complicated, its replacement by $\left[\underline{\underline{\hat{\tau}}}\right]$ in (6.37) is found to generate values of $[\underline{\mathcal{R}}]$ and $[\underline{\mathcal{T}}]$ that exhibit the main spectral features of the circular Bragg phenomenon as well those due to the central twist defect. In physical terms, the replacement of $\left[\underline{\underline{\tau}}\right]$ by $\left[\underline{\underline{\hat{\tau}}}\right]$ for obtaining $[\underline{\mathcal{R}}]$ and $[\underline{\mathcal{T}}]$ amounts to ignoring the index–mismatch across the interfaces $z = 0$ and $z = d$. Indeed, when $|\delta_n| << \bar{n}$ and $n_{hs} = \bar{n}$, the chiral STF can be said to be index–matched to the medium in the two half–spaces, and $\left[\underline{\underline{\tau}}\right] \simeq \left[\underline{\underline{\hat{\tau}}}\right]$ would then be very true.

To analyze the crossover phenomenon, let $n_r = \bar{n}$ to minimize the index–mismatch across the interfaces $z = 0$ and $z = d$. Then,

$$\begin{bmatrix} [\underline{\mathcal{T}}] \\ [\underline{0}]_2 \end{bmatrix} = \left[\underline{\underline{\hat{\tau}}}\right] \begin{bmatrix} [\underline{\mathcal{A}}] \\ [\underline{\mathcal{R}}] \end{bmatrix} \tag{6.45}$$

yields approximate but closed–form solutions for $[\underline{\mathcal{R}}]$ and $[\underline{\mathcal{T}}]$ as follows.

The reflection coefficients (r_{LL}, etc.) and the transmission coefficients (t_{LL}, etc.) are defined through the matrix expressions

$$\begin{bmatrix} r_{\mathrm{L}} \\ r_{\mathrm{R}} \end{bmatrix} = \begin{bmatrix} r_{\mathrm{LL}} & r_{\mathrm{RL}} \\ r_{\mathrm{LR}} & r_{\mathrm{RR}} \end{bmatrix} \begin{bmatrix} a_{\mathrm{L}} \\ a_{\mathrm{R}} \end{bmatrix} \,, \quad \begin{bmatrix} t_{\mathrm{L}} \\ t_{\mathrm{R}} \end{bmatrix} = \begin{bmatrix} t_{\mathrm{LL}} & t_{\mathrm{RL}} \\ t_{\mathrm{LR}} & t_{\mathrm{RR}} \end{bmatrix} \begin{bmatrix} a_{\mathrm{L}} \\ a_{\mathrm{R}} \end{bmatrix} \,. \tag{6.46}$$

Reflectances and transmittances are defined as

$$\mathrm{R}_{\sigma\sigma'} = |r_{\sigma\sigma'}|^2 \,, \quad \mathrm{T}_{\sigma\sigma'} = |t_{\sigma\sigma'}|^2 \,, \quad \sigma, \sigma' = \mathrm{L}, \mathrm{R} \,. \tag{6.47}$$

The coefficients and remittances defined by (6.46) and (6.47) are equivalent to those defined by (3.5) and (3.6) for the special case $\alpha = 0$.

Because the crossover phenomenon involves only the co–polarized quantities, closed–form expressions of the cross–polarized reflection and transmission coefficients are not of interest. On neglecting the small item $\hat{\mathrm{Q}}_-$ in $\left[\underline{\underline{\mathrm{W}}}^{\pm}(d/2)\right]$ for $|b| << 1$, the solution of (6.45) results in the co–polarized transmission coefficients

$$\left.\begin{aligned} t_{\mathrm{LL}} &= \frac{\hat{\mathrm{P}}_-^2\,\hat{\mathcal{G}}}{\hat{\mathcal{G}}+b^2\hat{\mathrm{Q}}_+^2}\delta_{h,1} + \frac{\left(|\hat{\mathrm{P}}_+|^2-|\hat{\mathrm{Q}}_+|^2\right)^2}{\hat{\mathcal{G}}+b^2\hat{\mathrm{Q}}_+^2}\delta_{h,-1} \\ t_{\mathrm{RR}} &= \frac{\hat{\mathrm{P}}_-^2\,\hat{\mathcal{G}}}{\hat{\mathcal{G}}+b^2\hat{\mathrm{Q}}_+^2}\delta_{h,-1} + \frac{\left(|\hat{\mathrm{P}}_+|^2-|\hat{\mathrm{Q}}_+|^2\right)^2}{\hat{\mathcal{G}}+b^2\hat{\mathrm{Q}}_+^2}\delta_{h,1} \end{aligned}\right\}, \tag{6.48}$$

and the co–polarized reflection coefficients

$$\left.\begin{aligned} r_{\mathrm{LL}} &= -\frac{\hat{\mathrm{P}}_-}{\hat{\mathrm{P}}_-^*}\left(\frac{b\hat{\mathcal{G}}-b^2\hat{\mathrm{P}}_+^*\hat{\mathrm{Q}}_+}{\hat{\mathcal{G}}+b^2\hat{\mathrm{Q}}_+^2}\right)\delta_{h,1} - \frac{2\,\mathrm{Re}\left[\hat{\mathrm{P}}_+\hat{\mathrm{Q}}_+\right]+b\left(|\hat{\mathrm{P}}_+|^2+|\hat{\mathrm{Q}}_+|^2\right)+b^2\hat{\mathrm{P}}_+\hat{\mathrm{Q}}_+}{\hat{\mathcal{G}}+b^2\hat{\mathrm{Q}}_+^2}\delta_{h,-1} \\ r_{\mathrm{RR}} &= -\frac{\hat{\mathrm{P}}_-}{\hat{\mathrm{P}}_-^*}\left(\frac{b\hat{\mathcal{G}}-b^2\hat{\mathrm{P}}_+^*\hat{\mathrm{Q}}_+}{\hat{\mathcal{G}}+b^2\hat{\mathrm{Q}}_+^2}\right)\delta_{h,-1} - \frac{2\,\mathrm{Re}\left[\hat{\mathrm{P}}_+\hat{\mathrm{Q}}_+\right]+b\left(|\hat{\mathrm{P}}_+|^2+|\hat{\mathrm{Q}}_+|^2\right)+b^2\hat{\mathrm{P}}_+\hat{\mathrm{Q}}_+}{\hat{\mathcal{G}}+b^2\hat{\mathrm{Q}}_+^2}\delta_{h,1} \end{aligned}\right\}, \tag{6.49}$$

where

$$\left.\begin{aligned} \hat{\mathcal{G}} &= (\hat{\mathrm{P}}_+^*)^2 + 2b\hat{\mathrm{P}}_+^*\hat{\mathrm{Q}}_+ + \hat{\mathrm{Q}}_+^2 \\ \hat{\mathrm{P}}_\pm &= \mathrm{P}_\mp(d/2)\delta_{h,-1} + \mathrm{P}_\pm(d/2)\delta_{h,1} \\ \hat{\mathrm{Q}}_\pm &= \mathrm{Q}_\mp(d/2)\delta_{h,-1} + \mathrm{Q}_\pm(d/2)\delta_{h,1} \end{aligned}\right\}. \tag{6.50}$$

All the results presented in Section 6.2 for the chiral STF with a central 90°–twist defect are obtained from (6.48) and (6.49), unless otherwise noted.

6.2 Solution and Analysis

6.2.1 Circular Bragg Phenomenon

For phenomenological completeness, it is desirable to begin with the optical response of a chiral STF *without* a twist defect. For simplicity, but without loss of essential physics, let dispersion be ignored. In the absence of the twist defect, the transmission matrix $\left[\underline{\underline{\hat{\tau}}}\right]$ is given in (6.44).

Figure 6.2 shows the reflectances and transmittances for $\lambda_0 \in [640, 740]$ nm, when $\epsilon_c = 1.7029^2$, $\epsilon_d = 1.7427^2$, $n_{hs} = \bar{n} = 1.7230$, $h = 1$, $\Omega = 200$ nm, and $\mathrm{N}_d = d/\Omega = 100$.

The circular Bragg phenomenon is indicated by a peak in $\mathrm{R_{RR}}$ and a trough in $\mathrm{T_{RR}}$, because the chosen chiral STF is structurally right–handed. The incident LCP plane wave is mostly transmitted. According to CWT, the Bragg regime is centered at the wavelength [30]

$$\lambda_{0_{\mathrm{CWT}}}^{\mathrm{Br}} = 2\bar{n}\Omega\,. \tag{6.51}$$

From numerous computations, it was ascertained that substantial development of circular Bragg phenomenon requires

$$\mathrm{N}_d \geq 1/|b|\,, \tag{6.52}$$

where $b = \delta_n/\bar{n}$ is the relative local birefringence.

The emergence of the circular Bragg phenomenon can be analytically explained by the characteristics of $\left[\underline{\underline{\mathrm{W}}}^{+}(z)\right]$. This 4×4 matrix can be decomposed into the following 2×2 submatrixes:

$$\left[\underline{\underline{\mathrm{W}}}_{\mathrm{L}}^{+}(z)\right] = \begin{bmatrix} \mathrm{P}_{-}(z) & \mathrm{Q}_{-}(z) \\ \mathrm{Q}_{-}^{*}(z) & \mathrm{P}_{-}^{*}(z) \end{bmatrix}, \quad \left[\underline{\underline{\mathrm{W}}}_{\mathrm{R}}^{+}(z)\right] = \begin{bmatrix} \mathrm{P}_{+}(z) & \mathrm{Q}_{+}(z) \\ \mathrm{Q}_{+}^{*}(z) & \mathrm{P}_{+}^{*}(z) \end{bmatrix}. \tag{6.53}$$

These two submatrixes control the responses of the chiral STF to incident LCP and RCP plane waves, respectively. For $|b| << 1$, $|\mathrm{Q}_{\mp}(z)|$ is much smaller than $|\mathrm{P}_{\mp}(z)|$ ($\simeq 1$) for $h = \pm 1$. Therefore, $\left[\underline{\underline{\mathrm{W}}}_{\mathrm{R}}^{+}(z)\right]\delta_{h,-1} + \left[\underline{\underline{\mathrm{W}}}_{\mathrm{L}}^{+}(z)\right]\delta_{h,1}$ is approximately equal to $\left[\underline{\underline{\mathrm{I}}}\right]_2$ for $\lambda_0 \sim \lambda_{0_{\mathrm{CWT}}}^{\mathrm{Br}}$, which leads to the total transmission of the incident cross–handed CP plane wave in the Bragg regime. In other words, a chiral STF acts as a homogenous, isotropic, dielectric medium for a normally incident, cross–handed, CP plane wave. However, the format of $\left[\underline{\underline{\mathrm{W}}}_{\mathrm{L}}^{+}(z)\right]\delta_{h,-1} + \left[\underline{\underline{\mathrm{W}}}_{\mathrm{R}}^{+}(z)\right]\delta_{h,1}$ resembles the scattering matrix of a scalar Bragg grating [79]. Accordingly, the response to a co–handed CP plane wave is the same as of a scalar Bragg grating, for wavelengths within the Bragg regime [31].

6.2.2 Crossover Phenomenon

Now, the optical response of a chiral STF with a central 90°–twist defect is considered. Figures 6.3 and 6.4 show the spectrums of the co–polarized reflectances and transmittances obtained from the CWT expressions (6.48) and (6.49), when $\mathrm{N}_d = 100$ and $\mathrm{N}_d = 600$, respectively. As expected, the CWT captures the already–known phenomenons that

- a co–handed reflectance hole, accompanied by a co–handed transmittance peak, occurs in the center of the Bragg regime for relatively small N_d (Figure 6.3), disappearing for large N_d; and
- a cross–handed transmittance hole, accompanied by a cross–handed reflectance peak, occurs in the center of the Bragg regime for large N_d (Figure 6.4).

Typically, the bandwidth of the cross–handed transmittance hole is extraordinarily small, and is independent of N_d beyond its crossover value N_d^{co}.

In order to analyze the consequences of introducing the central 90°–twist defect, recourse to the matrix $\big[\underline{\underline{\hat{\tau}}}\big]$ must be taken. This matrix can be decomposed as

$$\big[\underline{\underline{\hat{\tau}}}\big] = \big[\underline{\underline{\mathrm{W}}}^{-}(d/2)\big]\,\big[\underline{\underline{\mathrm{W}}}^{+}(d/2)\big] + \big[\underline{\underline{\mathrm{W}}}^{-}(d/2)\big]\,\big[\underline{\underline{\Theta}}(b)\big]\,\big[\underline{\underline{\mathrm{W}}}^{+}(d/2)\big]\ , \tag{6.54}$$

where all nonzero entries of the 4×4 matrix

$$\big[\underline{\underline{\Theta}}(b)\big] = \big[\underline{\underline{\mathrm{Z}}}^{-}\big]^{-1}\,\big[\underline{\underline{\mathrm{Z}}}^{+}\big] - \big[\underline{\underline{\mathrm{I}}}\big]_4 \tag{6.55}$$

are of $\mathcal{O}(b)$. This decomposition is not arbitrary but has physical meaning. The first term on the right side of (6.54), all by itself, would give rise to total transmission in the central part of the Bragg regime. In contrast, were $\big[\underline{\underline{\hat{\tau}}}\big] = \big[\underline{\underline{\mathrm{W}}}^{-}(d/2)\big]\,\big[\underline{\underline{\Theta}}(b)\big]\,\big[\underline{\underline{\mathrm{W}}}^{+}(d/2)\big]$, total reflection would occur in the entire Bragg regime, for all $\mathrm{N}_d \geq 1/|b|$. Thus, the second term on the right side of (6.54) describes a CP mirror.

As $|b| << 1$, the second term on the right side of (6.54) may be viewed as perturbing the leading term $\left[\underline{\underline{\mathrm{W}}}^{-}(d/2)\right]\left[\underline{\underline{\mathrm{W}}}^{+}(d/2)\right]$. Even so, the former is essential to the elucidation of the crossover phenomenon. For convenience, the weight of the second term in relation to the first term is defined

$$\alpha_\infty = \frac{\| \left[\underline{\underline{\mathrm{W}}}^{-}(d/2)\right]\left[\underline{\underline{\Theta}}(b)\right]\left[\underline{\underline{\mathrm{W}}}^{+}(d/2)\right] \|_\infty}{\| \left[\underline{\underline{\mathrm{W}}}^{-}(d/2)\right]\left[\underline{\underline{\mathrm{W}}}^{+}(d/2)\right] \|_\infty} = \frac{|b|}{1-b^2}\frac{|\hat{\mathrm{P}}_+|^2 + |\hat{\mathrm{Q}}_+|^2}{|\hat{\mathrm{P}}_+^2 + (\hat{\mathrm{Q}}_+^*)^2|}\,, \tag{6.56}$$

where $||\,.\,||$ is the L_∞–norm of matrix [68]. According to (6.50),

$$\alpha_\infty \approx \begin{cases} |b|\,, & \text{for } |b\sinh(\pi b \mathrm{N}_d)| << 1\,, \\ \\ |b/\beta|\,, & \text{for } |b\sinh(\pi b \mathrm{N}_d)| >> 1\,, \end{cases} \tag{6.57}$$

where $\beta = (k - \pi/\Omega)/k_\delta$. Clearly, α_∞ is independent of N_d in either of the N_d–ranges specified in (6.57); therefore, both terms on the right side of (6.54) are similar to each other in the sense of L_∞ norms in those two N_d–ranges. Furthermore, a wavelength–regime can be mapped to a β–regime uniquely. When $\beta = 0$, $\lambda_0 = \lambda_{0_{\mathrm{CWT}}}^{\mathrm{Br}}$; therefore, the neighborhood of $\lambda_{0_{\mathrm{CWT}}}^{\mathrm{Br}}$ can be equivalently specified through the β–neighborhood of 0.

When N_d is relatively small (but larger than $1/|b|$), $||\left[\underline{\underline{\mathrm{W}}}^{\pm}(d/2)\right]||_\infty = \mathcal{O}(1)$ and $\alpha_\infty \approx |b| << 1$; thus, the second term on the right side of (6.54) can be ignored in favor of the first term, so that $\left[\underline{\underline{\hat{\tau}}}\right] \approx \left[\underline{\underline{\mathrm{W}}}^{-}(d/2)\right]\left[\underline{\underline{\mathrm{W}}}^{+}(d/2)\right]$. According to (6.23) and (6.24), $\left[\underline{\underline{\mathrm{W}}}^{-}(d/2)\right]\left[\underline{\underline{\mathrm{W}}}^{+}(d/2)\right]$ becomes almost equal to $\left[\underline{\underline{\mathrm{I}}}\right]_4$ for $\lambda_0 \sim \lambda_{0_{\mathrm{CWT}}}^{\mathrm{Br}}$, which gives rises to almost total transmission in the center of Bragg regime, as confirmed by Figure 6.3(b) for $\mathrm{N}_d = 100$. In other words, the chiral STF with the central 90°–twist defect becomes optically transparent in a small neighborhood of $\lambda_{0_{\mathrm{CWT}}}^{\mathrm{Br}}$, for both LCP and RCP plane waves. Another interpretation is that the phase difference between the field phasors at $z = 0^+$ and $z = d/2^-$ is exactly the opposite of the phase difference between the field phasors at $z = d/2^+$ and $z = d^-$.

When N_d is significantly large, the foregoing picture changes completely. No longer can $\left[\underline{\underline{\hat{\tau}}}\right]$ be considered approximately equal to $\left[\underline{\underline{\mathrm{W}}}^{-}(d/2)\right]\left[\underline{\underline{\mathrm{W}}}^{+}(d/2)\right]$, because $\alpha_\infty \approx |b/\beta| \to +\infty$ as $\lambda_0 \to \lambda_{0_{\mathrm{CWT}}}^{\mathrm{Br}}$. The first term on the right side of (6.54) is still almost equal to $\left[\underline{\underline{\mathrm{I}}}\right]_4$

at $\lambda_0 = \lambda^{\rm Br}_{0_{\rm CWT}}$ — and therefore indicates total transmission all by itself in the central part of the Bragg regime — although the bandwidth of that feature falls exponentially as N_d increases. But, the second term interferes with the first term in the neighborhood of $\lambda^{\rm Br}_{0_{\rm CWT}}$ so that $\left[\underline{\underline{\hat{\tau}}}\right]$ is isomorphic to the transmittance matrix of a defect–free chiral STF — except in a tiny neighborhood of $\beta = b$ wherein $\alpha_\infty \approx 1$. *It must be the L_∞–norm–equivalence of the two terms that engenders the total–reflection feature in the tiny neighborhood of $\beta = b$*, as confirmed by Figure 6.4(a) for $\mathrm{N}_d = 600$. This conclusion applies to any arbitrary $\phi \neq m\pi$, $(m \in \mathbb{Z})$, as proved by further investigations.

An analytical view of the crossover phenomenon is attained by examining the CWT expressions (6.48) and (6.49) when $\beta = b$. Now, $\hat{\mathcal{G}} \equiv 1$ for any N_d, when $\beta = b$ or λ_0 equals

$$\lambda^{p}_{0_{\rm CWT}} = \lambda^{\rm Br}_{0_{\rm CWT}}(1 - b^2)\,. \tag{6.58}$$

Furthermore, $|\hat{\mathrm{P}}_-|^2 = 1 + \mathcal{O}(b^2)$ and

$$\mathrm{Det}\left\{\left[\underline{\underline{\mathrm{W}}}^{+}_{\mathrm{L}}(d/2)\right]\delta_{h,-1} + \left[\underline{\underline{\mathrm{W}}}^{+}_{\mathrm{R}}(d/2)\right]\delta_{h,1}\right\} = |\hat{\mathrm{P}}_+|^2 - |\hat{\mathrm{Q}}_+|^2 \equiv 1 \tag{6.59}$$

for any N_d. Hence, the values of $t_{\rm LL}$ and $t_{\rm RR}$ in (6.48) are generally determined by the denominator $\hat{\mathcal{G}} + b^2\hat{\mathrm{Q}}^2_+$. Typically, when N_d is not significantly large so that

$$b^2\hat{\mathrm{Q}}^2_+ \approx -\frac{b^2}{1-b^2}\sinh^2(\pi b \mathrm{N}_d) \tag{6.60}$$

is of $o(1)$ for $\lambda_0 = \lambda^{p}_{0_{\rm CWT}}$, then $\hat{\mathcal{G}} + b^2\hat{\mathrm{Q}}^2_+ \approx 1$. Hence, $\mathrm{T}_{\rm LL} \to 1$ and $\mathrm{T}_{\rm RR} \to 1$, as $\lambda_0 \to \lambda^{p}_{0_{\rm CWT}}$. Correspondingly, total transmission (and thereby the co–handed reflection hole) occurs near $\lambda^{p}_{0_{\rm CWT}}$ for small values of $\mathrm{N}_d \geq 1/|b|$.

However, as N_d increases, the value of $|b^2\hat{\mathrm{Q}}^2_+|$ increases exponentially to exceed $\hat{\mathcal{G}} = 1$ tremendously at $\lambda_0 = \lambda^{p}_{0_{\rm CWT}}$. Therefore, $\mathrm{T}_{\rm LL} \to 0$ and $\mathrm{T}_{\rm RR} \to 0$ for significantly large N_d at $\lambda_0 = \lambda^{p}_{0_{\rm CWT}}$, leading to the disappearance of total transmission in the center of the Bragg regime. Instead, (6.49) implies that $\mathrm{R}_{\rm LL} \to 1$ and $\mathrm{R}_{\rm RR} \to 1$ at $\lambda_0 = \lambda^{p}_{0_{\rm CWT}}$ for $\mathrm{N}_d \to +\infty$, thereby confirming the emergence of total reflection (and thereby the cross–handed transmittance hole) for large values of $\mathrm{N}_d \geq 1/|b|$.

Although the foregoing analysis successfully provides a rigorous explanation of the crossover phenomenon for either small or significantly large values of N_d, it is not able to yield an estimate of N_d^{co}. In fact, when N_d is close to N_d^{co}, the denominator $\hat{\mathcal{G}} + b^2\hat{\mathrm{Q}}_+^2$ in (6.48) and (6.49) becomes almost null–valued for $\lambda_0 = \lambda_{0_{\mathrm{CWT}}}^p$. Therefore, (6.48) and (6.49) are not reliable as far as adherence to the principle of conservation of energy is considered. The reason for this inadequacy is the neglect of the second–order derivatives in the coupled–wave ODEs (6.17).

Parenthetically, although the electromagnetic field in axially excited defect–free chiral STFs can be expressed exactly [80, 81] and has been used for chiral STFs with central twist defects [58], closed–form expressions of the reflectances and transmittances of chiral STFs with central 90°–twist defects are presented here for the first time. These expressions may be used to calculate the peak wavelength and bandwidth when N_d is sufficiently different from N_d^{co}.

6.2.3 Hole/Peak Locations and Bandwidths

Figure 6.5 provides a comparison of the co–handed transmittance and the cross–handed reflectance obtained using the CWT equation (6.49) with those obtained from the numerical solution procedure devised in Chapter 5 for $\alpha = 0$. Clearly, Figure 6.5(a) illustrates that the CWT agrees with the numerical solution procedure in modeling the co–handed transmittance peak (and thereby the co–handed reflectance hole) on a relatively coarse wavelength–scale for small values of $\mathrm{N}_d \geq 1/|b|$. However, on a highly refined wavelength–scale, the locations of the cross–handed reflectance peak (as well as the cross–handed transmittance hole) for large values of N_d are predicted differently by the CWT and the numerical solution procedure, as illustrated in Figure 6.5(b).

In fact, according to the numerical solution of (5.15), both types of spectral holes and

peaks are centered at

$$\lambda_0^p = \lambda_{0_{\mathrm{CWT}}}^{\mathrm{Br}}(1 - 0.5b^2)\,. \tag{6.61}$$

When compared with λ_0^{Br} of (4.1), it is found that $\lambda_0^p = \lambda_0^{\mathrm{Br}}$ correct to order $\mathcal{O}(b^4)$. The deviation of $\lambda_{0_{\mathrm{CWT}}}^p$ of (6.58) from λ_0^p echoes the approximation inherent in the CWT.

Figure 6.6 provides an assessment of the bandwidths of both types of spectral holes in relation to the local birefringence. The bandwidth of the co–handed reflectance hole decreases exponentially with N_d. This is because the factor $b^2\hat{\mathrm{Q}}_+^2$ in (6.48) increases exponentially with N_d, as per (6.60). The bandwidth of the cross–handed transmittance hole, although saturated for $\mathrm{N}_d > \mathrm{N}_d^{co}$, increases exponentially with $|b|$, as shown in Figure 6.6(b). In comparison, Figure 6.6(a) illustrates that the b–dependence of the bandwidth of the co–handed reflectance hole is linear for $\mathrm{N}_d = 1/|b|$.

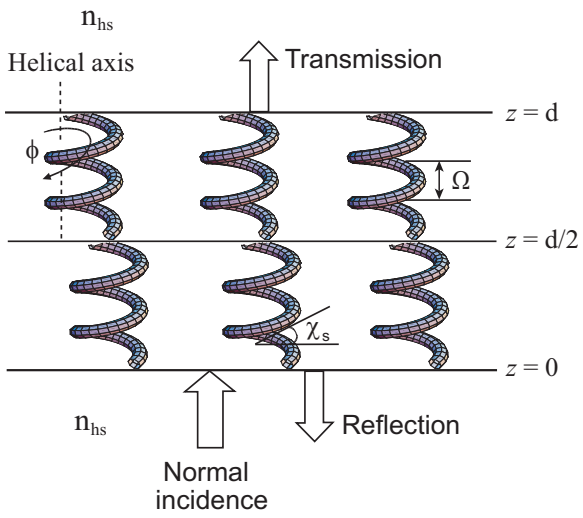

Figure 6.1: Schematic of the boundary value problem involving axial propagation of electromagnetic wave in a chiral STF with a central twist defect of $\phi \neq m\pi$ ($m \in \mathbb{Z}$) introduced between the upper and the lower halves about the helical axis.

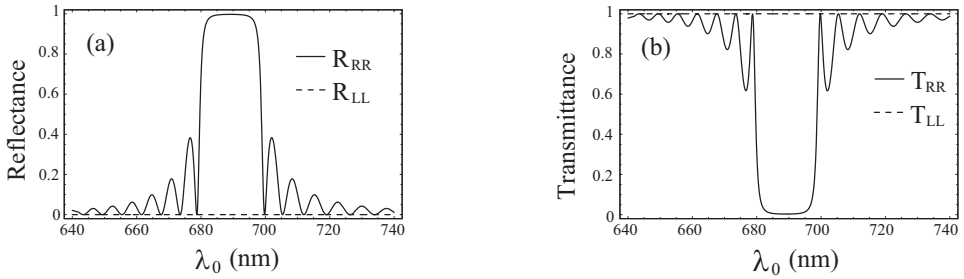

Figure 6.2: (a) Reflectances and (b) transmittances of a structurally right–handed chiral STF without the central twist defect, for normal incidence. The following parameters were used for CWT calculations: $\epsilon_c = 1.7029^2$, $\epsilon_d = 1.7429^2$, $n_r = \bar{n} = 1.7230$, $h = 1$, $\Omega = 200$ nm and $\mathrm{N}_d = 100$. Interchange the subscripts $_{\mathrm{L}}$ and $_{\mathrm{R}}$ for $h = -1$.

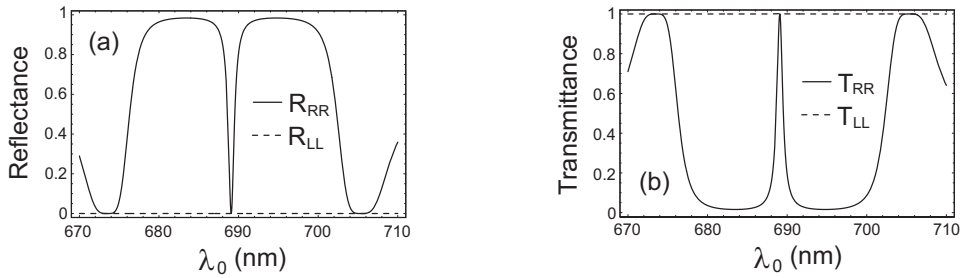

Figure 6.3: (a) Reflectances R_{LL} and R_{RR} and (b) transmittances T_{LL} and T_{RR}, computed for a structurally right–handed chiral STF with a central 90°–twist defect. While $N_d = 100$, other parameters are the same as for Figure 6.2. A co–handed reflectance hole and a co–handed transmittance peak must be noted.

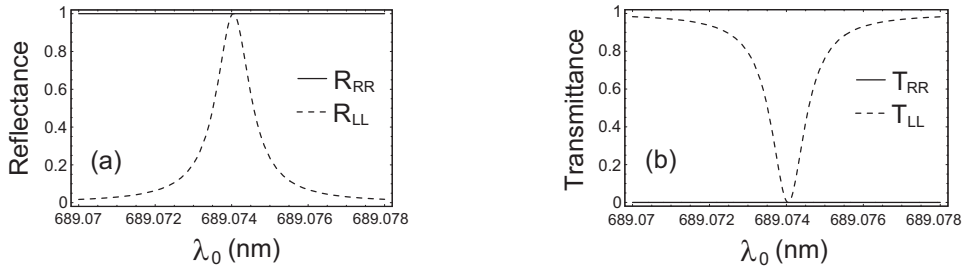

Figure 6.4: Same as Figure 6.3, but for $N_d = 600$. A cross–handed transmittance hole and a cross–handed reflectance peak must be noted.

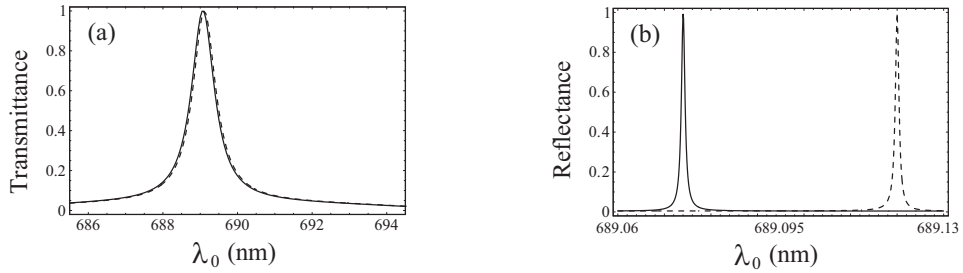

Figure 6.5: (a) Co–handed transmittance T_{RR} for $N_d = 100$ and (b) cross–handed reflectance R_{LL} for $N_d = 600$. Other parameters are the same as for Figure 6.3. Data for the solid lines were computed using CWT expressions (6.48) and (6.49), while the dashed lines are due to the numerical solution of (5.15) for $\alpha = 0$.

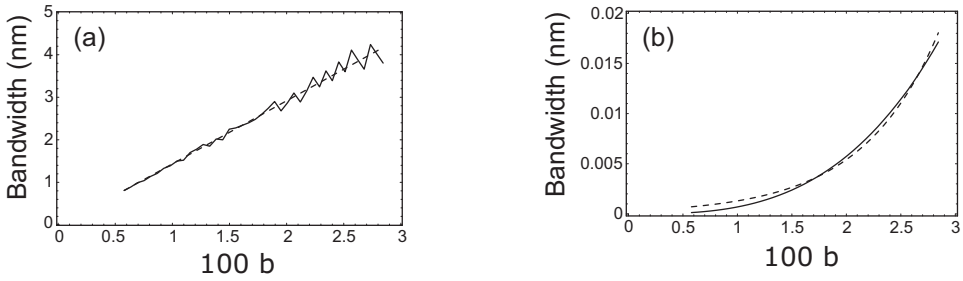

Figure 6.6: Bandwidths of (a) co–handed reflectance hole for $N_d = 1/b$ and (b) cross–handed transmittance hole for $N_d = 2(\pi b)^{-1}\ell n(8/b)$ (significantly large), as functions of $b > 0$. Data for the solid lines were computed using (6.48) and (6.49), while the dashed lines are fitted to solid lines by (a) a linear function and (b) an exponential function. See Figure 6.3 for other parameters.

Chapter 7

Lateral Shifts of Optical Beam on Reflection by Slanted Chiral STFs[‡]

In addition to planewave excitation discussed in Chapters 3–6, finite sources of excitation (e.g., evanescent waves, nonparaxial optical beams, and point dipoles) are widely exploited in nano–optics. Due to the interaction between the circular Bragg phenomenon and the Rayleigh–Wood anomaly, practical applications of slanted chiral STFs are likely to involve optical beams which are either continuous–wave or pulsed. Therefore, the objective of this chapter is to present the response of slanted chiral STFs to optical beams, with emphasis on lateral shifts of optical beams on reflection.

7.1 Angular–spectrum Representation of 3D Optical Beams

Let a slanted chiral STF of thickness d occupying the region $0 < z < d$, while two half–spaces $z \leq 0$ and $z \geq d$ filled with a homogeneous and isotropic medium of refractive index

[‡] This chapter is partly adapted from the following paper: F. Wang, A. Lakhtakia, "Lateral shifts of optical beams on reflection by slanted chiral sculptured thin films", Opt. Commun. **235** 107–132 (2004).

n_{hs}, as shown in Figure 7.1. A 3D optical beam is incident from the half–space $z \leq 0$ on to the plane $z = 0$. As a result, reflection and transmission of the optical beam into the two half–spaces occur.

The incidence geometry of the 3D optical beam is described as follows: Let $\theta_i^b \in (-\pi/2, \pi/2)$ and $\psi_i^b \in [0, \pi)$, respectively, be the mean angles of beam incidence with respect to the z axis and the x axis in the xy plane. The introduction of θ_i^b and ψ_i^b helps define the cartesian coordinates $(\bar{x}, \bar{y}, \bar{z})$, where

$$\left.\begin{aligned} \bar{x} &= x\cos\theta_i^b\cos\psi_i^b + y\cos\theta_i^b\sin\psi_i^b - z\sin\theta_i^b \\ \bar{y} &= -x\sin\psi_i^b + y\cos\theta_i^b \\ \bar{z} &= x\sin\theta_i^b\cos\psi_i^b + y\sin\theta_i^b\sin\psi_i^b + z\cos\psi_i^b - \nu_0/\cos\theta_{\rm i} \end{aligned}\right\}, \tag{7.1}$$

and ν_0 is the z–value of the origin of the $(\bar{x}, \bar{y}, \bar{z})$ coordinates. A schematic of the $(\bar{x}, \bar{y}, \bar{z})$ coordinates is shown in Figure 7.1, where $\mathbf{u}_{\bar{x}}$, $\mathbf{u}_{\bar{y}}$ and $\mathbf{u}_{\bar{z}}$ are the basis vectors. Clearly, the $z\bar{z}$ plane is the plane of incidence; while the $\bar{x}$ and $\bar{y}$ axes are parallel and perpendicular to the plane of incidence, respectively.

The incident beam can be decomposed into an angular spectrum of plane waves [82]. Therefore, the electromagnetic field phasors of the 3D incident beam are written in the $(\bar{x}, \bar{y}, \bar{z})$ coordinates as

$$\left.\begin{aligned} \mathbf{E}_i(\bar{x}, \bar{y}, \bar{z}) = {} & \int_{-\infty}^{\infty}\int_{-\infty}^{\infty} \Psi(\vartheta_x, \vartheta_y)\mathbf{e}_i(\vartheta_x, \vartheta_y) \\ & \times\exp\left[ik_0 n_{hs}(\vartheta_x\bar{x} + \vartheta_y\bar{y} + \vartheta_z\bar{z})\right] \mathrm{d}\vartheta_x\mathrm{d}\vartheta_y \\ \mathbf{H}_i(\bar{x}, \bar{y}, \bar{z}) = {} & \int_{-\infty}^{\infty}\int_{-\infty}^{\infty} \Psi(\vartheta_x, \vartheta_y)\mathbf{h}_i(\vartheta_x, \vartheta_y) \\ & \times\exp\left[ik_0 n_{hs}(\vartheta_x\bar{x} + \vartheta_y\bar{y} + \vartheta_z\bar{z})\right] \mathrm{d}\vartheta_x\mathrm{d}\vartheta_y \end{aligned}\right\}, \quad z \leq 0\,. \tag{7.2}$$

In (7.2), the real–valued ϑ_x and ϑ_y together define the domain of the angular spectrum of plane waves, while $\vartheta_z = +\sqrt{1 - \vartheta_x^2 - \vartheta_y^2}$ is either real–valued or complex–valued. The unit vectors $\mathbf{e}_i(\vartheta_x, \vartheta_y)$ and $\mathbf{h}_i(\vartheta_x, \vartheta_y)$, respectively, represent the electric and magnetic fields of a plane wave specified by $(\vartheta_x, \vartheta_y)$; while the angular–spectrum function $\Psi(\vartheta_x, \vartheta_y)$ defines the profile of the incident beam.

The substitution of (7.1) into (7.2) yields

$$\left.\begin{aligned}\mathbf{E}_i(x,y,z) &= \int_{-\infty}^{\infty}\int_{-\infty}^{\infty} \Psi(\vartheta_x,\vartheta_y)\mathbf{e}_i(\vartheta_x,\vartheta_y)\exp[i(\mathbf{k}_+^{(0)}\cdot\mathbf{r}+\varpi_0)]\,\mathrm{d}\vartheta_x\mathrm{d}\vartheta_y \\ \mathbf{H}_i(x,y,z) &= \int_{-\infty}^{\infty}\int_{-\infty}^{\infty} \Psi(\vartheta_x,\vartheta_y)\mathbf{h}_i(\vartheta_x,\vartheta_y)\exp[i(\mathbf{k}_+^{(0)}\cdot\mathbf{r}+\varpi_0)]\,\mathrm{d}\vartheta_x\mathrm{d}\vartheta_y\end{aligned}\right\}, \quad z \le 0\,, \tag{7.3}$$

where $\varpi_0 = -\vartheta_z\nu_0/\cos\theta_\mathrm{i}$. The quantity $\mathbf{k}_+^{(0)} \equiv \mathbf{k}_+^{(0)}(\vartheta_x,\vartheta_y)$ in (7.3) symbolizes the wavevector of each planewave contributor of the incident beam; thus,

$$\mathbf{k}_+^{(0)} = k_x^{(0)}\mathbf{u}_x + k_y^{(0)}\mathbf{u}_y + k_z^{(0)}\mathbf{u}_z\,, \tag{7.4}$$

where

$$\left.\begin{aligned}k_x^{(0)} &= k_0 n_{hs}(\vartheta_x\cos\theta_i^b\cos\psi_i^b - \vartheta_y\sin\psi_i^b + \vartheta_z\sin\theta_i^b\cos\psi_i^b) \\ k_y^{(0)} &= k_0 n_{hs}(\vartheta_x\cos\theta_i^b\sin\psi_i^b + \vartheta_y\cos\psi_i^b + \vartheta_z\sin\theta_i^b\sin\psi_i^b) \\ k_z^{(0)} &= k_0 n_{hs}(-\vartheta_x\sin\theta_i^b + \vartheta_z\cos\theta_i^b)\end{aligned}\right\}. \tag{7.5}$$

In order to represent $\mathbf{e}_i(\vartheta_x,\vartheta_y)$ and $\mathbf{h}_i(\vartheta_x,\vartheta_y)$, it is assumed that each of the contributing plane waves of the incident beam locally has an identical polarization state denoted via $\left\{a_\mathrm{L}^{(0)},\, a_\mathrm{R}^{(0)}\right\}$. As a matter of fact, the local planewave polarization state can be defined in a variety of ways for an optical beam [83, 84], although the polarization state of the beam is not the same as the local planewave polarization state [85]. Here, it is reasonable to consider the incident beam defined whose polarization state is approximately circular.

Hence, an approximately LCP beam is simulated by setting $a_\mathrm{R}^{(0)} = 0$, and an approximately RCP beam by $a_\mathrm{L}^{(0)} = 0$. In analogy with (2.6) and (2.7), $\mathbf{e}_i$ and $\mathbf{h}_i$ for each planewave component $(\vartheta_x,\vartheta_y)$ are written in terms of $\left\{a_\mathrm{L}^{(0)},\, a_\mathrm{R}^{(0)}\right\}$ as

$$\mathbf{e}_i = \mathbf{L}_+^{(0)}\,a_\mathrm{L}^{(0)} + \mathbf{R}_+^{(0)}\,a_\mathrm{R}^{(0)}\,, \quad \mathbf{h}_i = \frac{-in_{hs}}{\eta_0}\left[\mathbf{L}_+^{(0)}\,a_\mathrm{L}^{(0)} - \mathbf{R}_+^{(0)}\,a_\mathrm{R}^{(0)}\right], \tag{7.6}$$

where $\mathbf{L}_+^{(0)}$ and $\mathbf{R}_+^{(0)}$ are defined in (2.13) and (2.14), respectively, to vary with $\mathbf{k}_+^{(0)}$ (and thus with ϑ_x and ϑ_y).

The planewave angular spectrum can then be multiplied by the reflection or transmission coefficients and recombined to produce the reflected or the transmitted beams

[83, 86]. Therefore, the electromagnetic field phasors of the reflected and transmitted beams of order n are written as follows:

$$\mathbf{E}_r^{(n)}(x,y,z) = \int_{-\infty}^{\infty}\int_{-\infty}^{\infty} \Psi(\vartheta_x,\vartheta_y)\mathbf{e}_r^{(n)}(\vartheta_x,\vartheta_y) \times\exp[i(\mathbf{k}_-^{(n)}\cdot\mathbf{r}+\varpi_0)]\,\mathrm{d}\vartheta_x\mathrm{d}\vartheta_y\,, \quad z\le 0\,, \tag{7.7}$$

$$\mathbf{H}_r^{(n)}(x,y,z) = \int_{-\infty}^{\infty}\int_{-\infty}^{\infty} \Psi(\vartheta_x,\vartheta_y)\mathbf{h}_r^{(n)}(\vartheta_x,\vartheta_y) \times\exp[i(\mathbf{k}_-^{(n)}\cdot\mathbf{r}+\varpi_0)]\,\mathrm{d}\vartheta_x\mathrm{d}\vartheta_y\,, \quad z\le 0\,, \tag{7.8}$$

$$\mathbf{E}_t^{(n)}(x,y,z) = \int_{-\infty}^{\infty}\int_{-\infty}^{\infty} \Psi(\vartheta_x,\vartheta_y)\mathbf{e}_t^{(n)}(\vartheta_x,\vartheta_y) \times\exp[i(\mathbf{k}_+^{(n)}\cdot\tilde{\mathbf{r}}+\varpi_0)]\,\mathrm{d}\vartheta_x\mathrm{d}\vartheta_y\,, \quad z\ge d\,, \tag{7.9}$$

$$\mathbf{H}_t^{(n)}(x,y,z) = \int_{-\infty}^{\infty}\int_{-\infty}^{\infty} \Psi(\vartheta_x,\vartheta_y)\mathbf{e}_t^{(n)}(\vartheta_x,\vartheta_y) \times\exp[i(\mathbf{k}_+^{(n)}\cdot\tilde{\mathbf{r}}+\varpi_0)]\,\mathrm{d}\vartheta_x\mathrm{d}\vartheta_y\,, \quad z\ge d\,. \tag{7.10}$$

In these expressions, the electric and magnetic fields vectors $\mathbf{e}_r^{(n)}$, $\mathbf{h}_r^{(n)}$, $\mathbf{e}_t^{(n)}$ and $\mathbf{h}_t^{(n)}$ are calculated similarly to $\mathbf{e}_i$ and $\mathbf{h}_i$ of (7.6); thus,

$$\mathbf{e}_r^{(n)} = \mathbf{L}_-^{(n)}\, r_{\mathrm{L}}^{(n)} + \mathbf{R}_-^{(n)}\, r_{\mathrm{R}}^{(n)}\,, \quad \mathbf{h}_r^{(n)} = \frac{-in_{hs}}{\eta_0}\left[\mathbf{L}_-^{(n)}\, r_{\mathrm{L}}^{(n)} - \mathbf{R}_-^{(n)}\, r_{\mathrm{R}}^{(n)}\right], \tag{7.11}$$

and

$$\mathbf{e}_t^{(n)} = \mathbf{L}_+^{(n)}\, t_{\mathrm{L}}^{(n)} + \mathbf{R}_+^{(n)}\, t_{\mathrm{R}}^{(n)}\,, \quad \mathbf{h}_t^{(n)} = \frac{-in_{hs}}{\eta_0}\left[\mathbf{L}_+^{(n)}\, t_{\mathrm{L}}^{(n)} - \mathbf{R}_+^{(n)}\, t_{\mathrm{R}}^{(n)}\right]. \tag{7.12}$$

For (7.11) and (7.12), $\mathbf{L}_\pm^{(n)}$ and $\mathbf{R}_\pm^{(n)}$ are defined in (2.13) and (2.14), respectively; while the amplitude pairs $\left\{r_{\mathrm{L}}^{(n)},\, r_{\mathrm{R}}^{(n)}\right\}$ and $\left\{t_{\mathrm{L}}^{(n)},\, t_{\mathrm{R}}^{(n)}\right\}$, which are functions of ϑ_x and ϑ_y, need to be determined by means of the numerical solution procedure devised in Chapter 2. The electromagnetic field phasors of the reflected and transmitted beams are thereafter obtained from (7.7)–(7.10).

Additionally, similar definitions as (3.5) are needed for the electromagnetic field phasors of the reflected and transmitted beams when $\alpha = 0$; i.e.,

$$\mathbf{E}_r^{(0)}(x,y,z) \Leftarrow \sum_{|n|\le \mathrm{N}_t} \mathbf{E}_r^{(n)}(x,y,z)\,, \quad \mathbf{H}_r^{(0)}(x,y,z) \Leftarrow \sum_{|n|\le \mathrm{N}_t} \mathbf{H}_r^{(n)}(x,y,z) \tag{7.13}$$

and

$$\mathbf{E}_t^{(0)}(x,y,z) \Leftarrow \sum_{|n|\le \mathrm{N}_t} \mathbf{E}_t^{(n)}(x,y,z)\,, \quad \mathbf{H}_t^{(0)}(x,y,z) \Leftarrow \sum_{|n|\le \mathrm{N}_t} \mathbf{H}_t^{(n)}(x,y,z)\,, \tag{7.14}$$

because all nonspecular field phasors fold into the specular ones [86].

7.2 Lateral Shifts on Reflection

In general, lateral shifts on reflection are expected because every planewave component of an incident beam experiences different phase and magnitude changes on reflection. Reflection of an optical beam by a slanted chiral STF occurs in different Floquet–harmonic orders, and each reflected beam of order n shifts by $\mathbf{d}^{(n)}$ in the $z = 0$ plane relative to the incident beam. The value of $\mathbf{d}^{(n)}$ is represented by the relative difference between the first moments of the energy densities of the electric fields $\mathbf{E}_i(x,y,z)$ and $\mathbf{E}_r^{(n)}(x,y,z)$, respectively, evaluated on the interface plane $z = 0$. Thus,

$$\mathbf{d}^{(n)} = \mathbf{\Delta}_r^{(n)} - \mathbf{\Delta}_i\,, \tag{7.15}$$

where

$$\mathbf{\Delta}_i = \left(\int_{-\infty}^{\infty}\int_{-\infty}^{\infty} (x\mathbf{u}_x + y\mathbf{u}_y)|\mathbf{E}_i|^2\,\mathrm{d}x\mathrm{d}y\right)\left(\int_{-\infty}^{\infty}\int_{-\infty}^{\infty} |\mathbf{E}_i|^2\,\mathrm{d}x\mathrm{d}y\right)^{-1} \tag{7.16}$$

and

$$\mathbf{\Delta}_r^{(n)} = \left(\int_{-\infty}^{\infty}\int_{-\infty}^{\infty} (x\mathbf{u}_x + y\mathbf{u}_y)|\mathbf{E}_r^{(n)}|^2\,\mathrm{d}x\mathrm{d}y\right)\left(\int_{-\infty}^{\infty}\int_{-\infty}^{\infty} |\mathbf{E}_r^{(n)}|^2\,\mathrm{d}x\mathrm{d}y\right)^{-1}. \tag{7.17}$$

A lateral shift is always in the plane of incidence (i.e., the $\bar{z}z$ plane) for 2D beams, but may comprise components both in and normal to the $\bar{z}z$ plane for 3D beams.

Let $\mathbf{d}_{\mathrm{L}}^{(n)}$ and $\mathbf{d}_{\mathrm{R}}^{(n)}$ denote the lateral shifts of order n by LCP and RCP beams, respectively. It is convenient to represent $\mathbf{d}_{\mathrm{L}}^{(n)}$ and $\mathbf{d}_{\mathrm{R}}^{(n)}$ in the form

$$\left.\begin{aligned} \mathbf{d}_{\mathrm{L}}^{(n)} &= d_{\mathrm{L}}^{(n)\parallel}\mathbf{u}_\parallel + d_{\mathrm{L}}^{(n)\perp}\mathbf{u}_\perp \\ \mathbf{d}_{\mathrm{R}}^{(n)} &= d_{\mathrm{R}}^{(n)\parallel}\mathbf{u}_\parallel + d_{\mathrm{R}}^{(n)\perp}\mathbf{u}_\perp \end{aligned}\right\}, \tag{7.18}$$

where the unit vectors $\mathbf{u}_{\parallel} = \mathbf{u}_{\bar{y}} \times \mathbf{u}_z$ and $\mathbf{u}_{\perp} = \mathbf{u}_{\bar{y}}$ are parallel and perpendicular to the $\bar{z}z$ plane, respectively. Clearly, $d_{\mathrm{L}}^{(n)\parallel}$ and $d_{\mathrm{R}}^{(n)\parallel}$ represent the in–plane shifts; while $d_{\mathrm{L}}^{(n)\perp}$ and $d_{\mathrm{R}}^{(n)\perp}$ represent the out–of–plane shifts [84].

7.3 Solution and Analysis

7.3.1 Preliminaries

The numerical solution procedure devised in Section 7.1 is suitable for the computation of lateral shifts of reflected optical beams in the following two problems:

- **Problem A:** The half–spaces of reflection and transmission are vacuous.
- **Problem B:** The half–spaces of reflection and transmission are occupied by a dielectric medium that is optically denser than the slanted chiral STF.

For Problem A, the focus lies on the lateral shift of a co–handed optical beam on Bragg reflection, when the angular spectrum of the beam lies totally within the angular spread of the Bragg regime. For Problem B, total reflection of the incident beam must occur when $|\theta_i^b|$ exceeds a critical value θ_{ic}^b. Therefore, the focus is on the Goos–Hänchen shifts of an incident beam on total reflection [62, 63]. Both of these problems are similar to their counterparts in Chapter 4.

The angular–spectrum function of a 3D Gaussian beam is [53, 83]

$$\Psi(\vartheta_x, \vartheta_y) = \frac{\rho_0^2}{2\pi} \exp\left[-\frac{1}{2}\,\rho_0^2\left(\vartheta_x^2 + \vartheta_y^2\right)\right], \tag{7.19}$$

where $\rho_0 = k_0 n_{hs} w_0$ and w_0 is the beam waist. The 2D Gaussian beam is represented through the angular–spectrum function

$$\Psi(\vartheta_x, \vartheta_y) = \frac{\rho_0}{\sqrt{2\pi}} \exp\left(-\frac{1}{2}\,\rho_0^2 \vartheta_x^2\right) \delta(\vartheta_y)\,, \tag{7.20}$$

where $\delta(\cdot)$ is the Dirac delta function.

Computations were carried out with the same parameters as those in Chapter 4, with the selections $\alpha = 0$, 10°, and 15°. For simplicity, $\nu_0 = 0$ was chosen. The 3D Gaussian beam profile was uniformly discretized to a 80×80 mesh in the angular–spectrum domain $\left\{(\vartheta_x, \vartheta_y) \,\middle|\, \sqrt{\vartheta_x^2 + \vartheta_y^2} \leq 4/\rho_0\right\}$, which was sufficient to calculate the approximate value of $|\mathbf{E}_i|^2$ of (7.2) with less than 0.01% inaccuracy. Accordingly, $80 \times 80 = 6400$ plane waves corresponding to different values of the pair $(\vartheta_x, \vartheta_y)$ were generated to span the entire angular spectrum of the reflected/transmitted beams.

7.3.2 Problem A: Lateral Shift of Gaussian Beam on Bragg reflection

In analogy with the circular Bragg phenomenon, a co–handed incident beam would be mostly reflected, and thus shifted with little distortion in profile, when its angular spectrum lies totally within the angular spread of the Bragg regime (if possible at that wavelength). Figure 7.2 shows the in–plane shift of a 2D RCP (i.e., co–handed) Gaussian beam on Bragg reflection by either a chiral STF ($\alpha = 0$) or a slanted chiral STF ($\alpha = 10^\circ$), when $n_{hs} = 1$. The in–plane shift presented in this figure was calculated as

$$d_{\mathrm{Br}}^{\parallel} = \begin{cases} d_{\mathrm{R}}^{(0)\parallel}\,, & \alpha = 0\,, \\ d_{\mathrm{R}}^{(\mp 2)\parallel}\,, & \alpha \gtrless 0\,, \end{cases} \tag{7.21}$$

because the (slanted) chiral STF is structurally right–handed; while the out–of–plane shift $d_{\mathrm{Br}}^{\perp} \equiv 0$. Clearly, the in–plane shift is always *forward* (i.e., $d_{\mathrm{Br}}^{\parallel} \sin\theta_i^b \geq 0$) and almost symmetric with respect to θ_{i} when $\alpha = 0$. However, when $\alpha \neq 0$, the in–plane shift could be either forward or *backward* (i.e., $d_{\mathrm{Br}}^{\parallel} \sin\theta_i^b \leq 0$), depending on the angles θ_i^b and ψ_i^b. For example, Figure 7.2(a) shows negative $d_{\mathrm{Br}}^{\parallel}$ for $\sin\theta_i^b \in (0,\, 0.31)$ when $\psi_i^b = 0$ and $\alpha = 10^\circ$. The reason for occurrence of a backward shift is simply because reflection occurs mostly in the order $n = \mp 2$ for $\alpha \gtrless 0$. Incidentally, negative shifts do not violate causality [87, 88].

The in–plane shift of the RCP Gaussian beam on Bragg reflection can be estimated by

$$d_{\rm Br}^{||} \approx \begin{cases} -\dfrac{\partial\varphi\left(r_{\rm RR}^{(0)}\right)}{\partial k_{hs}^{||}}\left[1+\mathcal{O}\left(\dfrac{\mathrm{R}_{\rm LR}^{(0)}}{\mathrm{R}_{\rm RR}^{(0)}}\right)\right], & \alpha = 0\,, \\ -\dfrac{\partial\varphi\left(r_{\rm RR}^{(\mp 2)}\right)}{\partial k_{hs}^{||}}\left[1+\mathcal{O}\left(\dfrac{\mathrm{R}_{\rm LR}^{(\mp 2)}}{\mathrm{R}_{\rm RR}^{(\mp 2)}}\right)\right], & \alpha \gtrless 0\,, \end{cases} \tag{7.22}$$

where $\varphi(\sigma)$ is the phase φ of the planewave reflection coefficient σ computed by setting $\theta_i^p = \theta_i^b$, and $k_{hs}^{||} = k_0 n_{hs} \sin\theta_i^p$. This simple formula is adequate because the co–handed reflection coefficient —- either $r_{\rm RR}^{(0)}$ for $\alpha = 0$ or $r_{\rm RR}^{(\mp 2)}$ for $\alpha \gtrless 0$ — does not change significantly in magnitude when θ_i^p lies squarely within the angular spread of the Bragg regime; see Figure 4.3. In addition, because $\mathrm{R}_{\rm LR}^{(0)} << \mathrm{R}_{\rm RR}^{(0)}$ (for $\alpha = 0$) and $\mathrm{R}_{\rm LR}^{(\mp 2)} << \mathrm{R}_{\rm RR}^{(\mp 2)}$ (for $\alpha \gtrless 0$) in the Bragg regime, the minute items $\mathcal{O}\left(\frac{\mathrm{R}_{\rm LR}^{(0)}}{\mathrm{R}_{\rm RR}^{(0)}}\right)$ and $\mathcal{O}\left(\frac{\mathrm{R}_{\rm LR}^{(\mp 2)}}{\mathrm{R}_{\rm RR}^{(\mp 2)}}\right)$ on the right side of (7.22) can be omitted.

The phases of the co–handed reflection coefficients $r_{\rm RR}^{(0)}$ (for $\alpha = 0$) and $r_{\rm RR}^{(-2)}$ (for $\alpha = 10^\circ$) are presented in Figure 7.3 as functions of θ_i^p and ψ_i^p. In fact, the phases in Figure 7.3 appear to be approximately second–order polynomials of $\sin\theta_i^p$ that are defined piecewise. Correspondingly, $d_{\rm Br}^{||}$ should be approximately linearly proportional to $\sin\theta_i^b$, which is predicted by (7.22) and basically confirmed by the plots of Figure 7.2. In addition, the plot of $\varphi\left(r_{\rm RR}^{(-2)}\right)$ in Figure 7.3(a) is symmetric about $\sin\theta_i^p = 0.31$, but not about $\sin\theta_i^p = 0$, which explains the backward shifts in Figure 7.2(a) for the slanted chiral STF.

When $\alpha \neq 0$, the reflected field comprises beams of different orders n. Thus, lateral shifts of different orders are possible, as indicated by (7.18). In fact, the dominant Bragg reflection of the co–handed Gaussian beam, which occurs in the order $n = \mp 2$ for $\alpha \gtrless 0$, is always accompanied by a weak reflection of order $n = 0$ (i.e., $0.01 < |\mathbf{E}_r^{(0)}|^2/|\mathbf{E}_i|^2 < 0.1$). Certainly, the reflected beam of order $n = 0$ shifts laterally away from the incident beam as well. Figure 7.4 shows the in–plane shift $d_{\rm R}^{(0)\|}$ of the 2D RCP Gaussian beam, when $\alpha = 10^\circ$. The shift $d_{\rm R}^{(0)\|}$ oscillates with θ_i^b about the zero value, indicating that the specularly reflected beam can shift in the forward as well as the backward directions.

A comparison of Figures 7.2 and 7.4 indicates a distinction between $d_{\mathrm{R}}^{(0)\parallel}$ and $d_{\mathrm{Br}}^{\parallel}$ when $\alpha \neq 0$, implying the fact that the lateral shifts of different orders are different. The circular Bragg phenomenon being the chief attraction of the slanted chiral STF, secondary lateral shifts are of incidental importance.

7.3.3 Problem B: Goos–Hänchen Shifts of Gaussian Beams

Total Reflection of Gaussian Beam

As an incident plane wave is totally reflected in the order of $n = 0$, so does an optical beam. The lateral shift of the reflected beam under the total–reflection condition is called the Goos–Hänchen shift [62]

$$\mathbf{d}^{\mathrm{GH}} = \mathbf{d}^{(0)}\,, \tag{7.23}$$

for arbitrary α. Two different Goos–Hänchen shifts are possible, one for LCP beams and the other for RCP beams. The shifts are denoted by $\mathbf{d}_{\mathrm{L}}^{\mathrm{GH}}$ and $\mathbf{d}_{\mathrm{R}}^{\mathrm{GH}}$, respectively.

Since an optical beam is an angular continuum of plane waves, the critical angle θ_{ic}^{b} for an optical beam is certainly different from its planewave counterpart θ_{ic}^{p}. Table 7.1 shows the approximate values of θ_{ic}^{b} obtained from actual computation as well as from a simple estimation procedure. The value of θ_{ic}^{b} was actually computed by ascertaining that $|\mathbf{E}_r^{(0)}|^2$ rises to $0.995|\mathbf{E}_i|^2$ as $|\theta_i^b|$ increases to θ_{ic}^{b}. The simple estimate

$$\theta_{ic}^{b} \approx \theta_{ic}^{p} + \sin^{-1}(2/\rho_0)\,, \tag{7.24}$$

is based on the assumption that all planewave components in the domain $\left\{(\vartheta_x, \vartheta_y)\,\middle|\, \sqrt{\vartheta_x^2 + \vartheta_y^2} \leq 2/\rho_0\right\}$ of an incident beam should be totally reflected. As is clear from Table 7.1, (7.24) is a good predictor of θ_{ic}^{b}, especially when $w_0 \geq 3\lambda_{hs}$, where $\lambda_{hs} = \lambda_0/n_{hs}$ is the wavelength in the medium filling the half–spaces of incidence and reflection. Computational results showed that θ_{ic}^{b} is largely unaffected by ψ_i^b. The computed values of θ_{ic}^{b} are employed for all the plots presented in Figures 7.5, 7.7 and 7.10.

Table 7.1: Values of θ_{ic}^b for various w_0 as estimated by (7.24) and from actual computation.

w_0	estimated from (7.24)	computed for 2D beam	computed for 3D beam
$2\lambda_{hs}$	37.2°	39.3°	39.9°
$3\lambda_{hs}$	34.1°	35.1°	35.6°
$4\lambda_{hs}$	32.6°	32.9°	32.9°
$6\lambda_{hs}$	31.1°	31.3°	31.3°

Goos–Hänchen shifts of 2D Gaussian Beams

Figure 7.5 shows the in–plane Goos–Hänchen shifts $d_{\rm L}^{\rm GH\parallel}$ and $d_{\rm R}^{\rm GH\parallel}$ as functions of $\sin\theta_i^b \in [\sin\theta_{ic}^b, 1)$ when the incident beam is 2D. Similarly, Figure 7.6 presents $d_{\rm L}^{\rm GH\parallel}$ and $d_{\rm R}^{\rm GH\parallel}$ plotted against $\psi_i^b \in [0, 180°)$ when $\theta_{\rm i} = 37.5° > \theta_{ic}^b$. It is clear from Figure 7.5 that α affects the Goos–Hänchen shift at low angles of incidence for total reflection.

A distinction between $d_{\rm L}^{\rm GH\parallel}$ and $d_{\rm R}^{\rm GH\parallel}$ is unambiguously evident at low values of $|\theta_i^b| > \theta_{ic}^b$ when $\alpha = 0$ (Figure 7.6). However, that distinction diminishes for all post–critical $\theta_{\rm i}$ when $\alpha \neq 0$, as illustrated by the plots in Figure 7.6 for $\alpha = 15°$. Similarly, the variations of $d_{\rm L}^{\rm GH\parallel}$ and $d_{\rm R}^{\rm GH\parallel}$ with ψ_i^b are less pronounced for $\alpha \neq 0$ than for $\alpha = 0$.

Although the foregoing effects of α may be considered small in conventional optics practice, as they amount to small fractions of the wavelength, their nanotechnological significance cannot be denied [89]. That becomes evident on noting that quantum dots are 1–2 nm in diameter, globular proteins are of 6 nm diameter, while gate oxide films have been shrunk to about 2 nm in thickness [90]. In comparison, 1% of the typical λ_0 in the visible regime is between 4 and 7 nm.

Figure 7.7 shows the effect of the beam waist width w_0 on the Goos–Hänchen shift when $\alpha = 15°$. Enhancement of the beam waist decreases the critical angle θ_{ic}^b, as shown by Table 7.1 also. Furthermore, both $d_{\rm L}^{\rm GH\parallel}$ and $d_{\rm R}^{\rm GH\parallel}$ decrease (increase) with increasing

beam waist when the post–critical $|\theta_i^b|$ is low (high).

The Goos–Hänchen shift of a 2D Gaussian beam can be estimated by

$$\left.\begin{aligned} d_{\mathrm{L}}^{\mathrm{GH}\parallel} &\approx -\mathrm{R}_{\mathrm{LL}}^{(0)}\frac{\partial\varphi\left(r_{\mathrm{LL}}^{(0)}\right)}{\partial k_{hs}^{||}} - \mathrm{R}_{\mathrm{RL}}^{(0)}\frac{\partial\varphi\left(r_{\mathrm{RL}}^{(0)}\right)}{\partial k_{hs}^{||}} \\ d_{\mathrm{R}}^{\mathrm{GH}\parallel} &\approx -\mathrm{R}_{\mathrm{LR}}^{(0)}\frac{\partial\varphi\left(r_{\mathrm{LR}}^{(0)}\right)}{\partial k_{hs}^{||}} - \mathrm{R}_{\mathrm{RR}}^{(0)}\frac{\partial\varphi\left(r_{\mathrm{RR}}^{(0)}\right)}{\partial k_{hs}^{||}} \end{aligned}\right\}, \tag{7.25}$$

in analogy with (7.22). Figures 7.8 and 7.9 contain the plots of φ of different reflection coefficients, for both $\alpha = 0$ and $\alpha = 15°$. Although $\varphi\left(r_{\mathrm{LL}}^{(0)}\right)$ and $\varphi\left(r_{\mathrm{RR}}^{(0)}\right)$ are little affected by α (Figure 7.8(b)), $\varphi\left(r_{\mathrm{RL}}^{(0)}\right)$ and $\varphi\left(r_{\mathrm{LR}}^{(0)}\right)$ are absolutely under its influence at low values of $|\theta_i^p| \geq \theta_{ic}^p$ (Figure 7.8(a)). According to (7.25), the Goos–Hänchen shifts $d_{\mathrm{L}}^{\mathrm{GH}\parallel}$ and $d_{\mathrm{R}}^{\mathrm{GH}\parallel}$ should be affected by α at low values of $|\theta_i^b| \geq \theta_{ic}^b$, by noting the fact that $\frac{\mathrm{R}_{\mathrm{RL}}^{(0)}}{\mathrm{R}_{\mathrm{LL}}^{(0)}}$ and $\frac{\mathrm{R}_{\mathrm{LR}}^{(0)}}{\mathrm{R}_{\mathrm{RR}}^{(0)}}$ are not trivial at low values of $|\theta_i^p| \geq \theta_{ic}^p$ (Figures 4.4 and 4.5). Similarly, because $\varphi\left(r_{\mathrm{LL}}^{(0)}\right) \approx \varphi\left(r_{\mathrm{RR}}^{(0)}\right)$ and $\varphi\left(r_{\mathrm{RL}}^{(0)}\right) \neq \varphi\left(r_{\mathrm{LR}}^{(0)}\right)$ for $\alpha = 0$ (Figure 7.9(a)), a distinction between $d_{\mathrm{L}}^{\mathrm{GH}\parallel}$ and $d_{\mathrm{R}}^{\mathrm{GH}\parallel}$ is undoubtedly evident when $\alpha = 0$ (Figure 7.6). However, that distinction reduces when $\alpha \neq 0$, because $\varphi\left(r_{\mathrm{LL}}^{(0)}\right) \approx \varphi\left(r_{\mathrm{RR}}^{(0)}\right)$ and the difference between $\varphi\left(r_{\mathrm{LR}}^{(0)}\right)$ and $\varphi\left(r_{\mathrm{RL}}^{(0)}\right)$ is minute then (Figure 7.9(b)).

Goos–Hänchen Shifts of 3D Gaussian Beams

Figure 7.10 presents the plots of $\mathbf{d}_{\mathrm{L}}^{\mathrm{GH}}$ and $\mathbf{d}_{\mathrm{R}}^{\mathrm{GH}}$ against $\sin\theta_i^b \in [\sin\theta_{ic}^b, 1)$ for $\alpha = 0$ and $\alpha = 15°$, when the beam is 3D. The most prominent feature of the Goos–Hänchen phenomenon for 3D CP beams is that both in–plane ($d_{\mathrm{L}}^{\mathrm{GH}\parallel}$ and $d_{\mathrm{R}}^{\mathrm{GH}\parallel}$) and out–of–plane ($d_{\mathrm{L}}^{\mathrm{GH}\perp}$ and $d_{\mathrm{R}}^{\mathrm{GH}\perp}$) shifts are not zero. In fact, the out–of–plane Goos–Hänchen shift increases in amplitude as the post–critical $|\theta_i^b|$ decreases.

Furthermore, because $d_{\mathrm{L}}^{\mathrm{GH}\perp} < 0$ and $d_{\mathrm{R}}^{\mathrm{GH}\perp} > 0$ for any $|\theta_{\mathrm{i}}| \geq \theta_{ic}^b$, the direction of the out–of–plane Goos–Hänchen shift depends on the handedness of the incident beam in relation to the structural handedness of the thin film. In contrast, the in–plane Goos–Hänchen shift is always directed forward and exhibits characteristics similar to that of a 2D

beam. Specifically, $d_{\mathrm{L}}^{\mathrm{GH}\parallel} \neq d_{\mathrm{R}}^{\mathrm{GH}\parallel}$ at low values of $|\theta_i^b| \geq \theta_{ic}^b$ when $\alpha = 0$ (Figure 7.10(a)), but that distinction diminishes for all post–critical θ_i^b when $\alpha \neq 0$ (Figure 7.10(b)).

The effect of ψ_i^b on the Goos–Hänchen shift of a 3D Gaussian beam is illustrated in Figure 7.11, wherein $\theta_i^b = 37.5^\circ > \theta_{ic}^b$. Both in–plane and out–of–plane Goos–Hänchen shifts are less affected by ψ_i^b for $\alpha \neq 0$ than for $\alpha = 0$. In addition, it is clear from Figure 7.11(b) that $\left| d_{\mathrm{L}}^{\mathrm{GH}\perp} \right| \approx \left| d_{\mathrm{R}}^{\mathrm{GH}\perp} \right|$ for $\alpha \neq 0$, but not for $\alpha = 0$, thereby implying that the magnitude of out–of–plane Goos–Hänchen shift is not affected by the structural handedness of the slanted chiral STF with $\alpha \neq 0$.

The occurrence of the out–of–plane Goos–Hänchen shift depends on the ellipticity of the polarization state of the 3D incident beam. For example, when the 3D incident beam is approximately linearly polarized (i.e., either *s*– or *p*–polarized), no out–of–plane shift would occur on total reflection.

7.4 Concluding Remarks

In conclusion, there are two interesting types of lateral shifts of optical beams on reflection by slanted chiral STFs. One is the lateral shift of a co–handed optical beam that is mostly reflected due to the circular Bragg phenomenon. The other is the Goos–Hänchen shift that occurs when the beam is totally reflected. Four remarkable features of the two types of lateral shifts of optical beams are as follows:

- The lateral shift of a co–handed beam on Bragg reflection can be either forward or backward when $\alpha \neq 0$, depending on the directionality of incidence.

- The Goos–Hänchen shift is affected by both slantedness and structural handedness of the slanted chiral STF, when the post–critical angle of incidence (i.e., $|\theta_i^b| \geq \theta_{ic}^b$) is small.

- When the incident beam is CP and 3D, both in–plane and out–of–plane Goos–Hänchen shifts occur on total reflection. In particular, the out–of–plane Goos–Hänchen shift increases in amplitude as the angle of incidence decreases, and it can be either forward or backward.

- Lateral shift of each type at low–ultraviolet and longer wavelengths is large enough in magnitude to be significant for nanotechnology.

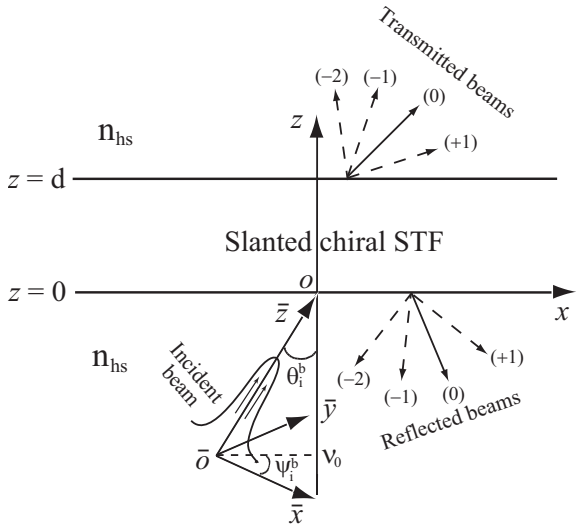

Figure 7.1: Cartesian coordinates $(\bar{x}, \bar{y}, \bar{z})$ for a 3D optical beam incident on a slanted chiral STF occupying the region $0 < z < d$. Reflection and transmission occur in the two half–spaces $z < 0$ and $z > d$ in both specular $(n = 0)$ and nonspecular $(n \neq 0)$ orders when $\alpha \neq 0$. All nonspecular orders fold into the specular one when $\alpha = 0$.

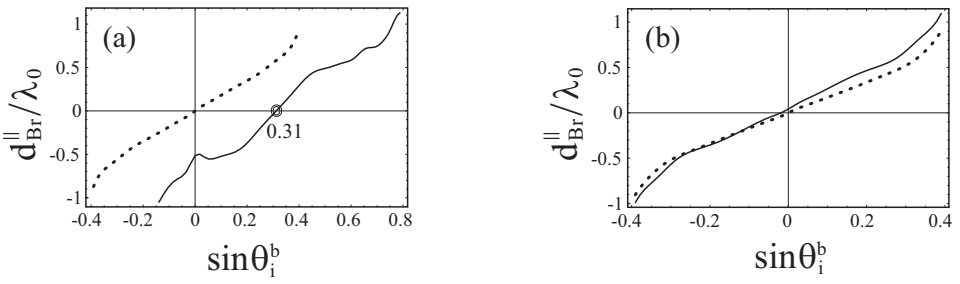

Figure 7.2: Normalized in–plane shift $d^{||}_{\mathrm{Br}}/\lambda_0$ as a function of $\sin\theta_{\mathrm{i}}$, when $\alpha = 0$ (dotted lines) and $\alpha = 10^\circ$ (solid lines). The incident beam is 2D RCP Gaussian, $\lambda_0 = \lambda_0^{\mathrm{Br}}\Big|_{\theta_i^p=0}$, $w_0 = 4\lambda_0$, and $\nu_0 = 0$. (a) $\psi_i^b = 0$, and (b) $\psi_i^b = 90^\circ$. The values of θ_i^b chosen lie squarely within the angular spread of the Bragg regime, so that the co–handed beam is mostly reflected. See Figure 4.1 for other parameters.

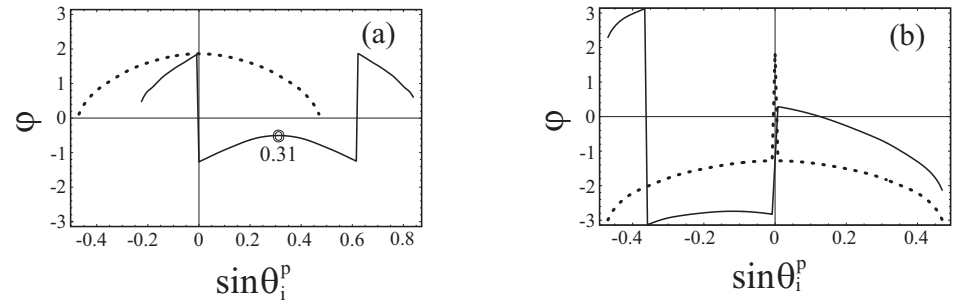

Figure 7.3: Phases of the planewave reflection coefficients $r^{(0)}_{\mathrm{RR}}$ (dotted lines) for $\alpha = 0$, and $r^{(-2)}_{\mathrm{RR}}$ (solid lines) for $\alpha = 10^\circ$. (a) $\psi_i^p = 0$, and (b) $\psi_i^p = 90^\circ$. See Figure 4.1 for other parameters.

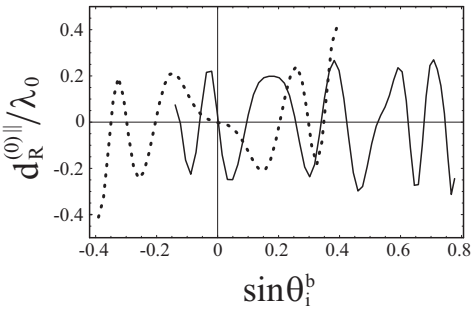

Figure 7.4: Normalized in–plane shift $d_{\mathrm{R}}^{(0)\parallel}/\lambda_0$ as a function of $\sin\theta_i^b$, computed for $\psi_i^b = 0$ (solid line) and $\psi_i^b = 90°$ (dotted line), when $\alpha = 10°$. The incident beam is 2D RCP (i.e., co–handed) Gaussian, and the values of θ_i^b chosen lie squarely within the angular spread of the Bragg regime. See Figure 7.2 for other parameters.

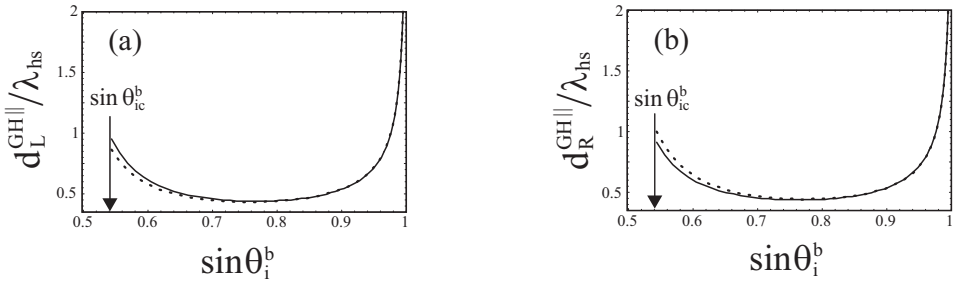

Figure 7.5: Normalized Goos–Hänchen shifts (a) $d_{\mathrm{L}}^{\mathrm{GH}\parallel}/\lambda_{hs}$ and (b) $d_{\mathrm{R}}^{\mathrm{GH}\parallel}/\lambda_{hs}$ as functions of $\sin\theta_i^b \in [\sin\theta_{ic}^b, 1)$, computed for $\alpha = 0$ (dotted lines) and $\alpha = 15°$ (solid lines), when $\psi_i^b = 120°$, $n_{hs} = 4$, $\lambda_0 = 727$ nm, and $w_0 = 4\lambda_{hs}$. See Figure 7.2 for other parameters.

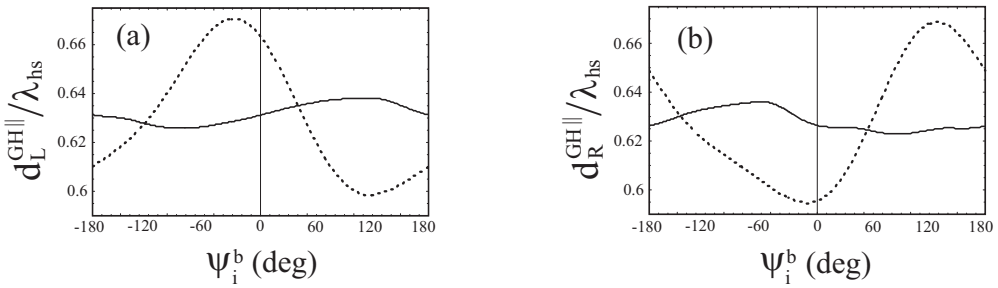

Figure 7.6: Same as Figure 7.5, except $d_{\rm L}^{\rm GH\parallel}/\lambda_{hs}$ and $d_{\rm R}^{\rm GH\parallel}/\lambda_{hs}$ are plotted against $\psi_i^b \in [-180°, 180°)$, for a fixed post–critical $\theta_i^b = 37.5°$.

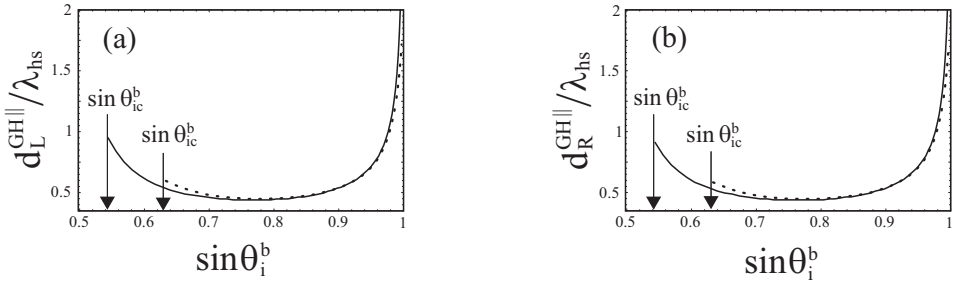

Figure 7.7: Normalized Goos–Hänchen shifts (a) $d_{\rm L}^{\rm GH\parallel}/\lambda_{hs}$ and (b) $d_{\rm R}^{\rm GH\parallel}/\lambda_{hs}$ as functions of $\sin\theta_{\rm i} \in [\sin\theta_{ic}^b, 1)$, computed for $w_0 = 2\lambda_{hs}$ (dotted lines) and $w_0 = 4\lambda_{hs}$ (solid lines), when $\alpha = 15°$. See Figure 7.5 for other parameters.

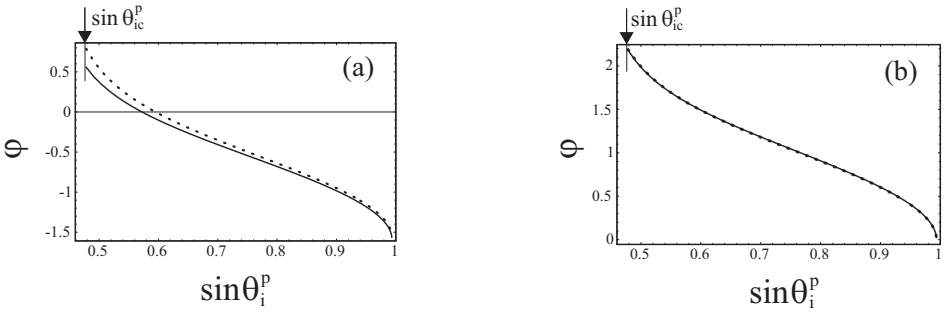

Figure 7.8: Phases of the planewave reflection coefficients (a) $r_{\mathrm{LR}}^{(0)}$ and (b) $r_{\mathrm{RR}}^{(0)}$ as functions of $\sin\theta_i^p \in [\sin\theta_{ic}^p, 1)$, computed for $\alpha = 0$ (dotted lines) and $\alpha = 15°$ (solid lines), when $\psi_i^p = 120°$. See Figure 4.4 for other parameters.

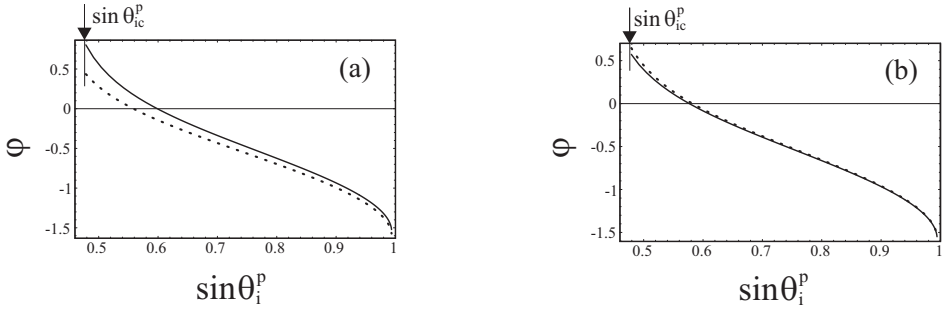

Figure 7.9: Phases of the planewave reflection coefficients $r_{\mathrm{LR}}^{(0)}$ (solid lines) and $r_{\mathrm{RL}}^{(0)}$ (dotted lines) as functions of $\sin\theta_i^p \in [\sin\theta_{ic}^p, 1)$, computed for (a) $\alpha = 0$ and (b) $\alpha = 15°$, when $\psi_i^p = 120°$. See Figure 7.8 for other parameters.

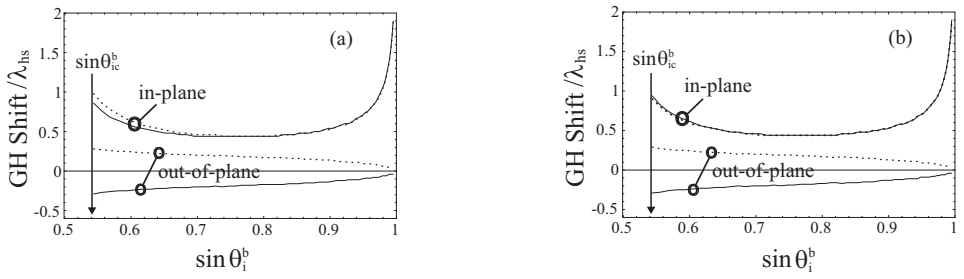

Figure 7.10: Normalized in–plane Goos–Hänchen shifts $d_{\rm L}^{\rm GH\parallel}/\lambda_{hs}$ (solid lines) and $d_{\rm R}^{\rm GH\parallel}/\lambda_{hs}$ (dotted lines), and normalized out–of–plane Goos–Hänchen shifts $d_{\rm L}^{\rm GH\perp}/\lambda_{hs}$ (solid lines) and $d_{\rm R}^{\rm GH\perp}/\lambda_{hs}$ (dotted lines) as functions of $\sin\theta_i^b \in [\sin\theta_{ic}^b, 1)$, computed for (a) $\alpha = 0$ and (b) $\alpha = 15°$. The incident beam is 3D and Gaussian. See Figure 7.5 for other parameters.

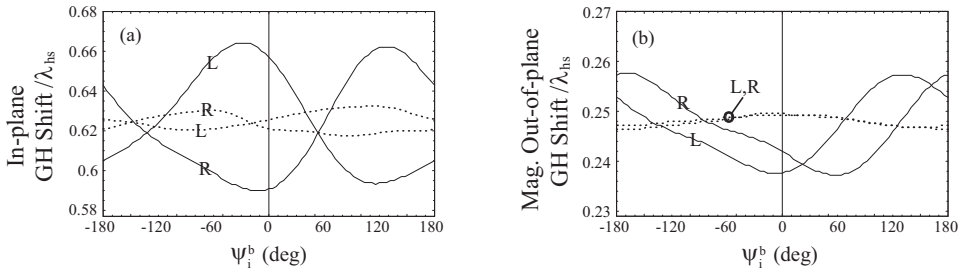

Figure 7.11: (a) Normalized in–plane Goos–Hänchen shifts $d_{\rm L}^{\rm GH\parallel}/\lambda_{hs}$ and $d_{\rm R}^{\rm GH\parallel}/\lambda_{hs}$, and (b) magnitudes of normalized out–of–plane Goos–Hänchen shifts $-d_{\rm L}^{\rm GH\perp}/\lambda_{hs}$ and $d_{\rm R}^{\rm GH\perp}/\lambda_{hs}$ as functions of $\psi_{\rm i} \in [-180°, 180°)$, computed for $\alpha = 0$ (solid lines) and $\alpha = 15°$ (dotted lines), when $\theta_i^b = 37.5° > \theta_{ic}^b$. See Figure 7.10 for other parameters.

Chapter 8

Response of Slanted Chiral STFs to Dipolar Radiation[‡]

Apart from optical beams, dipolar sources are useful in studying nano–optics. For example, point dipoles are treated as functional models of nanoprobes in the technique of scanning near–field optical microscopy (SNOM) that is utilized in nanodetection and nanolithography [51, 52]. Novel optical phenomenons are expected for dipolar sources interacting with nanomaterials, as implied by the fact that the interparticle correlation of nanomaterials resembles the dipole–dipole interaction [91, 92]. Slanted chiral STFs, as a type of nanomaterials, must certainly respond to radiation from dipolar sources in a distinguishing manner. The analytical treatment is similar to that devised in Chapter 7 for diffraction of optical beams. Thus, the objective of this chapter is to investigate the dipolar response of slanted chiral STFs.

[‡] This chapter is partly adapted from the following paper: F. Wang, A. Lakhtakia, "Response of slanted chiral sculptured thin films to dipolar sources", Opt. Commun. **235** 133–151 (2004).

8.1 Dyadic Green Functions

Without loss of generality, a slanted chiral STF of thickness d sandwiched between two vacuous half–spaces (i.e., $n_{hs} = 1$) is considered. Let the slanted chiral STF occupy the region $0 < z < d$; a point dipolar source lies exclusively in the half–space $z \leq 0$; see Figure 8.1.

Suppose initially that the slanted chiral STF is absent; then the electric field phasors *everywhere* can be formulated as [93]

$$\mathbf{E}\left(\mathbf{r}\right) = i\omega\mu_0 \iiint\limits_{\mathbb{R}^3} \underline{\underline{\mathbf{G}}}_0(\mathbf{r},\mathbf{r}') \cdot \mathbf{J}(\mathbf{r}')\, \mathrm{d}^3\mathbf{r}' - \nabla \times \iiint\limits_{\mathbb{R}^3} \underline{\underline{\mathbf{G}}}_0(\mathbf{r},\mathbf{r}') \cdot \mathbf{K}(\mathbf{r}')\, \mathrm{d}^3\mathbf{r}' \,, \tag{8.1}$$

where $\mathbf{J}(\mathbf{r}')$ and $\mathbf{K}(\mathbf{r}')$ are the externally impressed electric and magnetic current densities, respectively, at the source position $\mathbf{r}'$; while

$$\underline{\underline{\mathbf{G}}}_0(\mathbf{r},\mathbf{r}') = \left(\underline{\underline{\mathrm{I}}} + k_0^{-2}\nabla\nabla\right)\left[\exp\left(ik_0|\mathbf{R}|\right)/4\pi|\mathbf{R}|\right] \,, \tag{8.2}$$

is the infinite–medium dyadic Green function (DGF) for free space. Here and hereafter, $\mathbf{R} = \mathbf{r} - \mathbf{r}'$, and $\mathbb{R}^3$ denotes the 3D real space.

In consonance with the distinguishing role of structural handedness, sources of circularly polarized plane waves are preferred. Hence, two Beltrami source densities

$$\left.\begin{aligned} \mathbf{W}_{\mathrm{L}} &= \mathbf{J} + i\omega\epsilon_0\mathbf{K} \\ \mathbf{W}_{\mathrm{R}} &= \mathbf{J} - i\omega\epsilon_0\mathbf{K} \end{aligned}\right\} \tag{8.3}$$

are defined [94]. These two Beltrami source configurations are of the left– and right–handed types, respectively; They can be synthesized as co–located pairs of electric and magnetic dipoles that are either parallel or anti–parallel. After substituting (8.3) into (8.1), the electric field can be rewritten as

$$\mathbf{E}\left(\mathbf{r}\right) = \frac{i\omega\mu_0}{2} \iiint\limits_{\mathbb{R}^3} \left[\underline{\underline{\mathbf{G}}}_{\mathrm{L}0}(\mathbf{r},\mathbf{r}') \cdot \mathbf{W}_{\mathrm{L}}(\mathbf{r}') + \underline{\underline{\mathbf{G}}}_{\mathrm{R}0}(\mathbf{r},\mathbf{r}') \cdot \mathbf{W}_{\mathrm{R}}(\mathbf{r}')\right] \mathrm{d}^3\mathbf{r}' \,, \tag{8.4}$$

where

$$\left.\begin{aligned}\underline{\underline{\mathbf{G}}}_{\mathrm{L}0}(\mathbf{r},\mathbf{r}') &= \left(\underline{\underline{\mathrm{I}}} + k_0^{-1}\nabla\times\underline{\underline{\mathrm{I}}}\right)\underline{\underline{\mathbf{G}}}_0(\mathbf{r},\mathbf{r}') \\ \underline{\underline{\mathbf{G}}}_{\mathrm{R}0}(\mathbf{r},\mathbf{r}') &= \left(\underline{\underline{\mathrm{I}}} - k_0^{-1}\nabla\times\underline{\underline{\mathrm{I}}}\right)\underline{\underline{\mathbf{G}}}_0(\mathbf{r},\mathbf{r}')\end{aligned}\right\}. \tag{8.5}$$

Next, in the presence of the slanted chiral STF, the electric field in either of the two half–spaces must be of the form

$$\mathbf{E}(\mathbf{r}) = \frac{i\omega\mu_0}{2}\iiint\limits_{\mathbb{R}^3}\left[\underline{\underline{\mathbf{G}}}_{\mathrm{L}}(\mathbf{r},\mathbf{r}')\cdot\mathbf{W}_{\mathrm{L}}(\mathbf{r}') + \underline{\underline{\mathbf{G}}}_{\mathrm{R}}(\mathbf{r},\mathbf{r}')\cdot\mathbf{W}_{\mathrm{R}}(\mathbf{r}')\right]\mathrm{d}^3\mathbf{r}', \quad z\notin(0,d), \tag{8.6}$$

where $\underline{\underline{\mathbf{G}}}_{\mathrm{L}}(\mathbf{r},\mathbf{r}')$ and $\underline{\underline{\mathbf{G}}}_{\mathrm{R}}(\mathbf{r},\mathbf{r}')$ are DGFs that take the presence of the slanted chiral STF into account. Synthesis of these two DGFs is accomplished through the decomposition

$$\underline{\underline{\mathbf{G}}}_{\sigma}(\mathbf{r},\mathbf{r}') = \begin{cases}\underline{\underline{\mathbf{G}}}_{\sigma 0}(\mathbf{r},\mathbf{r}') + \underline{\underline{\mathbf{G}}}_{\sigma r}(\mathbf{r},\mathbf{r}'), & z\le 0,\\ \underline{\underline{\mathbf{G}}}_{\sigma t}(\mathbf{r},\mathbf{r}'), & z\ge d,\end{cases} \qquad \sigma = \mathrm{L},\mathrm{R}. \tag{8.7}$$

As the planewave response of a slanted chiral STF can be determined by RCWA formulated in Chapter 2, $\underline{\underline{\mathbf{G}}}_{\sigma r}(\mathbf{r},\mathbf{r}')$ and $\underline{\underline{\mathbf{G}}}_{\sigma t}(\mathbf{r},\mathbf{r}')$, $(\sigma = \mathrm{L},\mathrm{R})$, can be derived therefrom. Accordingly, a spectral representation of $\underline{\underline{\mathbf{G}}}_0(\mathbf{r},\mathbf{r}')$ is necessitated; thus [95],

$$\begin{aligned}\underline{\underline{\mathbf{G}}}_0(\mathbf{r},\mathbf{r}') = {} & -k_0^{-2}\delta(\mathbf{R})\mathbf{u}_z\mathbf{u}_z + \frac{i}{4\pi^2}\int_{-\infty}^{\infty}\int_{-\infty}^{\infty}\left(k_z^{(0)}\right)^{-1} \\ & \times\exp\left(i\mathbf{k}_{\pm}^{(0)}\cdot\mathbf{R}\right)\left(\mathbf{s}^{(0)}\mathbf{s}^{(0)} + \mathbf{p}_{\pm}^{(0)}\mathbf{p}_{\pm}^{(0)}\right)\mathrm{d}k_x^{(0)}\mathrm{d}k_y^{(0)},\end{aligned} \tag{8.8}$$

where the upper signs apply for $z > z'$ and the lower signs for $z < z'$. The second part of $\underline{\underline{\mathbf{G}}}_0(\mathbf{r},\mathbf{r}')$ in (8.8) functions like an angular spectrum of both propagating and evanescent plane waves. From (8.5) and (8.8), spectral representations of $\underline{\underline{\mathbf{G}}}_{\mathrm{L}0}$ and $\underline{\underline{\mathbf{G}}}_{\mathrm{R}0}$ are similarly obtained:

$$\left.\begin{aligned}\underline{\underline{\mathbf{G}}}_{\mathrm{L}0}(\mathbf{r},\mathbf{r}') &= -k_0^{-2}\delta(\mathbf{R})\mathbf{u}_z\mathbf{u}_z + \tfrac{i}{4\pi^2}\textstyle\int_{-\infty}^{\infty}\int_{-\infty}^{\infty}\left(k_z^{(0)}\right)^{-1} \\ &\quad\times\exp\left(i\mathbf{k}_{\pm}^{(0)}\cdot\mathbf{R}\right)\mathbf{L}_{\pm}^{(0)}\mathbf{R}_{\pm}^{(0)}\,\mathrm{d}k_x^{(0)}\mathrm{d}k_y^{(0)} \\ \underline{\underline{\mathbf{G}}}_{\mathrm{R}0}(\mathbf{r},\mathbf{r}') &= -k_0^{-2}\delta(\mathbf{R})\mathbf{u}_z\mathbf{u}_z + \tfrac{i}{4\pi^2}\textstyle\int_{-\infty}^{\infty}\int_{-\infty}^{\infty}\left(k_z^{(0)}\right)^{-1} \\ &\quad\times\exp\left(i\mathbf{k}_{\pm}^{(0)}\cdot\mathbf{R}\right)\mathbf{R}_{\pm}^{(0)}\mathbf{L}_{\pm}^{(0)}\,\mathrm{d}k_x^{(0)}\mathrm{d}k_y^{(0)}\end{aligned}\right\}. \tag{8.9}$$

The upper and lower signs in (8.9) are applied in the same way as in (8.8).

By strict analogy with representations of optical beams in Chapter 7, the spectral representations of the remaining DGFs in (8.7) are synthesized as follows:

$$\underline{\underline{\mathbf{G}}}_{\mathrm{L}r}(\mathbf{r},\mathbf{r}') = \frac{i}{4\pi^2}\sum_{n\in\mathbb{Z}}\int_{-\infty}^{\infty}\int_{-\infty}^{\infty}\left(k_z^{(n)}\right)^{-1} \times \exp\left[i\left(\mathbf{k}_-^{(n)}\cdot\mathbf{r}-\mathbf{k}_+^{(0)}\cdot\mathbf{r}'\right)\right]\underline{\underline{\mathfrak{R}}}_{\mathrm{L}}^{(n)}\,\mathrm{d}k_x^{(0)}\mathrm{d}k_y^{(0)}\,, \quad z\le 0\,, \tag{8.10}$$

$$\underline{\underline{\mathbf{G}}}_{\mathrm{R}r}(\mathbf{r},\mathbf{r}') = \frac{i}{4\pi^2}\sum_{n\in\mathbb{Z}}\int_{-\infty}^{\infty}\int_{-\infty}^{\infty}\left(k_z^{(n)}\right)^{-1} \times \exp\left[i\left(\mathbf{k}_-^{(n)}\cdot\mathbf{r}-\mathbf{k}_+^{(0)}\cdot\mathbf{r}'\right)\right]\underline{\underline{\mathfrak{R}}}_{\mathrm{R}}^{(n)}\,\mathrm{d}k_x^{(0)}\mathrm{d}k_y^{(0)}\,, \quad z\le 0\,, \tag{8.11}$$

$$\underline{\underline{\mathbf{G}}}_{\mathrm{L}t}(\mathbf{r},\mathbf{r}') = \frac{i}{4\pi^2}\sum_{n\in\mathbb{Z}}\int_{-\infty}^{\infty}\int_{-\infty}^{\infty}\left(k_z^{(n)}\right)^{-1} \times \exp\left[i\left(\mathbf{k}_+^{(n)}\cdot\tilde{\mathbf{r}}-\mathbf{k}_+^{(0)}\cdot\mathbf{r}'\right)\right]\underline{\underline{\mathfrak{T}}}_{\mathrm{L}}^{(n)}\,\mathrm{d}k_x^{(0)}\,\mathrm{d}k_y^{(0)}\,, \quad z\ge d\,, \tag{8.12}$$

$$\underline{\underline{\mathbf{G}}}_{\mathrm{R}t}(\mathbf{r},\mathbf{r}') = \frac{i}{4\pi^2}\sum_{n\in\mathbb{Z}}\int_{-\infty}^{\infty}\int_{-\infty}^{\infty}\left(k_z^{(n)}\right)^{-1} \times \exp\left[i\left(\mathbf{k}_+^{(n)}\cdot\tilde{\mathbf{r}}-\mathbf{k}_+^{(0)}\cdot\mathbf{r}'\right)\right]\underline{\underline{\mathfrak{T}}}_{\mathrm{R}}^{(n)}\,\mathrm{d}k_x^{(0)}\mathrm{d}k_y^{(0)}\,, \quad z\ge d\,. \tag{8.13}$$

The reflection and transmission dyadics entering (8.10)–(8.13) are given by

$$\left.\begin{aligned}
\underline{\underline{\mathfrak{R}}}_{\mathrm{L}}^{(n)}\left(k_x^{(0)},k_y^{(0)}\right) &= r_{\mathrm{LL}}^{(n)}\,\mathbf{L}_-^{(n)}\mathbf{R}_+^{(0)} + r_{\mathrm{RL}}^{(n)}\,\mathbf{R}_-^{(n)}\mathbf{R}_+^{(0)}\\
\underline{\underline{\mathfrak{R}}}_{\mathrm{R}}^{(n)}\left(k_x^{(0)},k_y^{(0)}\right) &= r_{\mathrm{LR}}^{(n)}\,\mathbf{L}_-^{(n)}\mathbf{L}_+^{(0)} + r_{\mathrm{RR}}^{(n)}\,\mathbf{R}_-^{(n)}\mathbf{L}_+^{(0)}\\
\underline{\underline{\mathfrak{T}}}_{\mathrm{L}}^{(n)}\left(k_x^{(0)},k_y^{(0)}\right) &= t_{\mathrm{LL}}^{(n)}\,\mathbf{L}_+^{(n)}\mathbf{R}_+^{(0)} + t_{\mathrm{RL}}^{(n)}\,\mathbf{R}_+^{(n)}\mathbf{R}_+^{(0)}\\
\underline{\underline{\mathfrak{T}}}_{\mathrm{R}}^{(n)}\left(k_x^{(0)},k_y^{(0)}\right) &= t_{\mathrm{LR}}^{(n)}\,\mathbf{L}_+^{(n)}\mathbf{L}_+^{(0)} + t_{\mathrm{RR}}^{(n)}\,\mathbf{R}_+^{(n)}\mathbf{L}_+^{(0)}
\end{aligned}\right\}. \tag{8.14}$$

These four dyadics are related to the reflected and transmitted plane waves of order n, and are also dependent on the incidence wavevector $\mathbf{k}_+^{(0)}$. The integrands on the right sides of (8.10)–(8.13) are 2D Lebesgue–integrable if the reflection and transmission dyadics in (8.14) are bounded. Therefore, it is possible to carry out integrations in (8.10)–(8.13) numerically. However, in many applications related to far–field radiation, only the asymptotic evaluation of the double radiation integrals in the limit $k_0|\mathbf{r}| \to \infty$ is needed.

8.2 Asymptotic Evaluation

The methods of stationary phase and steepest descent path (SDP) are generally used for asymptotic approximation of integrals [96]–[100]. As for the double integrals, the contours of integration can be deformed to confine the integration on a local domain defined by two local SDPs [98, 99]. The saddle points (or 1st–order critical points) along each SDP can then be utilized to establish the truncated Taylor expansion of the integrand, provided that the integrand term is differentiable on the mapped complex domain [99]. Following this approach, the double integrals in (8.10)–(8.13) can be asymptotically evaluated without any trouble up to the lowest order $\frac{1}{k_0|\mathbf{r}|}$, provided the observation point $\mathbf{r}$ is not close to the boundaries $z = 0$ and $z = d$, i.e., $-\frac{z}{|\mathbf{r}|} > 10\sqrt{\frac{1}{k_0|\mathbf{r}|}}$ for $z < 0$ and $\frac{(z-d)}{|\tilde{\mathbf{r}}|} > 10\sqrt{\frac{1}{k_0|\tilde{\mathbf{r}}|}}$ for $z > d$.

With the source point $\mathbf{r}'$ set equal to $d'\mathbf{u}_z$, $d' < 0$, the lowest–order approximations of the DGFs in (8.10)–(8.13), in the limit $k_0|\mathbf{r}| \to \infty$, turn out to be

$$\underline{\underline{\mathbf{G}}}_{\mathrm{L}r}(\mathbf{r},\mathbf{r}') \simeq \frac{1}{2\pi|\mathbf{r}|}\sum_{n\in\mathbb{Z}} \underline{\underline{\mathfrak{R}}}_{\mathrm{L}}^{(n)}(\alpha_n,\beta_0)\exp\left[i(k_0|\mathbf{r}| - \gamma_n d')\right]\,, \quad z<0\,, \tag{8.15}$$

$$\underline{\underline{\mathbf{G}}}_{\mathrm{R}r}(\mathbf{r},\mathbf{r}') \simeq \frac{1}{2\pi|\mathbf{r}|}\sum_{n\in\mathbb{Z}} \underline{\underline{\mathfrak{R}}}_{\mathrm{R}}^{(n)}(\alpha_n,\beta_0)\exp\left[i(k_0|\mathbf{r}| - \gamma_n d')\right]\,, \quad z<0\,, \tag{8.16}$$

$$\underline{\underline{\mathbf{G}}}_{\mathrm{L}t}(\mathbf{r},\mathbf{r}') \simeq \frac{1}{2\pi|\tilde{\mathbf{r}}|}\sum_{n\in\mathbb{Z}} \underline{\underline{\mathfrak{T}}}_{\mathrm{L}}^{(n)}(\tilde{\alpha}_n,\tilde{\beta}_0)\exp\left[i(k_0|\tilde{\mathbf{r}}| - \tilde{\gamma}_n d')\right]\,, \quad z>d\,, \tag{8.17}$$

$$\underline{\underline{\mathbf{G}}}_{\mathrm{R}t}(\mathbf{r},\mathbf{r}') \simeq \frac{1}{2\pi|\tilde{\mathbf{r}}|}\sum_{n\in\mathbb{Z}} \underline{\underline{\mathfrak{T}}}_{\mathrm{R}}^{(n)}(\tilde{\alpha}_n,\tilde{\beta}_0)\exp\left[i(k_0|\tilde{\mathbf{r}}| - \tilde{\gamma}_n d')\right]\,, \quad z>d\,, \tag{8.18}$$

subject to the restrictions stated in the previous paragraph. In (8.15)–(8.18), $\alpha_n = k_0\frac{x}{|\mathbf{r}|} - n\Lambda_x$ and $\tilde{\alpha}_n = k_0\frac{x}{|\tilde{\mathbf{r}}|} - n\Lambda_x$ are the saddle points along the SDPs of $k_x^{(0)}$ with respect to the reflected and transmitted plane waves of order n, respectively; while $\beta_0 = k_0\frac{y}{|\mathbf{r}|}$ and $\tilde{\beta}_0 = k_0\frac{y}{|\tilde{\mathbf{r}}|}$ are correspondingly the saddle points along the SDPs of $k_y^{(0)}$. The quantities $\gamma_n = +\sqrt{k_0^2 - \alpha_n^2 - \beta_0^2}$ and $\tilde{\gamma}_n = +\sqrt{k_0^2 - \tilde{\alpha}_n^2 - \tilde{\beta}_0^2}$.

8.3 Solution and Analysis

8.3.1 Preliminaries

The response of a slanted chiral STF to radiation by sources comprising electric and magnetic dipoles are considered. As any chiral STF discriminates between LCP and RCP plane waves strongly in the Bragg regime, the following two different Beltrami source configurations can be considered to be canonical:

$$(a)\ \mathbf{W}_{\mathrm{L}} = \tfrac{i\omega\varrho}{2}\mathbf{u}_s\delta(\mathbf{r}' - d'\mathbf{u}_z)\,, \quad \mathbf{W}_{\mathrm{R}} = \mathbf{0}\,, \tag{8.19}$$

$$(b)\ \mathbf{W}_{\mathrm{L}} = \mathbf{0}\,, \quad \mathbf{W}_{\mathrm{R}} = \tfrac{i\omega\varrho}{2}\mathbf{u}_s\delta(\mathbf{r}' - d'\mathbf{u}_z)\,. \tag{8.20}$$

These configurations are of the left– and right–handed types, respectively. Nominally, either configuration is a pair of parallel electric and magnetic dipoles co–located at $\mathbf{r}' = d'\mathbf{u}_z$, $(d' < 0)$, with $\mathrm{Re}[\varrho e^{-i\omega t}]$ being the electric dipole moment. The unit vector $\mathbf{u}_s$ represents the orientation of the dipolar sources. For either configuration, the electric field at observation points far from both the sources and the slanted chiral STF is derived from (8.4) in a normalized form as

$$\mathbf{e}(\mathbf{r}) = \frac{4\pi|\mathbf{r}|\mathbf{E}(\mathbf{r})}{\mu_0\varrho\omega^2}\exp\left(-ik_0|\mathbf{r}|\right)\,. \tag{8.21}$$

Computation of $\mathbf{e}(\mathbf{r})$ was carried out with the same parameters as those in Chapter 4, with $\alpha \in [0, 15^\circ]$ and $n_{hs} = 1$. The dipolar sources were located at $d' = -10\,\lambda_0$, and the far–field radiation patterns were computed at a fixed radial distance $|\mathbf{r}| = 10^5\lambda_0$. Computed values of $|\mathbf{e}(\mathbf{r})|^2$ in the xz and yz planes, for the two Beltrami source configurations, are presented in the remainder of this section.

8.3.2 Response to Parallel Beltrami Source Configurations

Chiral STF

Let $\alpha = 0$ first. The responses of chiral STFs to incident CP plane waves [9, 27] as well as Betrami source configurations [86] have been studied. The most prominent features of the planewave and dipolar responses are due to the circular Bragg phenomenon. With the chosen parameters, the Bragg regime is located at $\lambda_0 \in [702, 752]$ nm for normal planewave incidence; furthermore, the Bragg regime blue–shifts for oblique planewave incidence [27].

Figures 8.2 and 8.3 show plots of $|\mathbf{e}(\mathbf{r})|^2$ in the xz and yz planes for Beltrami source configurations that are oriented parallel (i.e., $\mathbf{u}_s = \mathbf{u}_x$) and perpendicular (i.e., $\mathbf{u}_s = \mathbf{u}_z$), respectively, to the xy plane. The plots for y–directed dipolar sources do not differ qualitatively from those for x–directed sources. The wavelength $\lambda_0 = \lambda_0^{\mathrm{Br}}\Big|_{\theta_i^p=0} = 727$ nm, which is the center–wavelength of the Bragg regime for normal planewave incidence. Evidently, the radiation patterns in Figures 8.2 and 8.3 contain substantial Fabry–Perot rings in the reflection half–space (i.e., $z \leq 0$) which arise due to thickness resonances inside the film. Fabry–Perot rings are also present in the transmission half–space (i.e., $z \geq d$), but are considerably muted [86].

One of the two most interesting features of the radiation patterns in Figure 8.2 is the presence of a wedge along the z axis in the transmission half–space (Figures 8.2(b) and 8.2(d)) for the right–handed (i.e., co–handed) Beltrami source configuration. That wedge is conspicuously absent for the left–handed (i.e., cross–handed) Beltrami source configuration, but a double–fang — the second of the two interesting features — appears in the reflection half–space (Figures 8.2(a) and 8.2(c)). The diversity with respect to the handedness of the source configuration is the cumulative expression of the circular Bragg phenomenon observed with normally [9] and obliquely [27] incident plane waves. As the fields radiated by a Beltrami source configuration can be decomposed into an

angular spectrum of CP plane waves, the angular–spread features of the circular Bragg phenomenon coalesce to create the wedge or the double–fang feature in the radiation pattern.

Although the chiral STF is definitely axially excited by x– and y–directed sources, it is not axially excited when the dipolar sources are z–directed. In the latter case, the dipolar radiation is broadside, not endfire [101]. Therefore, the radiation patterns in Figure 8.3 do not contain evidence of the circular Bragg phenomenon in the form of substantially diverse responses of the chiral STF to the two Beltrami source configurations.

Slanted Chiral STF

For slanted chiral STFs, $\alpha \neq 0$. Figures 8.4 and 8.5 show the dipolar radiation patterns in the presence of the slanted chiral STF with $\alpha = 5^\circ$, when $\mathbf{u}_s = \mathbf{u}_x$ and $\mathbf{u}_s = \mathbf{u}_y$, respectively. The wavelength was chosen $\lambda_0 = \lambda_0^{\text{Br}}\Big|_{\theta_i^p=0} = 724$ nm for $\alpha = 5^\circ$. The characteristic features of these radiation patterns are tailored by the circular Bragg phenomenon discussed in Chapters 3 and 4 for the slanted chiral STF. Noticeably, both (i) the wedge in the transmission half–space for the co–handed Beltrami source configuration and (ii) the double–fang in the reflection half–space for the cross–handed Beltrami source configuration are located asymmetrically in the xz plane about the z axis. In contrast, the radiation patterns are symmetric in the yz plane about the z axis, just as for the chiral STF. The reason seems clear by virtue of the fact that the circular Bragg phenomenon is significantly circularly asymmetric about the z axis and sensitive to the plane of planewave incidence when $\alpha \neq 0$. No wonder, there is a vast difference between the radiation pattern in the xz plane for $\mathbf{u}_s = \mathbf{u}_x$ (Figure 8.4(b)) and that in the yz plane for $\mathbf{u}_s = \mathbf{u}_y$ (Figure 8.5(d)).

In order to interpret the radiation patterns further, let the angle $\zeta_\rho \in [-180^\circ, 180^\circ)$ be

introduced and determined by

$$\frac{\mathbf{r}}{|\mathbf{r}|} = \begin{cases} \mathbf{u}_x \cos\zeta_\rho + \mathbf{u}_z \sin\zeta_\rho \,, & \mathbf{r} \bullet \mathbf{u}_y = 0 \\ \mathbf{u}_y \cos\zeta_\rho + \mathbf{u}_z \sin\zeta_\rho \,, & \mathbf{r} \bullet \mathbf{u}_x = 0 \end{cases} . \tag{8.22}$$

In Figures 8.4(b) and 8.5(b), the wedge is centered at $\zeta_\rho < 90^\circ$; but it is centered at $\zeta_\rho = 90^\circ$ in Figures 8.4(d) and 8.5(d). The reason is that, although the circular Bragg phenomenon shifts in the $+\theta_i^p$ direction as $|\alpha|$ increases in the plane of incidence $\psi_i^p = 0$, it does not shift at all in the plane of incidence $\psi_i^p = 90^\circ$, as indicated in Figure 4.3.

Even though the dominant remittances for an incident cross–handed CP plane wave are always specular — as exemplified by Figure 4.2 — the double–fangs in Figures 8.4(a) and 8.5(a) have rotated counterclockwise with respect to that in Figure 8.2(a) These three figures contain the radiation patterns in the xz plane; while the corresponding radiation patterns in the yz plane (in Figures 8.2(c), 8.4(c), and 8.5(c)) are symmetric with respect to the z axis, regardless of the value of α. The attributes of the circular Bragg phenomenon *versus* $\alpha \neq 0$ — as indicated in Figure 4.3 — also explain the foregoing features of the radiation patterns.

An increase in $|\alpha|$ can affect the wedge and the double–fang feature even more drastically than in Figures 8.4 and 8.5, for which $\alpha = 5^\circ$. For example, when α rises to 10°, Figure 8.6 shows that the wedge expands and rotates clockwise so much that there is no transmission for $\zeta_\rho \in (0, 90^\circ)$ in the xz plane — when the Beltrami source configuration is co–handed and x–directed.

The circular Bragg phenomenon being frequency–selective, the wavelength of radiation in relation to the Bragg regime also affects the radiation pattern. Clearly, because of the blue–shift of the Bragg regime for oblique incidence, the wedge and the double–fang tend to be obliquely oriented when λ_0 is lower than $\lambda_0^{\mathrm{Br}}\Big|_{\theta_i^p=0}$. This is exemplified by the radiation patterns in Figure 8.7 for which $\lambda_0 = 670$ nm, and the Beltrami source configuration is co–handed and x–directed. The wedge is located in the yz plane in the ζ_ρ–neighborhoods

of both 45° and 135° for $\alpha = 5°$ (Figure 8.7(b)) and $\alpha = 10°$ (Figure 8.7(d)) as well.

Incidentally, in Figure 8.7(c), enhanced radiation is evident in the xz plane, near the surface of the slanted chiral STF for $\alpha = 10°$. Unfortunately, the computation does not seem to be accurate because the asymptotic evaluation procedure is invalid in the vicinity of the slanted chiral STF.

8.3.3 Response to Perpendicular Beltrami Source Configurations

Because the fields emitted by a perpendicular dipolar source (i.e., $\mathbf{u}_s = \mathbf{u}_z$) are of the end–fire type with respect to the slanted chiral STF, the radiation patterns may not evince any trace of the circular Bragg phenomenon when $|\alpha|$ is small — as suggested by the limiting case of $\alpha = 0$ in Figure 4. However, for larger $|\alpha|$, a significant broadside aspect to the interaction between the dipolar source and the thin film is possible. Figure 8.8 presents the radiation patterns for $\alpha = 15°$ and z–directed dipolar sources radiating at $\lambda_0 = \lambda_0^{\mathrm{Br}}\Big|_{\theta_i^p=0} = 702$ nm. Although the plots labeled (a), (c), and (d) in Figure 8.8 look very similar to their counterparts in Figure 8.3 ($\alpha = 0$), a contrast between Figures 8.3(b) and 8.8(b) is evident. A wedge is located in the regime $\zeta_\rho \in (0, 45°)$ in Figure 8.8(b), but not in Figure 8.3(b). Thus, even for perpendicular Beltrami source configurations, the circular Bragg phenomenon can come into play when $\alpha \neq 0$.

8.4 Concluding Remarks

In conclusion,

- the appearance of either wedge or double–fang in radiation patterns, and
- the radiation spread being spatially asymmetric for $\alpha \neq 0$

are two remarkable features of the dipolar response of slanted chiral STFs.

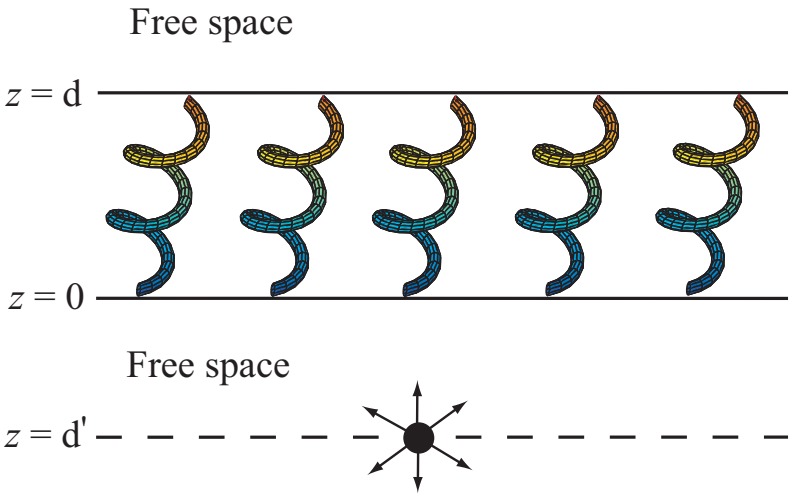

Figure 8.1: Schematic of the irradiation of a slanted chiral STF of thickness d by a dipolar source located at $\mathbf{r}' = \mathbf{d}'\mathbf{u}_z$, $d' < 0$.

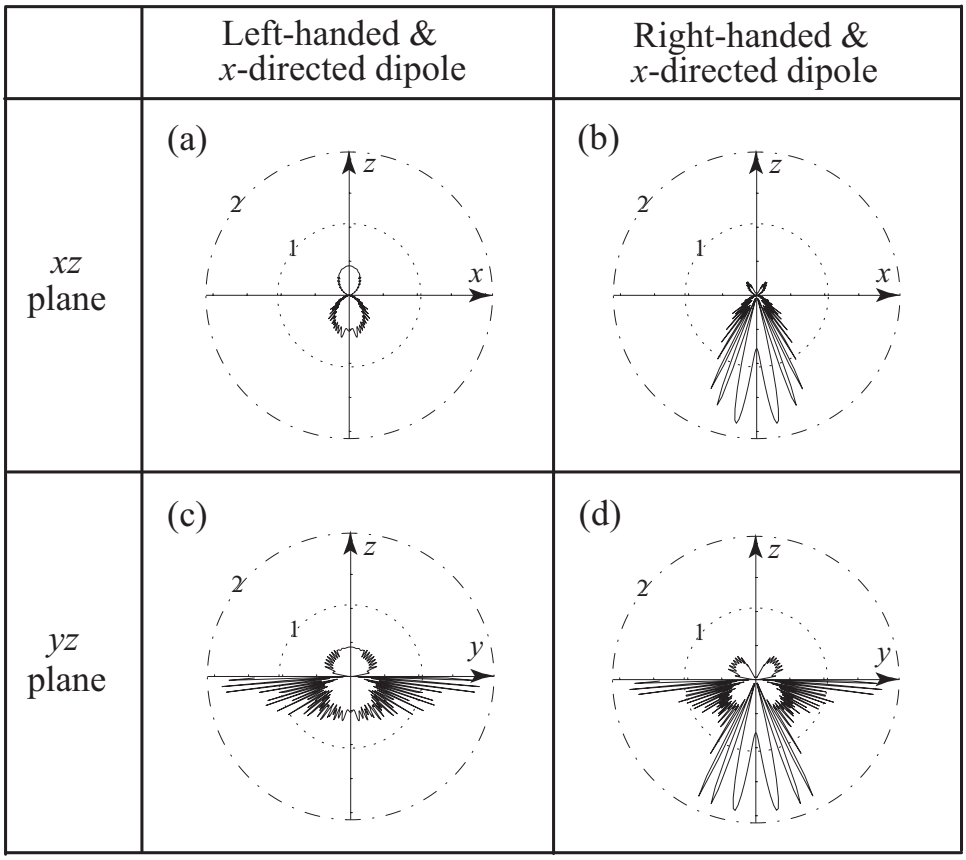

Figure 8.2: Computed values of $|\mathbf{e}(\mathbf{r})|^2$ in the xz and yz planes, for x–directed Beltrami source configurations radiating at $\lambda_0 = \lambda_0^{\mathrm{Br}}\Big|_{\theta_i^p=0} = 727$ nm in the presence of a structurally right–handed chiral STF. The Beltrami source configuration is left–handed for the left plots (a, c), and right–handed for the right plots (b, d). Whereas $d' = -10\,\lambda_0$ and $|\mathbf{r}| = 10^5\lambda_0$; see Figure 4.1 for other parameters.

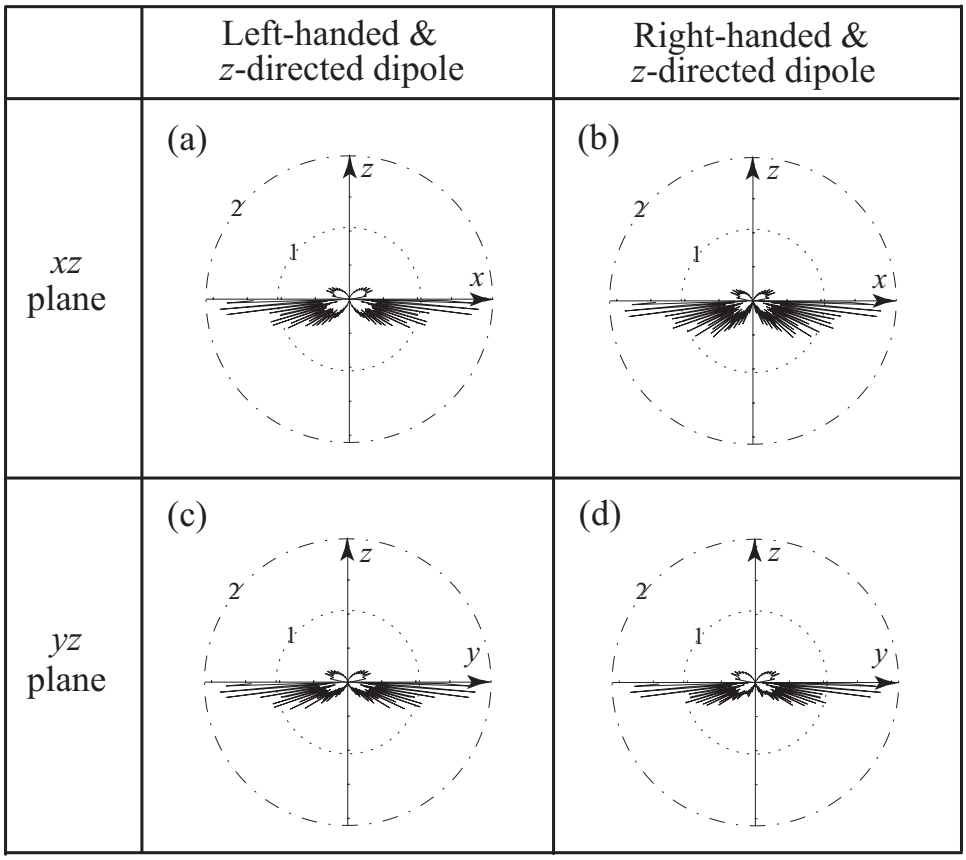

Figure 8.3: Same as Figure 8.2, but for z–directed Beltrami source configurations.

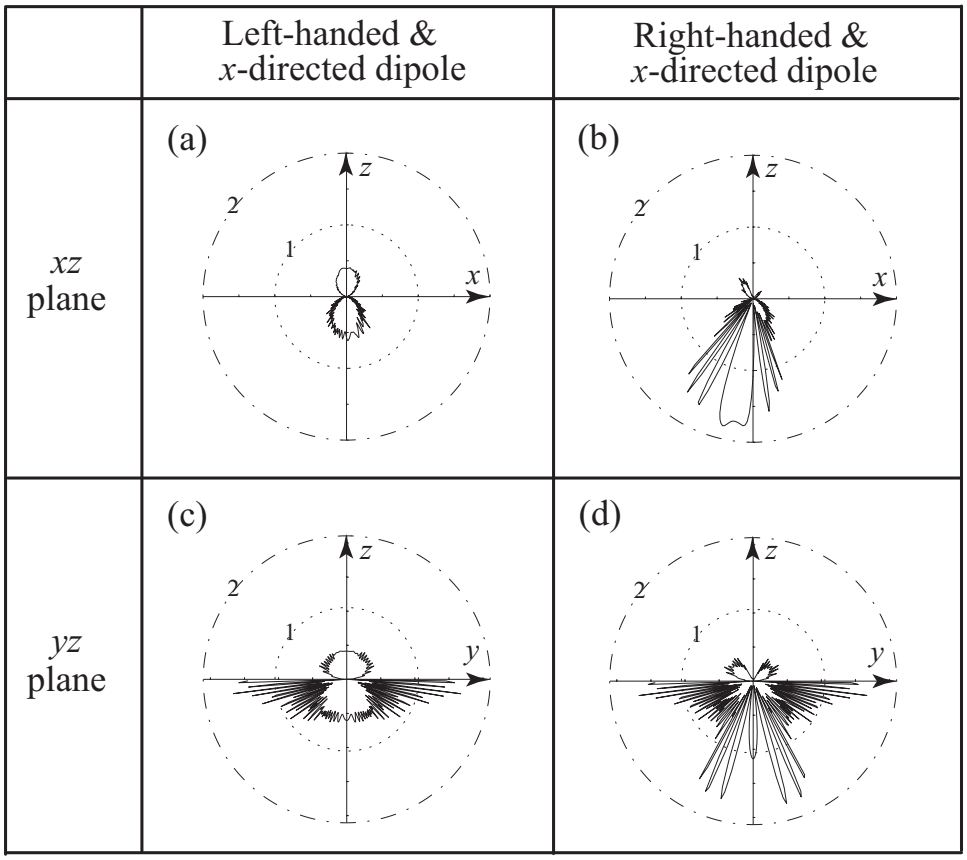

Figure 8.4: Same as Figure 8.2, but for $\alpha = 5^\circ$ and $\lambda_0 = \lambda_0^{\mathrm{Br}}\Big|_{\theta_i^p} = 724$ nm.

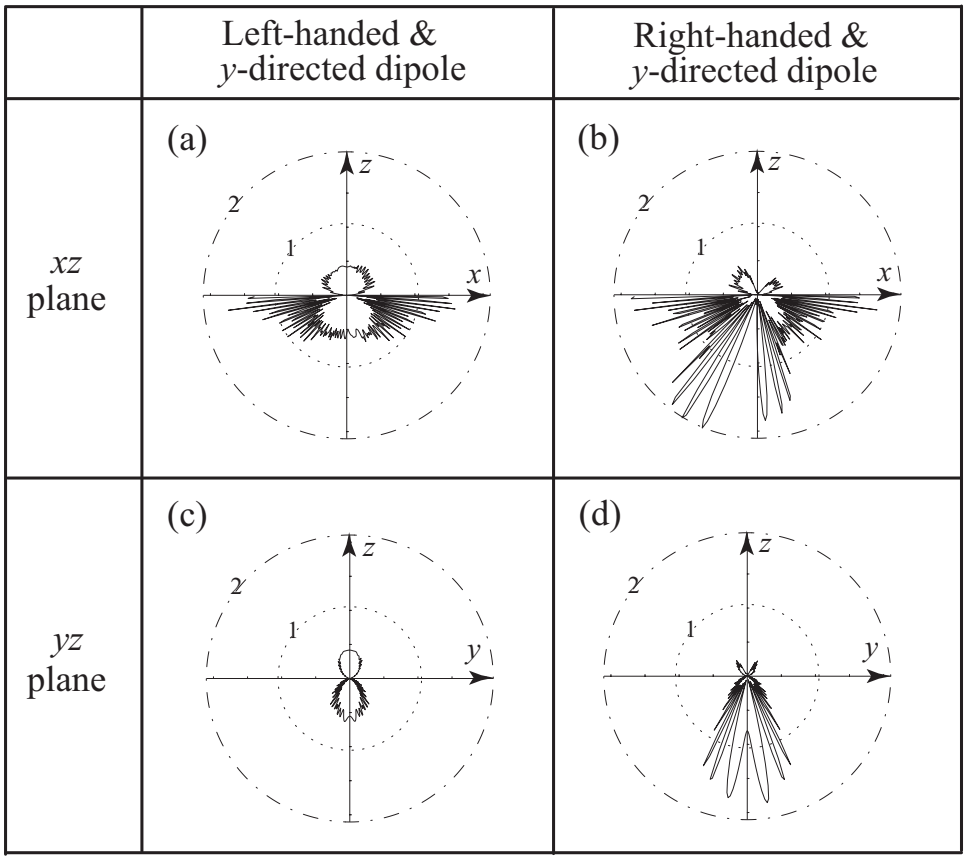

Figure 8.5: Same as Figure 8.4, but for y–directed Beltrami source configurations.

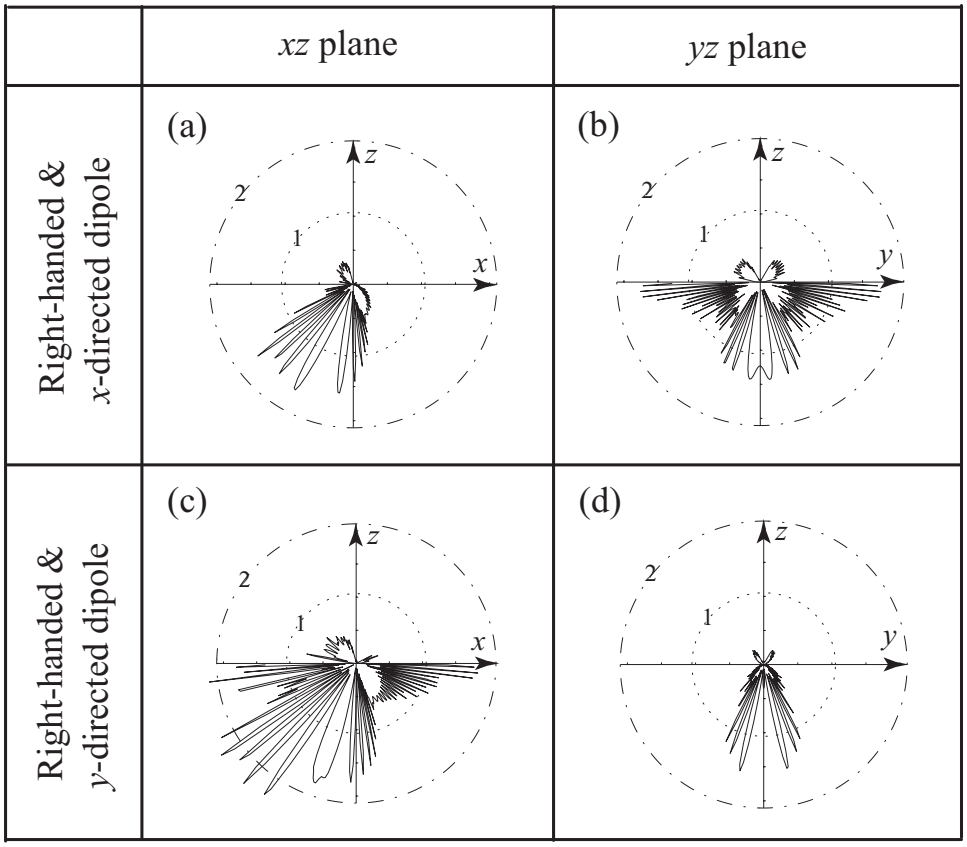

Figure 8.6: Computed values of $|\mathbf{e}(\mathbf{r})|^2$ in the xz and yz planes, for right–handed Beltrami source configuration radiating at $\lambda_0 = \lambda_0^{\mathrm{Br}}\Big|_{\theta_i^p=0} = 716$ nm. The Beltrami source configuration is (a, b) x–directed, and (c, d) y–directed. The slant angle $\alpha = 10°$; see Figure 8.4 for other parameters.

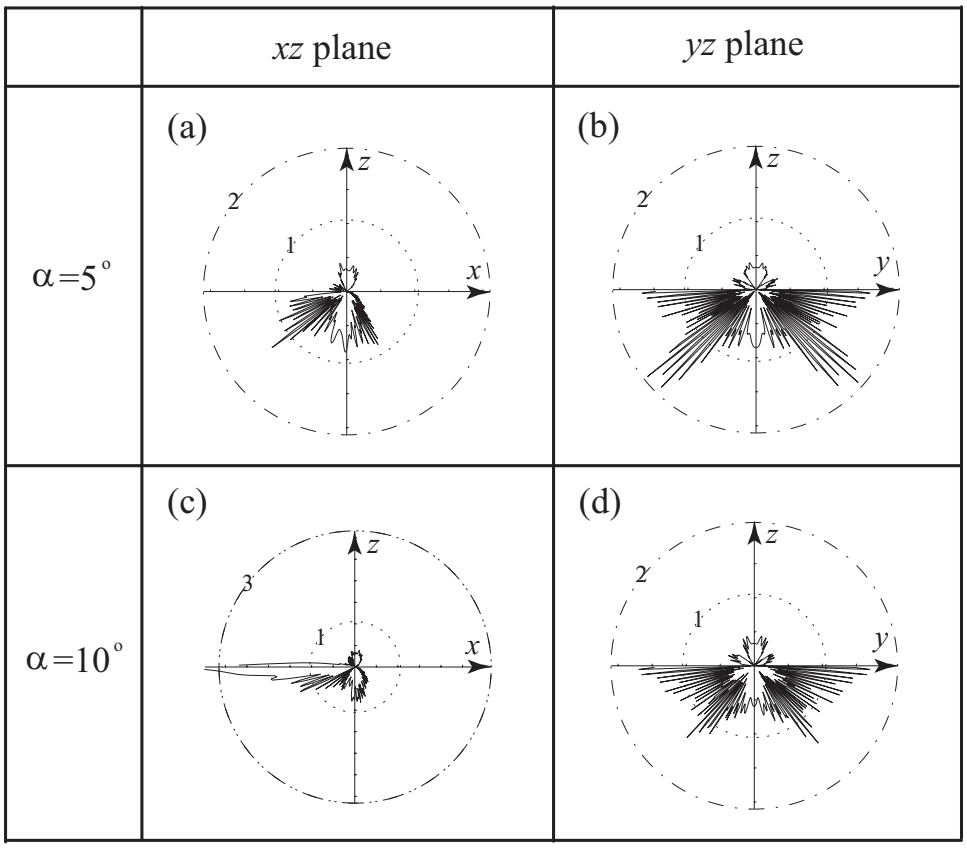

Figure 8.7: Computed values of $|\mathbf{e}(\mathbf{r})|^2$ in the xz and yz planes, for a x–directed, right–handed, Beltrami source configuration radiating at $\lambda_0 = 670$ nm. (a, b) $\alpha = 5°$ and (c, d) $\alpha = 10°$. See Figure 8.4 for other parameters.

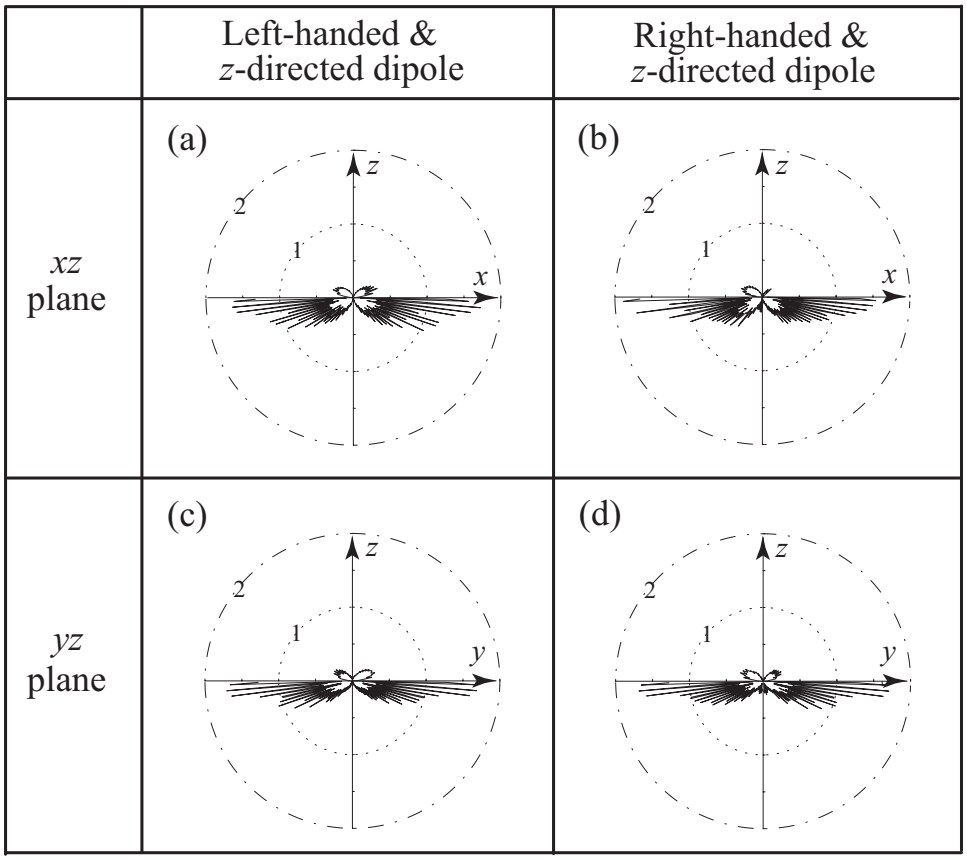

Figure 8.8: Same as Figure 8.3, but for $\alpha = 15^\circ$ and $\lambda_0 = \lambda_0^{\mathrm{Br}}\Big|_{\theta_i^p=0} = 702$ nm.

Chapter 9

Conclusion

In this thesis, slanted chiral STFs were proposed to couple the characteristic optical responses of volume and diffraction gratings in thin films. The optical framework for slanted chiral STFs was substantiated by theoretical investigations of the optical responses of these nanomaterials to several types of excitation sources, such as plane waves, optical beams, and dipoles. A robust numerical solution procedure was devised in Chapter 2 for computation of planewave diffraction by slanted chiral STFs. This numerical solution procedure was applied to determine the planewave response of slanted chiral STFs in Chapters 3 and 4, respectively, under normal–incidence and oblique–incidence conditions. The same solution procedure was employed to analyze the optical response of a slanted chiral STF with a central twist defect in Chapter 5. A remarkable crossover phenomenon was found in slanted chiral STFs for a wave resonance initiated by the twist defect. The genesis of the crossover phenomenon in chiral STFs was mathematically elucidated in Chapter 6, by an application of the coupled–wave theory.

The next step of theoretical investigations involved planewave representations of optical beams and dipole radiations. An optical beam was represented as an angular spectrum of plane waves; while the dipolar radiation was formulated in terms of spectral representations

of dyadic Green functions. Then, the response of slanted chiral STFs to optical beams was examined in Chapter 7, with emphasis on lateral shifts of optical beams on reflection. Finally, the radiation pattern of a dipolar source in the presence of a slanted chiral STF was presented in Chapter 8. The conclusions drawn from the studies discussed in the preceding chapters are summarized in the following sections.

9.1 Response of Slanted Chiral STFs to Plane Waves

- The circular Bragg phenomenon becomes partly nonspecular when the slant angle $\alpha \neq 0$, such that the co–handed Bragg reflection occurs in the Floquet–harmonic of order $n = \pm 2$ for $\alpha \gtrless 0$. This characteristic can be harnessed to design slanted chiral STFs as circular–polarization beamsplitters and couplers.

- The Bragg regime blue–shifts as $|\alpha|$ increases, and the width of the Bragg regime decreases to zero due to the influence of a Rayleigh–Wood anomaly of order $n = \pm 2$ for $\alpha \gtrless 0$.

- The angular spread of the Bragg regime is significantly asymmetric because of the subversion of the circular Bragg phenomenon by the Rayleigh–Wood anomaly.

- The angular spread is affected by the refractive index n_{hs} of the ambient dielectric medium, such that it is highly constrained by the occurrence of total reflection.

9.2 Spectral Holes in Slanted Chiral STFs

In the presence of a central twist defect, spectral holes emerge within the Bragg regime, thereby indicating the occurrence of wave resonance therein. The remarkable features of the spectral holes are as follows:

- Two types of spectral holes are excitable by circularly polarized plane waves — one is the co–handed reflectance hole, and the second is the cross–handed transmittance hole.

- There is a crossover phenomenon associated with the evolution of the two types of spectral holes with the increase of thickness of the chiral STF: When the thickness is small, a co–handed reflectance hole occurs in the Bragg regime; as the thickness increases, the co–handed reflectance hole diminishes to vanish eventually, and is replaced by a cross–handed transmittance hole.

- The bandwidth of the cross–handed transmittance hole is significantly smaller than that of the co–handed reflectance hole.

- The co–handed reflectance hole is nonspecular for $\alpha \neq 0$, while the cross–handed transmittance hole is always specular.

- The spectral holes occur in the center of the Bragg regime, when the twist angle $\phi = \frac{m_o \pi}{2}$ (m_o is an odd integer); they are shifted towards the edges of the Bragg regime when $\phi \neq \frac{m\pi}{2}$ ($m \in \mathbb{Z}$).

- The spectral holes are accompanied by the spectral peaks in the corresponding transmittance and reflectance spectrums. In contrast to the co–handed transmittance peak which is always specular for $\alpha \neq 0$, the cross–handed reflectance peak happens in Floquet harmonics of different orders as $\alpha \neq 0$ changes.

- Even for weakly dissipative slanted chiral STFs, the cross–handed hole is accompanied by substantial attenuation in transmission.

9.3 Analytic Approach to the Crossover Phenomenon in Chiral STFs

An approximate but closed–form solution for axial wave propagation in a chiral STF with a central 90°–twist defect is obtained in terms of a CWT 4×4 transmission matrix.

- The genesis of the crossover phenomenon in the chiral STF is mathematically elucidated by the spectral characteristics of the transmission matrix: As it can be decomposed into two terms, the first term favors total transmission in the middle of the Brag regime, while the second term favors total reflection in the whole Bragg regime. When the thickness of the chiral STF is relatively small, the first term dominates and gives rise to a co–handed reflectance hole in the center of Bragg regime. As the thickness of the chiral STF increases, the second term becomes significant and interferes with the first term such that the transmission matrix is isomorphic to that of a defect–free chiral STF — except in a tiny wavelength–regime ($\lambda_0 = \lambda^p_{0_{\mathrm{CWT}}}$) wherein the two terms become identical to each other in the L_∞–norm sense to engender the total–reflection feature. Hence, the co–handed reflectance hole diminishes to vanish eventually as the thickness increases, and is replaced by a cross–handed transmittance hole.

- The bandwidth of the cross–handed transmittance hole, although saturated for the thickness beyond the crossover value, increases exponentially with the local birefringence. In contrast, the bandwidth of the co–handed reflectance hole, which increases exponentially with the thickness, increases linearly with the local birefringence.

9.4 Lateral Shifts of Optical Beam on Reflection by Slanted Chiral STFs

There are two types of lateral shifts of optical beams on reflection by slanted chiral STFs. One is the lateral shift of a co–handed optical beam that is mostly reflected due to the circular Bragg phenomenon. The other is the Goos–Hänchen shift that occurs when the beam is totally reflected. Four remarkable features of the two types of lateral shifts of optical beams are as follows:

- The lateral shift of a co–handed beam on Bragg reflection can be either forward or backward when $\alpha \neq 0$, depending on the directionality of incidence.
- The Goos–Hänchen shift is affected by both slantedness and structural handedness of the slanted chiral STF, when the post–critical angle of incidence (i.e., $|\theta_i^b| \geq \theta_{ic}^b$) is small.
- When the incident beam is circularly polarized and three–dimensional, both in–plane and out–of–plane Goos–Hänchen shifts occur on total reflection. In particular, the out–of–plane Goos–Hänchen shift increases in amplitude as the angle of incidence decreases, and it can be either forward or backward.
- Lateral shift of each type at low–ultraviolet and longer wavelengths is large enough in magnitude to be significant for nanotechnology.

9.5 Response of Slanted Chiral STFs to Dipolar Radiation

The dipolar response of slanted chiral STFs to Beltrami source configurations is characterized in terms of the radiation pattern in the far–field limit. The remarkable features of the radiation pattern are as follows:

- Wedge and double–fang features appear in the radiation pattern, which expresses the spatial sense of the circular Bragg phenomenon.

- The radiation spread is spatially asymmetric for $\alpha \neq 0$, and wedge and double–fang features rotate towards the horizontal direction as $|\alpha|$ increases.

9.6 Future Work

Now that the concept of slanted chiral STFs has been proposed and its optical ramifications examined, experimental realization of this type of nanomaterials is needed. Along with that, slanted chiral STFs need to be characterized experimentally to obtain accurate constitutive data for different deposited materials. Both microscopic and phenomenological models for structure–property relationships need to be verified experimentally. Experimental studies of the optical response of slanted chiral STFs are to be carried out to demonstrate the coupling of two types of optical periodicities in these nanomaterials.

As of now, slanted chiral STFs have not been fabricated. It is possible that actual slanted chiral STFs may not conform exactly to (1.15). However, the rigorous coupled–wave analysis of Chapter 2 is robust enough to accommodate χ_s as a periodic function along the helical axis. Furthermore, such a change is not going to qualitatively influence the deleterious effect of Rayleigh–Wood anomaly on the circular Bragg phenomenon, as delineated in this thesis.

Further research is warranted for the development of optical devices for slanted chiral STFs. The uses of slanted chiral STFs as optical beamsplitters and couplers, spectral–hole filters, and biosensors have been suggested in this thesis, and need to be implemented experimentally.

Photonic–band–gap materials can be formed by lithographically patterning slanted chiral STFs on 2D regular lattices. Therefore, photonic waveguides and fibers and lasers

can be designed on the architecture of slanted chiral STFs.

Finally, slanted chiral STFs as optical pulse–shapers require investigation. Due to the circular Bragg phenomenon, a femtosecond CP pulsed beam of finite spectral width has the possibility to experience the temporal superresolution on transmission throughout the slanted chiral STF [102]. As a result, femtosecond pulse compression will happen, which should be circular–polarization–sensitive.

Bibliography

[1] A. Lakhtakia, R. Messier, *Sculptured Thin Films: Nanoengineered Morphology and Optics* (SPIE Press, Bellingham, WA, 2005)

[2] H. A. Macleod, *Thin–film Optical Filters* (Institue of Physics, Bristol, UK, 2001)

[3] I. J. Hodgkinson, Q. h. Wu, *Birefringent Thin Films and Polarizing Elements* (World Scientific, Singapore, 1997)

[4] A. Lakhtakia, "Sculptured thin films: accomplishments and emerging uses", Mater. Sci. Eng. C **19** 427–434 (2001).

[5] I. J. Hodgkinson, Q. h. Wu, "Inorganic chiral optical materials", Adv. Mater. **13** 889–897 (2001).

[6] A. Lakhtakia, R. Messier, "The past, the present, and the future of sculptured thin films", in: W. S. Weiglhofer, A. Lakhtakia (eds.), *Introduction to Complex Mediums for Optics and Electromagnetics* SPIE Press PM123 (2003).

[7] A. Lakhtakia, R. Messier, "Sculptured thin films—I. Concepts", Mater. Res. Innovat. **1** 145–148 (1997).

[8] R. Messier, A. Lakhtakia, "Sculptured thin films—II. Experiments and applications", Mater. Res. Innovat. **2** 217–222 (1999).

[9] V. C. Venugopal, A. Lakhtakia, "Sculptured thin films: Conception, optical properties, and applications", in: O.N. Singh, A. Lakhtakia (eds.), *Electromagnetic Fields in Unconventional Materials and Structures* 151–216 (Wiley, New York, 2000).

[10] M. Suzuki, Y. Taga, "Integrated sculptured thin films", Jpn. J. Appl. Phys. Pt. 2 **40** L358–L359 (2001).

[11] M. W. Horn, M. D. Pickett, R. Messier, A. Lakhtakia, "Blending of nanoscale and microscale in uniform large–area sculptured thin–film architectures", Nanotechnology **15** 303–310 (2004).

[12] J. A. Thornton, "High rate thick film growth", Ann. Rev. Mat. Sci. **7** 239–260 (1977).

[13] V. C. Venugopal, A. Lakhtakia, "Low–permittivity nanocomposite materials using sculptured thin film technology", J. Vac. Sci. Technol. B **18** 32–36 (2000).

[14] A. Lakhtakia, "On determing gas concentration using thin–film helicoidal bianisotropic medium bilayers", Sens. Actuat. B: Chem. **52**, 243–250 (1998).

[15] A. Lakhtakia, M. W. McCall, J. A. Sherwin, Q. H. Wu, I. J. Hodgkinson, "Sculptured–thin–film spectral holes for optical sensing of fluids", Opt. Commun. **194** 33–46 (2001).

[16] J. A. Sherwin, A. Lakhtakia, "Nominal model for structure–property relations of chiral dielectric sculptured thin films", Math. Comput. Model. **34** 1499–1514 (2001); corrections: **35** 1355–1363 (2002).

[17] J. A. Sherwin, A. Lakhtakia, "Nominal model for the optical response of a chiral sculptured thin film infiltrated with an isotropic chiral fluid", Opt. Commun. **214** 231–245 (2002).

[18] J. A. Sherwin, A. Lakhtakia, I. J. Hodgkinson, "On calibration of a nominal structure–property relationship model for chiral sculptured thin films by axial transmittance measurements", Opt. Commun. **209** 369–375 (2002).

[19] J. A. Sherwin, A. Lakhtakia, "Nominal model for the optical response of a chiral sculptured thin film infiltrated by an isotropic chiral fluid—oblique incidence", Opt. Commun. **222** 305–329 (2003).

[20] R. Messier, T. Gehrke, C. Frankel, V. C. Venugopal, W. Otaño, A. Lakhtakia, "Engineered sculptured nematic thin films", J. Vac. Sci. Technol. A **15** 2148–2152 (1997).

[21] N. O. Young, J. Kowal, "Optically active fluorite films", Nature **183** 104–105 (1959).

[22] K. Robbie, M. J. Brett, A. Lakhtakia, "First thin film realization of a helicoidal bianisotropic medium", J. Vac. Sci. Technol. A **13** 2991–2993 (1995).

[23] M. D. Pickett, A. Lakhtakia, "On gyrotropic chiral sculptured thin films for magneto–optics", Optik **113** 367–371 (2002).

[24] A. Lakhtakia, "On the genesis of Post constraint in modern electromagnetism", Optik **115** 151–158 (2004).

[25] C. M. Krowne, "Electromagnetic theorems for complex anisotropic media", IEEE Trans. Antennas Propagat. **32** 1224–1230 (1984).

[26] A. Lakhtakia (ed.), *Selected Papers on Linear Optical Composite Materials* (SPIE Press, Bellingham, WA, 1996).

[27] V. C. Venugopal, A. Lakhtakia, "Electromagnetic plane–wave response characteristics of non–axially excited slabs of dielectric thin–film helicoidal bianisotropic mediums", Proc. R. Soc. Lond. A **456** 125–161 (2000).

[28] V. C. Venugopal, A. Lakhtakia, "On absorption by non–axially excited slabs of dielectric thin–film bianisotropic mediums", Eur. J. Phys. Appl. Phys. **10** 173–184 (2000).

[29] M. D. Pickett, A. Lakhtakia, J. A. Polo, "Spectral responses of gyrotropic chiral sculptured thin films to obliquely incident plane waves", Optik, **115** 393–398 (2004).

[30] M. W. McCall, A. Lakhtakia, "Development and assessment of coupled wave theory of axial propagation in thin–film helicoidal bianisotropic media. Part 1: reflectances and transmittances", J. Mod. Opt. **47** 973–991 (2000); corrections: **50** 2807 (2003).

[31] M. W. McCall, "Axial electromagnetic wave propagation in inhomogeneous dielectrics", Math. Comput. Model. **34** 1483–1497 (2001).

[32] M. W. McCall, A. Lakhtakia, "Explicit expressions for spectral remittances of axially excited chiral sculptured thin films", J. Mod. Opt. **51** 111–127 (2004).

[33] Q. Wu, I. J. Hodgkinson, A. Lakhtakia, "Circular polarization filters made of chiral sculptured thin films: Experiments and simulation results", Opt. Eng. **39** 1863–1868 (2000).

[34] A. Lakhtakia, "Dielectric sculptured thin films for polarization–discriminatory handedness–inversion of circularly polarized light", Opt. Eng. **38** 1596–1602 (1999).

[35] I. J. Hodgkinson, A. Lakhtakia, Q. h. Wu, "Experimental realization of sculptured–thin–film polarization–discriminatory light–handedness inverters", Opt. Eng. **39** 2831–2834 (2000).

[36] I. J. Hodgkinson, Q. h. Wu, A. Lakhtakia, M. W. McCall, "Spectral–hole filter fabricated using sculptured thin–film technology", Opt. Commun. **177** 79–84 (2000).

[37] I. J. Hodgkinson, Q. H. Wu, K. E. Thorn, A. Lakhtakia, M. W. McCall, "Spacerless circular–polarization spectral–hole filters using chiral sculptured thin films: theory and experiment", Opt. Commun. **184** 57–66 (2000).

[38] F. Wang, A. Lakhtakia, R. Messier, "Towards piezoelectrically tunable chiral sculptured thin film lasers", Sens. Actuat. A **102** 31–35 (2002).

[39] J. B. Geddes III, A. Lakhtakia, "Reflection and transmisstion of optical narrow–extent pulses by axially excited chiral sculptured thin films", Eur. Phys. J. Appl. Phys. **13** 3–14 (2001); corrections: **16** 247 (2001).

[40] J. B. Geddes III, A. Lakhtakia, "Pulse–coded information transmission across an axially excited chiral sculptured thin film in the Bragg regime", Microwave Opt. Technol. Lett. **28** 59–62 (2001).

[41] A. T. Wu, M. Seto, M. J. Brett, "Capacitive SiO humidity sensors with novel microstructures", Sens. Mater. **11** 493–505 (2000).

[42] E. E. Steltz, A. Lakhtakia, "Theory of second–harmonic–generated radiation from chiral sculptured thin films for bio–sensing", Opt. Commun. **216** 139–150 (2003).

[43] J. M. Jarem, P. P. Banerjee, *Computational Methods for Electromagnetic and Optical Systems* (Marcel Dekker, New York, 2000).

[44] D. Maystre (ed.), *Selected Papers on Diffraction Gratings* (SPIE Press, Bellingham, WA, 1993).

[45] A. Lakhtakia, V. K. Varadan, V. V. Varadan, "Scattering by periodic achiral–chiral interfaces", J. Opt. Soc. Am. A **6** 1675–1681 (1989); corrections: **7** 951 (1990).

[46] F. Wang, A. Lakhtakia, R. Messier, "Coupling of Rayleigh–Wood anomalies and the circular Bragg phenomenon in slanted chiral sculptured thin films", Eur. Phys. J. Appl. Phys. **20** 91–103 (2002).

[47] R. Messier, V. C. Venugopal, P. D. Sunal, "Origin and evolution of sculptured thin films", J. Vac. Sci. Technol. B **18** 1538–1545 (2000).

[48] R. Messier, A. Lakhtakia, V. C. Venugopal, P. D. Sunal, "Sculptured thin films: Engineered nanostructural materials", Vac. Technol. Coating **2** (10) 40–47 (October 2001).

[49] F. de Fornel, *Evanescent Waves From Newtonian Optics to Atomic Optics* (Springer, Heidelberg, Germany, 2001).

[50] M. A. Paesler, P. J. Moyer, *Near–Field Optics: Theory, Instrumentation, and Application* (Wiley, New York, 1996).

[51] A. Naber, H. Kock, H. Fuchs, "High–resolution lithography with near–field optical microscopy", Scanning **18** 567–571 (1996).

[52] S. Kühn, C. Hettich, C. Schmitt, J. P. Poizat, V. Sandoghdar, "Diamond colour centres as a nanoscopic light source for scanning near–field optical microscopy", J. Microscopy **202** 2–6 (2001).

[53] H. A. Haus, C. V. Shank, "Antisymmetric taper of distributed feedback lasers", IEEE J. Quantum Electron. **12** 532–539 (1974).

[54] E. Yablonovitch, "Inhibited spontaneous emission in solid–state physics and electronics", Phys. Rev. Lett. **58** 2059–2062 (1987).

[55] J. Schmidtke, W. Stille, H. Finkelmann, "Defect mode emission of a dye doped cholesteric polymer network", Phys. Rev. Lett. **90** 083902 (2003).

[56] I. J. Hodgkinson, Q. h. Wu, L. De Silva, M. Arnold, M. W. McCall, & A. Lakhtakia, "Supermodes of chiral photonic filters with combined twist and layer defects", Phys. Rev. Lett. **91** 223903 (2003).

[57] V. I. Kopp, A. Z. Genack, "Twist defect in chiral photonic structures", Phys. Rev. Lett. **89** 033901 (2002).

[58] M. Becchi, S. Ponti, J. A. Reyes, C. Oldano, "Defect mode in helical photonic crystals: An analytic approach", Phys. Rev. B. **70** 033103 (2004).

[59] J. Schmidtke, W. Stille, "Photonic defect modes in cholesteric liquid crystal films", Eur. Phys. J. E **12** 553–564 (2003).

[60] E. N. Glytsis, T. K. Gaylord, "Rigorous three–dimensional coupled–wave diffraction analysis of single and cascaded anisotropic gratings", J. Opt. Soc. Am. A **4** 2061–2080 (1987).

[61] L. Li, C. W. Haggans, "Convergence of the coupled–wave method for metallic lamellar diffraction gratings", J. Opt. Soc. Am. A **10** 1184–1187 (1993).

[62] H. K. V. Lotsh, "Beam displacement at total reflection: the Goos–Hänchen shift, I", Optik **32** 116–137 (1970).

[63] A. Lakhtakia, "Truncation of angular spread of Bragg zones by total reflection, and Goos–Hänchen shifts exhibited by chiral sculptured thin films", Int. J. Electron. Commun. (AEÜ) **56** 169–176 (2002); corrections: **57** 79 (2003).

[64] C. Kittel, *Introduction to Solid State Physics* 4th ed. (Wiley Eastern, New Delhi, India, 1974) Chap. 13.

[65] A. Lakhtakia, "Spectral signatures of axially excited slabs of dielectric thin-film helicoidal bianisotropic mediums", Eur. Phys. J. Appl. Phys. **8** 129–137 (1999).

[66] N. Chateau, J. Hugonin, "Algorithm for the rigorous coupled–wave analysis of grating diffraction", J. Opt. Soc. Am. A **11** 1321–1331 (1994).

[67] H. Hochstadt, *Differential Equations: A Modern Approach* (Dover Press, New York, 1975).

[68] H. Lütkepohl, *Handbook of Matrices.* (Wiley, Chicester, UK, 1996).

[69] L. Li, "Multilayer modeal method diffraction gratings of arbitrary profile, depth, and permittivity", J. Opt. Soc. Am. A **10** 2581–2591 (1993).

[70] M. G. Moharam, E. B. Grann, D. A. Pommet, T.K. Gaylord, "Formulation for stable and efficient implementation of the rigorous coupled–wave analysis of binary gratings", J. Opt. Soc. Am. A **12** 1068–1076 (1995).

[71] M. G. Moharam, D. A. Pommet, E. B. Grann, T. K. Gaylord, "Stable implementation of the rigorous coupled–wave analysis for surface–relief gratings: enhanced transmittance matrix approach", J. Opt. Soc. Am. A **12** 1077–1086 (1995).

[72] I. J. Hodgkinson, Q. H. Wu, B. Knight, A. Lakhtakia, K. Robbie, "Vacuum deposition of chiral sculptured thin films with high optical activity", Appl. Opt. **39** 642–649 (2000).

[73] P. Kipfer, R. Klappert, H. P. Herzig, J. Grupp, R. Dändliker, "Improved red color with cholesteric liquid crystals in Bragg reflection mode", Opt. Eng. **41** 638–646 (2002).

[74] F. Wang, M. W. Horn, A. Lakhtakia, "Rigorous electromagnetic modeling of near–field phase–shifting contact lithography", Microelectron. Eng. **71** 34–53 (2004).

[75] J. B. Geddes III, A. Lakhtakia, "Time–domain simulation of the circular Bragg phenomenon exhibited by axially excited chiral sculptured thin films", Eur. Phys. J. AP **14** 97–105 (2001); corrections: **16** 247 (2001).

[76] C. Oldano, "Comment on "Twist defect in chiral photonic structures"", Phys. Rev. Lett. **91** 259401 (2003).

[77] S. F. Nagle, A. Lakhtakia, "Attenuation and handedness of axial propagation modes in a cholesteric liquid crystal", Microw. Opt. Tech. Lett. **7** 749–75 (1994).

[78] V. A. Yakubovich, V. M. Starzhinskii, *Linear Differential Equations with Periodic Coefficients.* (Wiley, Chichester, UK, 1975).

[79] H. A. Haus, C. V. Shank, "Antisymmetric taper of distributed feedback lasers", IEEE J. Quantum Electron. **12** 532–539 (1974).

[80] E. I. Kats, "Optical properties of cholesteric liquid crystals", Sov. Phys. JETP **32** 1004–1007 (1971).

[81] A. Lakhtakia, W. S. Weiglhofer, "On light propagation in helicoidal bianisotropic mediums", Proc. R. Soc. Lond. A **448** 419–437 (1995); corrections: **454** 3275 (1998).

[82] P. C. Clemmow, *The Plane Wave Spectrum Representation of Electromagnetic Fields* (Pergamon, New York, NY, 1956).

[83] S. Peng, G. M. Morris, "Resonant scattering from two–dimensional gratings", J. Opt. Soc. Am. A **13** 993–1005 (1996).

[84] F. I. Baida, D. Van Labeke, J. M. Vigoureux, "Numerical study of the displacement of a three–dimensional Gaussian beam transmitted at total internal reflection. Near–field applications", J. Opt. Soc. Am. A **17** 858–866 (2000).

[85] J. Lekner, "Polarization of tightly focused laser beams", J. Opt. A: Pure Appl. Opt. **5** 6–14 (2003).

[86] A. Lakhtakia, M. W. McCall, "Response of chiral sculptured thin films to dipolar sources", Int. J. Electron. Commun. (AEÜ) **57** 23–31 (2003).

[87] W. J. Wild, C. L. Giles, "Goos–Hänchen shifts from absorbing media", Phys. Rev. A **25** 2099–2101 (1982).

[88] A. Lakhtakia, "On planewave remittances and Goos–Hänchen shifts of planar slabs with negative real permittivity and permeability", Electromagnetics **23** 71 (2003).

[89] A. Lakhtakia, J. B. Geddes III, "Nanotechnology for optics is a phase–length–time sandwich", Opt. Eng. **43** 2410–2417 (2004).

[90] A. M. Stoneham, "The challenges of nanostructures for theory", Mater. Sci. Eng. C **23** 235–241 (2003).

[91] U. Kreibig, M. Vollmer, *Optical Properties of Metal Clusters* (Springer–Verlag, Berlin, 1994).

[92] M. I. Stockman, D. J. Bergman, T. Kobayashi, "Coherent control of nanoscale localization of ultrafast optical excitation in nanosystems", Phys. Rev. B **69** 054202 (2004).

[93] C.–T. Tai, *Dyadic Green Functions in Electromagnetic Theory* 2nd ed. (IEEE Press, New York, 1994).

[94] A. Lakhtakia, *Beltrami Fields in Chiral Media* (World Scientific, Singapore, 1994).

[95] W. C. Chew, *Wave and Fields in Inhomogeneous Media* (IEEE Press, New York, 1995).

[96] A. K. Jordan, R. H. Lang, "Electromagnetic scattering patterns from sinusoidal surfaces", Radio Sci. **14** 1077-1088 (1979).

[97] M. Born and E. Wolf, *Principles of Optics* 6th ed. (Pergamon, Oxford, UK, 1987).

[98] F. Capolino, S. Maci, L. B. Felsen, "Asymptotic high–frequency Green's function for a planar phased sectoral array of dipoles", Radio Sci. **35** 579–593 (2000).

[99] F. Wang, "Note on the asymptotic approximation of a double integral with an angular spectrum representation", Int. J. Electron. Commun. (AEÜ) (accepted, 2004).

[100] D. Bouche, F. Molinet, R. Mittra, *Asymptotic Methods in Electromagnetics* (Springer, Heidelberg, Germany, 1994).

[101] A. Lakhtakia, M. F. Iskander, C. H. Durney, H. Massoudi, "Irradiation of prolate spheroidal models of humans and animals in the near field of a small loop antenna", Radio Sci. **17** 77S–84S (1982).

[102] H. Ichikawa, K. Fukuoka, "Femtosecond pulse shaping by a reflection grating in the resonance domain", Opt. Commun. **223** 247–254 (2003).

VITA

Fei Wang
CATMS — Computational & Theoretical Materials Sciences Group
Department of Engineering Science & Mechanics, The Pennsylvania State University

EDUCATION

M. S., Engineering Mechanics, July 2001, University of Science and Technology of China
B. S., Engineering Mechanics, July 1998, China University of Mining and Technology

HONORS

2005 Alumni Association Dissertation Award
2003–2004, 2001–2002 Weiss Graduate Fellowship
2002 SPIE Education Scholarship
1998 National Excellent Mechanics Student Award
1996 First Prize, The 3rd National College Students Applied Mechanics Contest

SELECTED JOURNAL PUBLICATIONS

- F. Wang, K. E. Weaver, A. Lakhtakia, M. W. Horn, *Optik* (In press, 2005).
- F. Wang, *Int. J. Electron. Commun. (AEÜ)* (In press, 2005).
- F. Wang, K. E. Weaver, A. Lakhtakia, M. W. Horn, *Microelectron. Eng.* **77** 55–57 (2005).
- F. Wang, A. Lakhtakia, *Opt. Commun.* **235** 133–151 (2004).
- F. Wang, A. Lakhtakia, *Opt. Commun.* **235** 107–132 (2004).
- F. Wang, M. W. Horn, A. Lakhtakia, *Microelectron. Eng.* **71** 34–53 (2004).
- F. Wang, A. Lakhtakia, *Opt. Commun.* **215** 79–92 (2003).
- F. Wang, A. Lakhtakia, R. Messier, *J. Mod. Opt.* **50** 239–249 (2003)
- F. Wang, A. Lakhtakia, R. Messier, *Eur. Phys. J. Appl. Phys.* **20** 91–103 (2002).
- F. Wang, A. Lakhtakia, R. Messier, *Sens. Actuat. A* **102** 31–35 (2002).